UNIVERSITY OF CALIFORNIA,
IRVINE

Characteristics of the Velocity Power Spectrum as a Function of Taylor Reynolds Number

DISSERTATION

submitted in partial satisfaction of the requirements
for the degree of

DOCTOR OF PHILOSOPHY

in Mechanical and Aerospace Engineering

by

Alejandro J. Puga

Dissertation Committee:
Professor John C. LaRue, Chair
Professor Derek Dunn-Rankin
Professor Said Elghobashi

2016

Dedication

To my mom and dad for their love and support and for teaching me the value of hard work. To my sister and brother who inspire me everyday and who keep me grounded when I get out of hand. To my friends who **p**rovided the much needed distraction that **k**ept me sane. And, finally, to my wife who makes difficult endeavors worth pursuing.

Table of Contents

List of Figures

List of Tables

Acknowledgments

I would like to thank my advisor, Prof. John C. LaRue, for his insight, advice and patience without which I could not have completed this milestone. I would also like to thank my graduate colleagues, Timothy Koster, Baolong Nguyen, James Lewis, Rosa Padilla and Abdullah Alkudsi who provided thoughtful discussion and assistance in debugging programs and equipment. I would like to thank Allen Kine for his help regarding key electronic equipment needed for signal conditioning. I would also like to thank Oleg Goushcha for his help in the development of the active grid and Laurent Mydlarski and Zellman Warhaft for their helpful suggestions early on in the project.

Curriculum Vitae

Alejandro J. Puga

EDUCATION

Doctor of Philosophy in Mechanical and Aerospace Engineering **2016**
University of California, Irvine *Irvine, CA*

Master of Science in Aeronautical and Astronautical Engineering **2008**
Purdue University *West Lafayette, IN*

Bachelor of Science in Aerospace Engineering **2006**
University of California, Irvine *Irvine, CA*

Abstract

Characteristics of the Velocity Power Spectrum as a Function of Taylor Reynolds Number

by

Alejandro J. Puga

Doctor of Philosophy in Mechanical and Aerospace Engineering

University of California, Irvine, 2016

Professor John C. LaRue, Chair

An understanding of the wide range of scales present in a turbulent flow as well as the turbulence kinetic energy associated with those scales can provide significant insight into the modeling of such flows. Since turbulence is a stochastic process, statistical quantities such as mean, root mean square, correlations and spectra are used to identify and understand the evolution of turbulent flows. Time-resolved velocity measurements presented herein are obtained using hot-wire anemometry in a nearly homogeneous, isotropic and moderately high Taylor Reynolds number, R_λ, flow downstream of an active grid. Velocity power spectra presented herein show that the slope, n, of the inertial subrange, where the inertial subrange is defined as the wavenumber range where the power spectrum scales as κ^{-n}, varies with R_λ as $n = 1.69 - 5.86R_\lambda^{-0.645}$. This variation in the slope of the inertial subrange is consistent with measurements presented by Mydlarski & Warhaft (1996) in an active grid flow and Saddoughi & Veeravalli (1994) in a turbulent boundary layer. The effectiveness of velocity power spectrum normalizations proposed by Kolmogorov (1941), vonKarman & Howarth (1938) and George (1992) are compared qualitatively and quantitatively. The effectiveness of these normalizations suggests how the turbulent scales make specific portions of the velocity spectrum self-similar. It is found that the relation between the large and small scales is also shown by the normalized dissipation rate, which is defined as the dissipation rate normalized

by the ratio of the turbulence kinetic energy to the time scale of the large scale structure, is shown to be a constant with respect to R_λ for $R_\lambda \geq 450$. A modified model for the one-dimensional velocity power spectrum is proposed that is based on a model proposed by Pope (2000), which has been demonstrated to model power spectra at high value of R_λ where the slope of the inertial subrange is very close to $-5/3$. This modification takes into account the variation in the inertial subrange slope found in the data presented herein.

Chapter 1

Introduction to the thesis

Power spectra and velocity statistics are obtained for downstream positions that range from $x/M = 35$ to 142 at mean velocities, $\overline{U}$, of 4, 8 and 12 m/s where x is the coordinate position in the downstream direction with origin at the active grid and M is the spacing between grid rods. Turbulence intensities, $\overline{u^2}^{1/2}/\overline{U}$, vary from 6 to 20% and Taylor Reynolds numbers, R_λ, vary from 191 to 997 where $R_\lambda \equiv \overline{u^2}^{1/2}\lambda/\nu$, λ is the Taylor Microscale and ν is the kinematic viscosity. The thesis consists of this introductory chapter and three additional chapters each of which correspond to an individual paper with a specific focus.

The primary focus of Chapter 2 is to determine the evolution of the non-dimensional dissipation rate, $D = l\epsilon/\mathbf{u}^3$ as a function of R_λ where l is the integral length scale, ϵ is the dissipation rate and $\mathbf{u}$ is the velocity scale where $\mathbf{u} \equiv (\frac{1}{3}q)^{1/2}$ and $q = \overline{u^2} + \overline{v^2} + \overline{w^2}$ is the turbulence kinetic energy. Two methods are employed to determine the integral scale. One is based on integrating the velocity correlation, l_a, and the second, l_s, is determined from the peak of the energy spectrum, $\kappa E_{11}(\kappa)$, where κ is the wavenumber and $E_{11}(\kappa)$ is the one-dimensional power spectrum of the downstream velocity (cf. Webb (1955)). At corresponding downstream positions, l_a and l_s are found to be nearly equal with l_s exhibiting

more scatter. The normalized dissipation rate is found to approach a constant value, D_∞, of 0.76 for $R_{\lambda,u_q} \geq 365$, where $R_{\lambda,u_q} \equiv (\frac{1}{3}q)^{1/2}\lambda/\nu$. This value of D_∞ is in general agreement with values presented by Sreenivasan (1984, 1998) in other experimental flows and various DNS studies.

Tennekes & Lumley (1972) note that $R_l = (D/15)R_\lambda^2$, which implies that D can be obtained from the determination of the slope of R_l when plotted as a function of R_λ^2. This approach leads to reduction in the scatter of the data set, but care must be taken to determine the slope and D_∞ in the range of R_λ where D is a constant. More specifically, at values of $R_{\lambda,u_q} \leq 365$, the slope of R_l versus R_{λ,u_q}^2 appears to vary only slightly which makes it difficult to determine the value of R_{λ,u_q}^2 for which D is a constant, and inclusion of data where D is not constant may result in an incorrect value for D_∞. It is found that for $R_{\lambda,u_q} \geq 365$ where D has reached a constant value with respect to R_{λ,u_q}, D_∞ is found to equal 0.76 using the slope determined from R_l versus R_{λ,u_q}^2.

The primary foci of Chapter 3 are to determine the slope of the inertial subrange as a function of R_λ and to assess the effectiveness of three spectral normalizations in collapsing the spectra. The normalizations proposed by vonKarman & Howarth (1938), Kolmogorov (1941) and George (1992) are considered and qualitative and quantitative comparisons are presented. In this chapter, the term "inertial subrange" is generalized to refer to the portion of the spectrum where $E_{11}(\kappa)\ \kappa^{-n}$ but where n does not necessarily equal $-5/3$. In the present study, n is found to vary from 1.40 to 1.63 for a corresponding variation of R_λ from 185 to 997. The values of n at corresponding R_λ values are in agreement with results in a turbulent boundary layer flow (Saddoughi & Veeravalli, 1994) and the results presented by Mydlarski & Warhaft (1996) in the flow downstream of an active grid with a range of R_λ from 183 to 473. Data obtained in a mixing layer and an atmospheric surface layer (Praskovsky & Oncley, 1994) with a corresponding variation of R_λ from 2.0×10^3 to 12.7×10^3 are also considered and a least squares fit of the values of n as a function of R_λ suggests that

$n = 1.69 - 5.86R_\lambda^{-0.645}$. The uncertainty in the asymptotic value of n is ± 0.036. The value of $-5/3$ falls within this uncertainty range, which means these results cannot be used to determine an accurate value for the intermittency factor, μ, which corrects Kolmogorov's original prediction of the slope of the inertial subrange from $-5/3$ to $-5/3 - \mu/9$.

The focus of Chapter 4 is the development of a spectral model that can model the inertial subrange and high wavenumber dissipation range of $E(\kappa)$ for the range of R_λ where n varies as a function of R_λ. The model is a modification of the one presented by Pope (2000) to take into account the changing slope of the inertial subrange. Pope's original model for the three dimensional spectrum follows

$$E_p(\kappa) = C\epsilon^{2/3}\kappa^{-5/3} f_l(\kappa l) f_\eta(\kappa\eta) \tag{1.1}$$

where $f_l(\kappa l) = \left(\frac{\kappa l}{[(\kappa l)^2 + c_l]^{1/2}}\right)^{5/3+p_o}$ and $f_\eta(\kappa\eta) = exp\left\{-\beta\left\{\left[(\kappa\eta)^4 + c_\eta^4\right]^{1/4} - c_\eta\right\}\right\}$ are are non-dimensional functions that determine the shape of the energy-containing and dissipation range, respectively. C, c_l, c_η and β are constants that need to be determined based on experimental data. The resulting modified model follows

$$E(\kappa) = C_\phi \epsilon^\phi \kappa^{-2\phi} (\epsilon^{2/3}\kappa^{-5/3}) f_l(\kappa l) f_\eta(\kappa\eta) \tag{1.2}$$

where $C_\phi = C\left(l_a/\overline{u^2}^{1/2}\right)^{3\phi}$ and $\phi = \frac{1}{2}\left(C_1 R_\lambda^{-C_2} - \mu/9\right)$. At the limit where R_λ approaches infinity, and assuming that $\mu = 0$, the modified spectrum model equals Pope's original model. The modified spectrum model is fitted to spectra obtained in the present study and it is found that the values for C and c_η approach those suggested by Pope as R_λ increases. Furthermore, the values for β are constant with respect to R_λ and are in general agreement with Pope. The values for c_l, however do not match those presented by Pope, which is consistent with observation that the low wavenumber, energy-containing range is dependent on the manner

in which the turbulence is being generated. This leads to the possibility that no one model would be able to accurately model the spectrum values in the energy-containing range.

Chapter 2

Normalized dissipation rate in a moderate Taylor Reynolds number flow

2.1 Abstract

Time-resolved velocity measurements obtained using a hot-wire in a nearly homogeneous and isotropic flow for a range of Taylor Reynolds numbers from 191 to 660 reveal that the ratio of dissipation to the time scale of the large scale structure, $D_\infty = l\epsilon/\mathbf{u}^3$ where ϵ is the dissipation and $\mathbf{u} \equiv (q/3)^{1/2}$, is a constant equal to 0.73 for $R_{\lambda,u_q} > 365$, where $R_{\lambda,u_q} \equiv (q/3)^{1/2}\lambda/\nu$, which is in general agreement with Sreenivasan (1984, 1998). Integral length scale (l_a) measurements obtained from the velocity correlation are in close agreement with integral length scale (l_s) measurements obtained from the peak of the energy spectrum, $\kappa E_{11}(\kappa)$, where κ is the wavenumber and $E_{11}(\kappa)$ is the one-dimensional power spectrum of the downstream velocity. Tennekes & Lumley (1972) present $R_l = (D_\infty/15)R_\lambda^2$, which can

be used to find D_∞; however, the current study suggests that care should be taken when using this method as it may incur an error if points used coincide with ranges where D is R_λ dependent.

2.2 Background

One of the most fundamental concepts in turbulent flows is that the dissipation, ϵ, of turbulent kinetic energy, represented by $\mathbf{u}^2$, of the large eddies of scale l must be proportional to the time scale of those eddies, $l/\mathbf{u}$, where $\mathbf{u}$ is the velocity scale corresponding to the large scale structures. Based on that reasoning, an estimate for the dissipation is that

$$\epsilon = D\mathbf{u}^3/l \tag{2.1}$$

where D is a proportionality constant expected to be of order unity. While it is possible to find the constant D by determining values of ϵ, $\mathbf{u}$ and l, Tennekes & Lumley (1972) present an alternative expression where D can be determined as

$$R_l = (D/15)R_\lambda^2 \tag{2.2}$$

where R_l is the Reynolds number based on the length scale, l, and is defined as

$$R_l = \frac{\mathbf{u}l}{\nu} \tag{2.3}$$

where ν is the kinematic viscosity. R_λ is the Reynolds number based on the Taylor microscale,

$\lambda \equiv \overline{u^2}/\overline{(\frac{\partial u}{\partial x})^2}$ where the overbar denotes time average, and is defined as

$$R_\lambda = \frac{\mathbf{u}\lambda}{\nu}. \tag{2.4}$$

The proportionality constant, D, has been determined experimentally for a variety of flows as well as in DNS studies. Sreenivasan (1984, 1998) presents an estimate of D measured using equation 2.1 for both wind tunnel experiments and a compilation of DNS studies conducted by several groups. For the DNS studies presented with R_λ values ranging from about 25 to 250, Sreenivasan (1998) suggests that for $R_\lambda < 150$, D decreases as R_λ increases and, for $R_\lambda > 150$, D reaches a constant value, defined as D_∞. The multiple DNS studies presented by Sreenivasan (1998) align themselves into two groups, one with $D_\infty = 0.4$ and the other with $D_\infty = 0.7$. The larger D_∞ value is consistent with Sreenivasan's reported value of $D_\infty = 0.73$ in decaying turbulence produced by a stationary square grid with round rods. Kaneda *et al.* (2003) conduct DNS experiments on homogeneous turbulence in a periodic box and are able to determine D for $94 \leq R_\lambda \leq 1200$ using equation 2.1. These results show that for $R_\lambda < 300$, D decreases with increasing R_λ and, for$R_\lambda > 300$, a value of D_∞ between 0.4 and 0.5 is observed. This value is consistent with the results of Boffetta & Romano (2002) who report a value of D_∞ of about 0.4 in a jet flow. Mydlarski & Warhaft (1996), hereafter referred to as MW96, conduct an experiment using an active grid with a mesh spacing of $5cm$ and a wind tunnel test section size of 40.65×40.65 cm and find that $D_\infty = 0.9$ for $50 \leq R_\lambda \leq 473$ using an approach based on equation 2.2. Thus, there are several approaches that can be used to determine D_∞ and, in the various studies cited, several different values for D_∞ are determined.

The first step in the determination of D is to determine the values for the characteristic velocity and length scale as well as the dissipation rate. If the flow is isotropic, then an

appropriate velocity scale is

$$\mathbf{u} \equiv \overline{u^2}^{1/2} \tag{2.5}$$

or alternatively,

$$\mathbf{u} \equiv (q/3)^{1/2} \tag{2.6}$$

where $q = \overline{u^2} + \overline{v^2} + \overline{w^2}$ and u, v and w are the velocity components in the three coordinate directions. If the flow is isotropic, the two scales are the same but if there is a departure from isotropy, the two scales would have different values which would lead to different values for the normalized dissipation.

The length scale of the large structures, hereafter referred to as the integral length scale, can be determined using several different approaches. If the spatial correlation of the downstream velocity in the downstream direction, i.e.

$$\rho(u(x,t)u(x+\delta x,t)) = \frac{\overline{u(x,t)u(x+\delta x,t)}}{u(x,t)^2} \tag{2.7}$$

has an exponential decay with δx, then the integral length scale has been shown to correspond to the wavenumber of the peak of the energy spectrum, $\kappa E_{11}(\kappa)$, where κ is the wavenumber and $E_{11}(\kappa)$ is the one-dimensional power spectrum of the downstream velocity (cf. Webb (1955)). In this approach,

$$l \equiv l_s = 1/\kappa_n \tag{2.8}$$

where l_s is the integral length scale measured using the spectrum method and κ_n is the location in wavenumber of the peak of the energy spectrum.

An alternative approach to determine l is one based on the integration of the time autocorre-

lation of the downstream velocity. For this approach, the integral length scale is determined from the integral time scale, which is defined as

$$T = \int_0^{\tau=\infty} \rho(u(x,t)u(x,t+\tau))d\tau \tag{2.9}$$

where

$$\rho(u(x,t)u(x,t+\tau)) = \frac{\overline{u(x,t)u(x,t+\tau)}}{u(x,t)^2} \tag{2.10}$$

and the integral length scale is defined as

$$l \equiv l_a = \overline{U}T \tag{2.11}$$

where l_a is the integral length scale measured using the autocorrelation method and $\overline{U}$ is the mean speed.

The dissipation is determined using the variance of the temporal velocity derivative, Taylor's hypothesis and the assumption of local isotropy and is defined as

$$\epsilon = 15\nu\overline{\left(\frac{\partial u}{\partial x}\right)^2} = \frac{15\nu}{\overline{U}^2}\overline{\left(\frac{\partial u}{\partial t}\right)^2}. \tag{2.12}$$

Due to the relatively high turbulence intensities (defined as $\overline{u^2}^{1/2}/\overline{U}$) of as high as 11% observed in the study presented herein, the validity of Taylor's hypothesis must be investigated to ensure proper space-time conversion or a correction must be employed if deemed necessary. These corrections are motivated by the fact that Taylor's hypothesis may not be accurate in non-homogeneous flows with large turbulence intensities. Champagne (1978) demonstrates that in an inhomogeneous flow with an intensity of 9%, Taylor's hypothesis can be used to

accurately determine the spatial derivative from the time derivative and, hence assuming the flow is locally isotropic, determine the dissipation using the relationship shown in equation 2.12.

The goals of the study presented herein are 1) to determine the value for D based on equations 2.1 and 2.2 as a function of R_λ; 2) to determine the value of R_λ where D becomes a constant, defined as D_∞; 3) to determine the effect on the value of D_∞ using the two velocity scales defined in equations 2.5 and 2.6; 4) to compare the values of R_λ where D becomes a constant and the value of D_∞ to those of previous studies. An additional goal of the present study is to provide a comparison of the measures of l_a and l_s as defined in equations 2.8 and 2.11.

2.3 Experimental setup

2.3.1 Flow facilities

The flow facility used for this experiment is the closed-return wind tunnel at the University of California, Irvine. The tunnel has a rectangular test section that is 0.91 m tall, 0.61 m wide, 6.71 m long and is preceded by a contraction section with an area reduction ratio of 9.36. The ceiling and floor of the test section diverge to compensate for boundary layer growth and, thereby minimizing the mean velocity variation in the downstream direction. The high intensity, nearly homogeneous and isotropic flow is produced by means of an active, turbulence-generating grid, which is based on the initial design of Makita & Sassa (1991) as implemented by MW96.

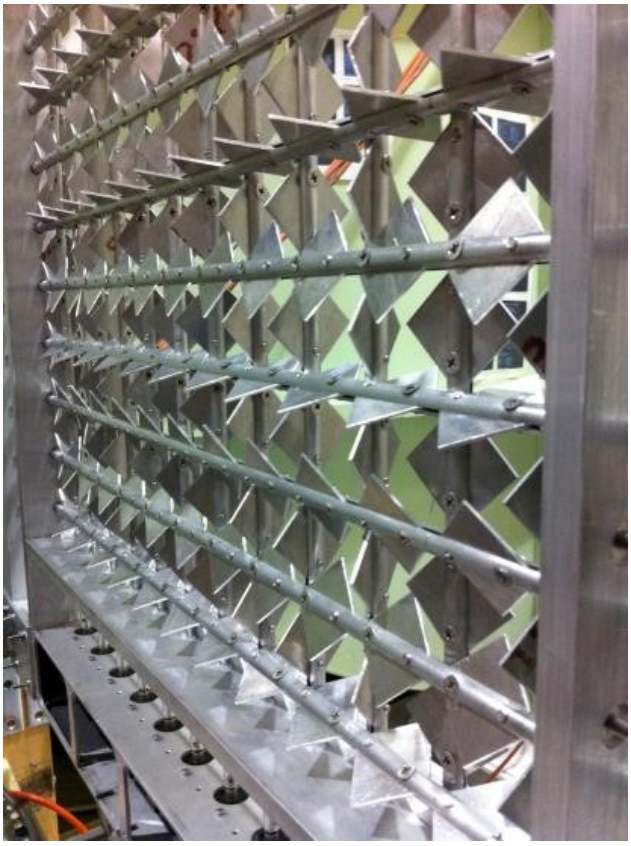

Figure 2.1: Image of turbulence-generating active grid.

2.3.2 Active grid

The active grid consists of an aluminum frame that holds 18 horizontal and 12 vertical cylindrical rods to form a square mesh, which can be seen in figure 2.1. The rods measure 9.5 mm in diameter and are spaced 50.8 mm apart. Hereafter, the rod spacing is referred to as M. Diamond-shaped flaps measuring 33 mm on a side are center-mounted along a 1.6 mm slit down the center of each rod. The rod ends are placed in an oil-impregnated brass sleeve bearing that allows the rods to rotate smoothly and minimize their wear. Each rod is attached to a high torque Anaheim Automation 17MD102S stepper motor that has a resolution of 200 steps per revolution and is mounted inside the hollow outer frame.

Two independent Parallax ProtoBoards with a USB interface, each capable of controlling 15 motors, are used to control the rotation speed and direction of rotation. If the controller is

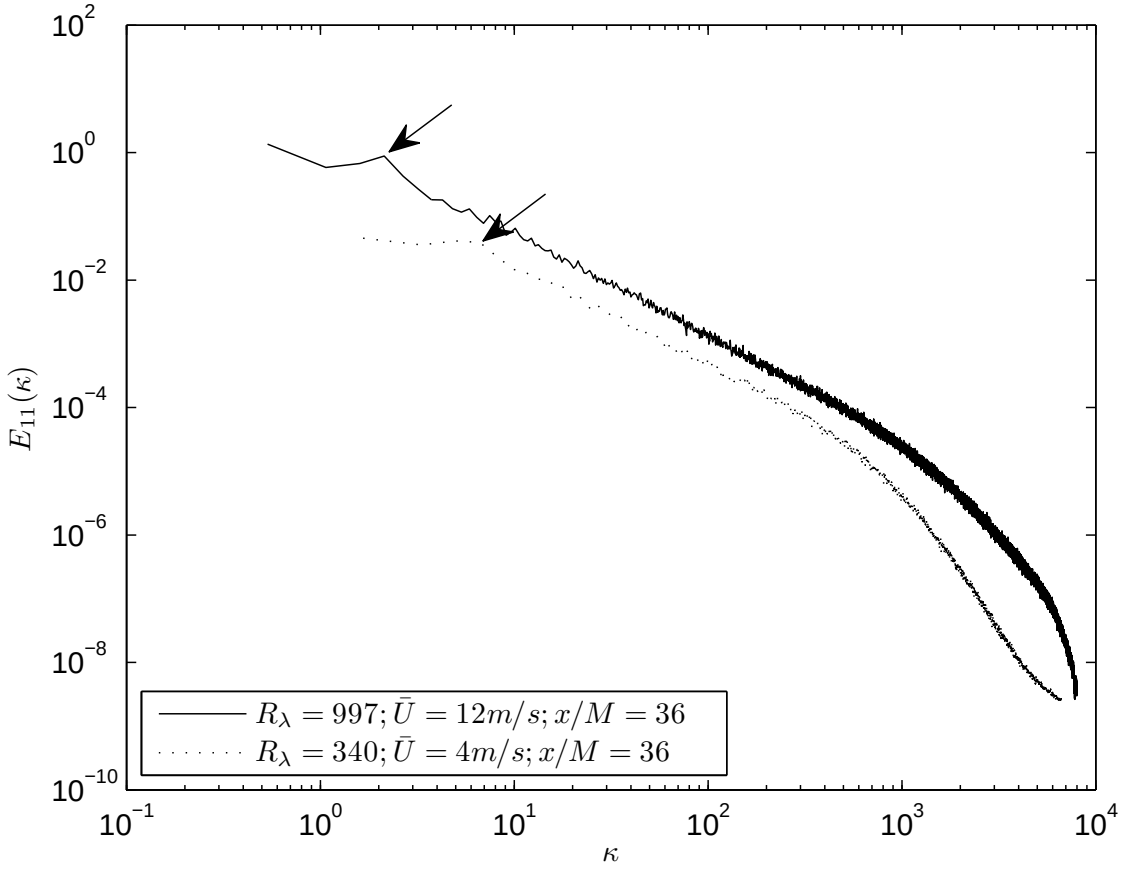

Figure 2.2: Velocity power spectra obtained at $x/M = 36$. Arrows denote the relative peaks corresponding to a frequency equal to twice the rotation rate of the active grid rods.

programmed to provide a fixed rotation rate and direction to the motors, the velocity power spectra will have a large relative peak that is centered at twice the rotation rate. Therefore, to minimize the effect of this peak, the mean rotation rate (MRS) is set to two revolutions per second and the motor rotation rates are programmed to vary $\pm 25\%$ relative to the MRS. The direction of rotation along with the rotation rates are programmed to change every 125 to 325 *msec*. It is important to note that all of the motors controlled by the same microcontroller will be assigned a new speed and direction at the same time.

Although grid parameters are randomized, the relative peak is not completely eliminated as can be seen in figure 2.2, which shows velocity power spectra with mean velocities of 4 and

12 m/s at $x/M = 36$. The relative peak becomes more pronounced as the mean velocity increases and at most has a magnitude of a fraction of a decade. Integration of the power spectra to determine the relative contribution of the peak to the measured velocity variance indicates a contribution of less than 1%. Due to the small size of the peak and relatively small contribution to the measured velocity variance, no corresponding correction is made to the measured values of $\overline{u^2}$. Also, in order to reduce noise, spectra are computed from the average of 120 data sets each 1 *sec* in length.

2.3.3 Sensors

The time-resolved velocity is measured using a standard, one-component hot-wire sensor. The hot-wire is fabricated from a 5.08 μm diameter Wollaston platinum wire manufactured by Sigmund Cohn. It is soldered to two stainless steel needles that are nickel plated to provide good electrical contact. The length of the platinum wire is nominally 1 mm, which yields a length to diameter ratio of about 200. This ratio matches the optimal ratio suggested by Azad (1993), which minimizes prong effects while maximizing spatial resolution. Wyngaard (1968) proposes a correction for the velocity spectrum taken from hot wires of finite length that, when implemented, shows the r.m.s. of velocity to be less than 1% in error with the sensor used in this experiment. For that reason, no correction due to spatial averaging is made. The hot-wire sensor is powered by an AA Labs System model AN-1005 constant temperature anemometer (CTA) with an overheat ratio of 1.75, which corresponds to a wire temperature of 249.9°C. A pulse response test indicates that the frequency response of the sensor is at least 30 kHz at 18 m/s. The wire temperature (T_w) is determined experimentally to within 1°C by varying the speed from 2 to 20 m/s and varying temperature from 20°C to 100°C in a laminar calibration jet. This procedure will be discussed in detail in the calibration procedure section. Sensors are calibrated for T_w only a few times during the course of an experiment, however, a velocity calibration is obtained at the start and end of

each data collection period. If the statistics of interest vary more than 1% when analyzed using the calibration coefficients found before and after the experiment, the corresponding data are discarded.

A reference mean velocity is obtained using a Pitot-static tube connected to an MKS Baratron Model 698A11TRE differential pressure transducer. The maximum difference between the mean velocity obtained using the Pitot-static tube and the hot-wire is less than 2%.

The mean temperature is measured using a platinum resistance thermometer (PRT) manufactured by Omega Engineering. It is connected to a custom-made Wheatstone bridge based on an Analog Devices 5B34-01 isolated linearized RTD Input Module. The PRT is mounted 5 cm away from the hot-wire and is used to correct the hot-wire signal for mean gas temperature variation.

2.3.4 Signal conditioning

The voltage output from the CTA is filtered using an analog, low pass, 4-pole Butterworth filter which incorporates a Frequency Devices (744PB-4) module. The filter has an insignificant amount of droop in the pass band up to 2/3 of the corner frequency, therefore, the corner frequency is set to 1.65 times higher than the frequency at which the signal reaches the noise level to ensure that the entire turbulent signal is not affected by the filter. Even though the filters are set to a higher than ideal corner frequency, the increased noise allowed to pass through increases the signal r.m.s. by less than 2% for the majority of the data collected. The signal then goes through a custom-built, 3-stage amplifier that can both amplify and offset the signal to ensure that the majority of the dynamic range of the analog to digital (A/D) converter is used. The frequency response of the amplifier is flat to approximately 70 kHz. Next, the signal goes through a voltage divider that can either pass the signal unattenuated or attenuate it by 2/3. The voltage divider is used in combination with the

amplifier to increase the signal to noise ratio. An analog, low noise differentiator is used to provide the time derivative of the hot-wire signal. The bandwidth of the differentiator is approximately 18 kHz.

All signals are digitized using a 16-bit Measurement Computing Corp. 1608-HS analog to digital converter with 8 differential analog inputs that have an operational input range of $\pm 10\ V$ and a maximum sampling rate of 250 kS/s per channel. The signal is transferred to a personal computer running $Windows\ 7$ via USB where the data are recorded and analyzed using $LabView2012$.

2.3.5 Calibration procedure

The calibration equation for the hot-wire is based on a modified form of Kings law:

$$E_{HW}^2 = \left(A_{HW} + B_{HW}\overline{U}^n\right)(T_w - T_g) \tag{2.13}$$

where E_{HW} is the voltage from the anemometer, $\overline{U}$ is the mean velocity, T_w is the wire temperature, T_g is the gas temperature and A_{HW} and B_{HW} are the calibration coefficients. As suggested by Bruun (1995), the value for the exponent, n, is determined using the calibration data and is not assumed to be 0.45. Based on the fact that $E_{HW}^2/(T_w - T_g)$ is linearly related to $\overline{U}^n$, appropriate values of T_w and n are found that minimize the nonlinearity. For the current study, T_w and n are $249.9°C$ and 0.403, respectively.

The next step in the calibration is carried out in the wind tunnel and is performed both before (pre-calibration) and after (post-calibration) a data collection period. For both the pre- and post-calibration, the gas temperature is measured using a PRT and the mean velocity is measured using the MKS Baratron and a Pitot-static tube. In this step, the velocity is varied

$Run\#$	$\overline{U},\ m/s$	x/M	$C_v = \frac{\overline{u^2}}{\overline{v^2}}$	$C_w = \frac{\overline{u^2}}{\overline{w^2}}$	R_λ
1	4	$45 - 142$	1.10 ± 0.019	1.12 ± 0.014	191-305
2	6	$55 - 142$	1.05 ± 0.014	1.16 ± 0.014	274-385
3	8	$65 - 142$	1.06 ± 0.018	1.18 ± 0.016	384-517
4	12	$80 - 142$	1.12 ± 0.016	1.25 ± 0.013	505-660

Table 2.1: Experimental parameters

over a range from 2 to 20 m/s and the wire temperature, T_w, and the velocity exponent, n, are assumed to remain equal to the values found in the previous step of the calibration. Data are only presented when the application of the pre- and post-calibration lead to less than a 1% variation in the statistical values of interest.

An R_λ range of 191 to 660 is achieved by varying mean speed, $\overline{U}$, and downstream location from the active grid, x/M. The mean velocities, range of downstream positions and corresponding Taylor Reynolds number ranges are shown in table 2.1. The starting downstream locations are chosen to correspond to the downstream position where $\overline{u^2}/\overline{v^2}$ and $\overline{u^2}/\overline{w^2}$ become nearly a constant (cf. Nguyen (2015)). The Taylor Reynolds number $\left(R_{\lambda_u} \equiv \overline{u^2}^{1/2}\lambda/\nu\right)$ range at each mean velocity and the values for $\overline{u^2}/\overline{v^2}$ and $\overline{u^2}/\overline{w^2}$ along with their standard deviations are also shown in table 2.1. It should be noted that the turbulent kinetic energy is computed using the following equation:

$$q = \overline{u^2} + \frac{1}{C_v}\overline{u^2} + \frac{1}{C_w}\overline{u^2} \tag{2.14}$$

where $C_v = \overline{u^2}/\overline{v^2}$ and $C_w = \overline{u^2}/\overline{w^2}$ and are the average values of the variance ratios over the downstream range of interest. Since the standard deviation of the values for C_v and C_w are small, the average values are used in determining the turbulent kinetic energy.

2.4 Analysis procedure

2.4.1 Integral length scale based on the autocorrelation

The integral length scale can be determined by integrating the spatial autocorrelation of the downstream velocity. However, in practice, a 1-point correlation in time is more easily obtained and transformed to a spatial correlation as shown in equations 2.9 – 2.11. Nobach & Tropea (2012) compare a 2-point longitudinal spatial correlation taken with an LDA system to a 1-point time correlation. They find that the temporal correlation can be accurately transformed into the spatial correlation for flows with turbulence intensities of up to 25% and, hence, l_a can be determined accurately using equation 2.11.

One challenge in determining a unique value for the integral length scale using this method is that the autocorrelation for a finite time sample varies in value at different time shifts, τ. For example, figures 2.3 and 2.4 show 23 autocorrelation curves taken at 8 m/s and $x/M = 35$ and at 4 m/s and $x/M = 60$, respectively. The error bars shown on the plot represent ± 2 standard deviations ($\rho_{r.m.s.}$) from the mean normalized autocorrelation value as a function of time. Formally, the integral time scale is computed by integrating an autocorrelation to an infinite time shift as shown in equation 2.9, however, in practice, the integral time scale is determined by integrating the autocorrelation to the time corresponding to the first zero crossing. The variation in the autocorrelations leads to a variation in the value of the time corresponding to the first zero crossing. For the autocorrelations shown in figure 2.3, that variation in the zero crossing time has little effect on the value of the integral time scale, which has an uncertainty of less than 3%. However, as shown in figure 2.4, the variability in the value of the autocorrelation can have a significant effect on the values of the time of the first zero crossing and also on the value of the integral time scale, in this case, the variation is 16%.

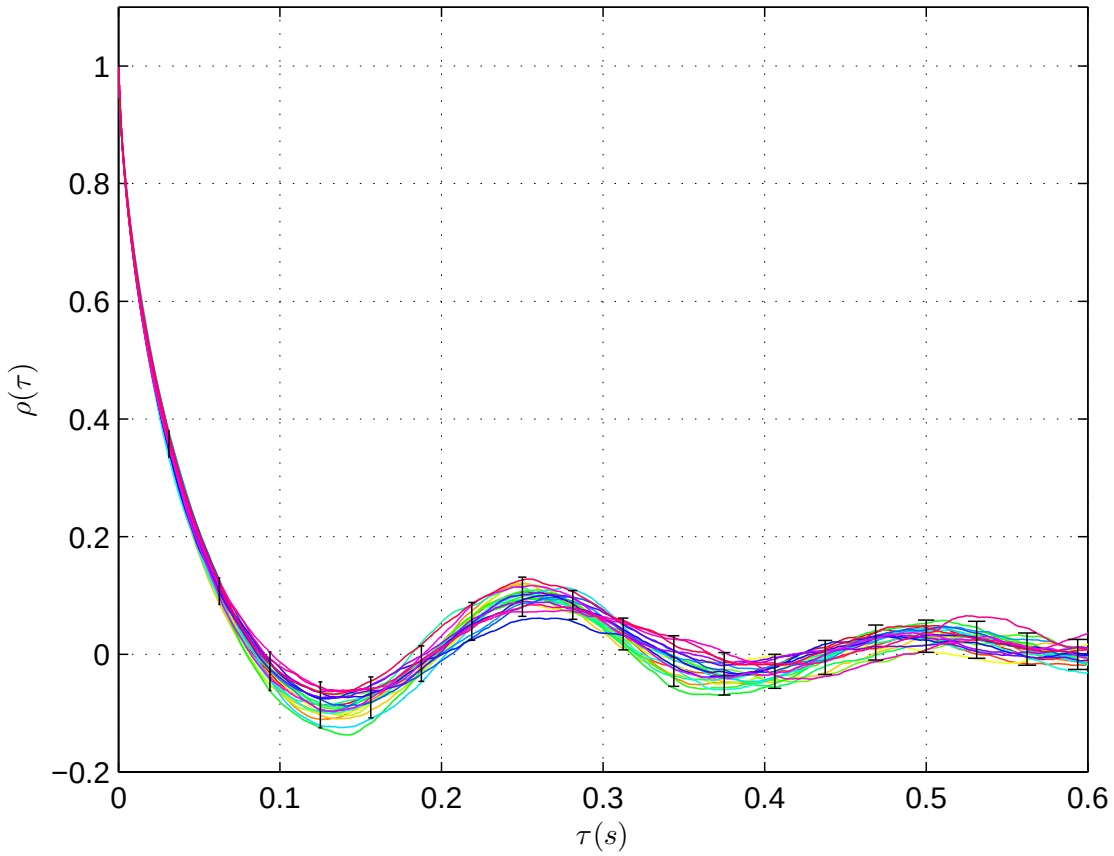

Figure 2.3: 23 autocorrelations taken at $\overline{U} = 8\ m/s$ and $x/M = 35$. The dot shows the local ensemble average of the autocorrelation and the error bars represent the scatter of the autocorrelation ($2\rho_{r.m.s.}$).

To minimize the effect of the variability in the values of the autocorrelation and the variability in the value of the first zero crossing time, a modified version of equation 2.9 is employed where

$$T_o = \int_0^{\tau_o} \rho(u(x,t)u(x,t+\tau))d\tau \tag{2.15}$$

where

$$\tau_o \equiv \tau(\rho(\tau) = 0 + \delta) \tag{2.16}$$

where δ is twice the average value of the r.m.s. of the fluctuation of the correlation.

For all mean speeds and downstream positions, $\delta = 0.03 \pm 0.0053$. When the modified

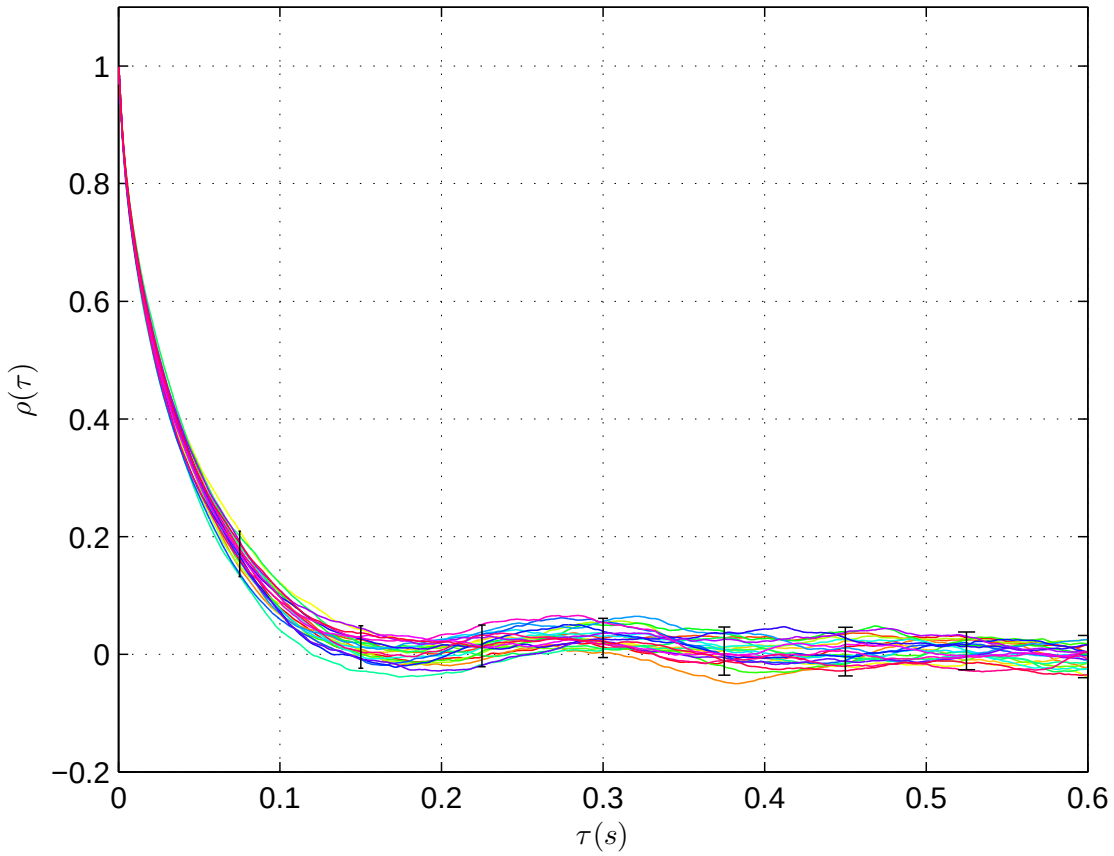

Figure 2.4: 23 autocorrelations taken at $\overline{U} = 4\ m/s$ and $x/M = 60$. The dot shows the local ensemble average of the autocorrelation and the error bars represent the scatter of the autocorrelation ($2\rho_{r.m.s.}$).

definition of the zero crossing time as shown in equation 2.16 is used, the uncertainty in the integral length scale from the autocorrelations shown in figure 2.4 decreases from 16% to 6%. For autocorrelations similar in structure to those shown in figure 2.3, the use of τ_o as defined in equation 2.16 leads to less than a 1% change in the integral time scale when compared to the value obtained using $\tau_o \equiv \tau(\rho(\tau) = 0)$.

As presented in section 2.3.2, the velocity power spectrum corresponding to higher mean speeds and close in proximity to the active grid have a relative peak at a frequency equal to twice the mean rotation rate. As noted by Tennekes & Lumley (1972), a spike of finite width in the spectrum generates decaying oscillations of wavelength $2\pi/\kappa$ in the correlation

and corresponds to the oscillations seen in the autocorrelation for longer time separations in figure 2.3.

2.4.2 Integral length scale based on the spectral method

The integral length scale has been shown (Webb, 1955) to correspond to the peak of the energy spectrum, $\kappa E_{11}(\kappa)$, for exponentially decaying autocorrelations. In this study, the autocorrelations do not have an exponential decay. Thus, there is some inherent uncertainty in the determination of the integral length scale using this approach. Furthermore, the relative peak in the power spectrum corresponding to the rod rotation of the active grid can obscure the location of the peak that corresponds to the large scale structure. For example, a sample energy spectrum measured at a mean speed of 8.01 m/s at $x/M = 142.5$ is shown in figure 2.5 where the peak occurs at a wavenumber of 6.2 m^{-1}, which corresponds to a frequency of 7.9 Hz. However, for some combinations of means speed and downstream locations, e.g. at 11.7 m/s and $x/M = 38$, as shown in figure 2.6, the peak in the energy spectrum occurs at a wavenumber of 2.1 m^{-1} with a corresponding frequency of 4 Hz, which is equal to twice the rotation rate of the grid. Thus, for this study, it is only possible to obtain the integral length scale using the peak of the energy spectrum at certain downstream locations.

2.5 Results

As mentioned in the background section, one of the steps to determine D is to identify the velocity scale, $\mathbf{u}$. The results presented herein use the two characteristic velocity scales identified in equations 2.5 and 2.6 and apply them to the definition of R_λ, R_l and D (equations 2.1, 2.3 and 2.4, respectively) in order to determine the effect on the value of D as a function

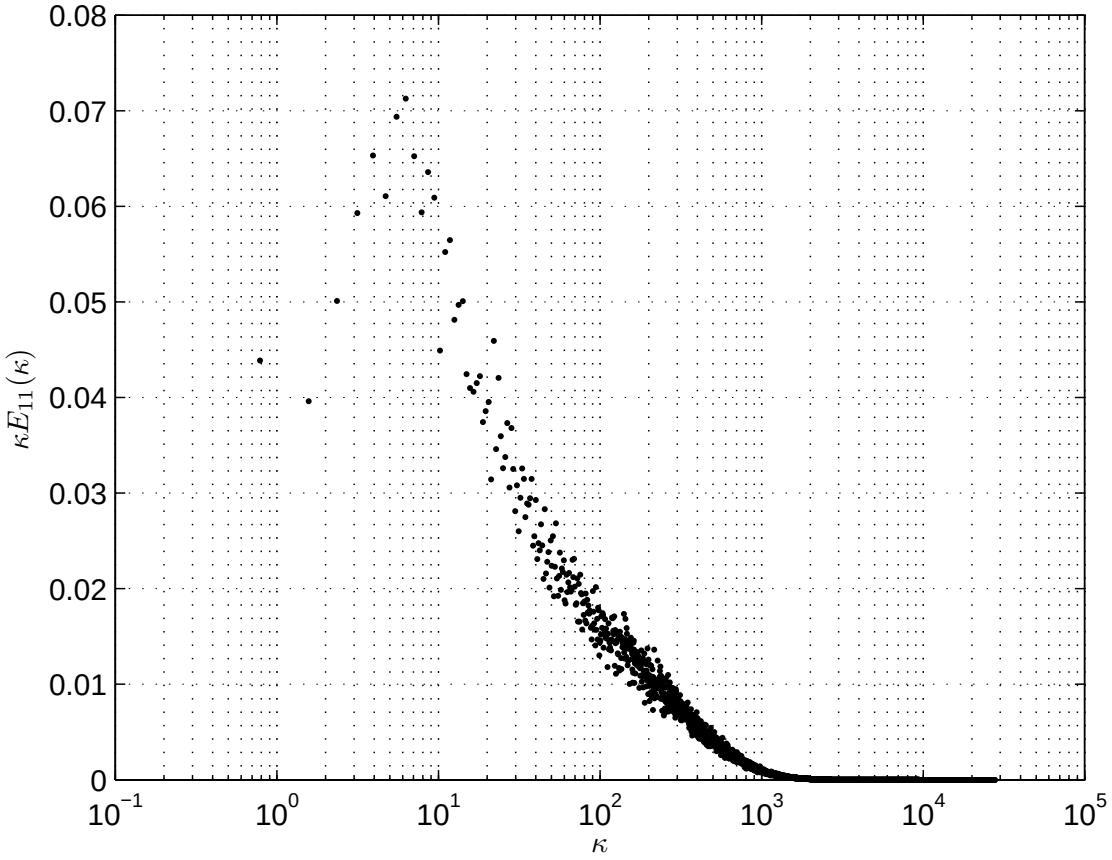

Figure 2.5: Energy spectrum ($\kappa E_{11}(\kappa)$) taken at 8.01 m/s at $x/M = 142.5$ exhibiting a clear spectral peak used to compute the integral scale, l_s.

of R_λ. If the flow is isotropic, then the two characteristic velocity scales would lead to the same results. However, since the flow is slightly anisotropic, the use of the two velocity scales will cause a shift in the values of R_λ, R_l and D, which can be seen in table 2.2. The magnitude of the shift depends on the anisotropy as shown in table 2.1. In table 2.2, the subscripts u_q and u_u represent the use of $(q/3)^{1/2}$ and $\overline{u^2}^{1/2}$ as the velocity scale, respectively.

Figure 2.7 shows D_{u_u} as a function of R_{λ,u_u}. The solid line on that figure corresponds to an exponentially decaying least squares fit to the data. D_{u_u} is seen to initially decrease with increasing R_{λ,u_u} and reaches a value of $D_{u_u,\infty} = 0.64$ at $R_{\lambda,u_u} \approx 450$. The value of R_{λ,u_u} where $D_{u_u,\infty}$ is reached is higher than those reported in the DNS studies from Sreenivasan

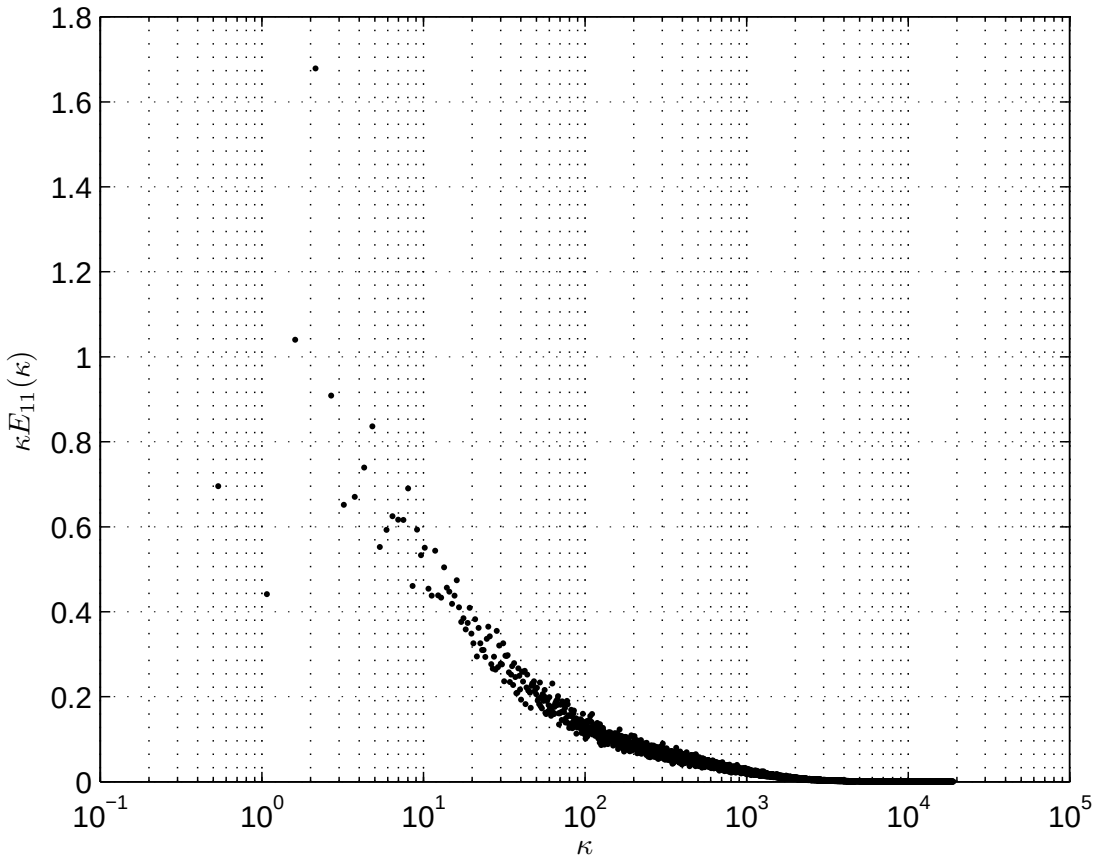

Figure 2.6: Energy spectrum ($\kappa E_{11}(\kappa)$) taken at 11.7 m/s and $x/M = 38$ and contains a relative peak at 4 Hz that obscures the spectral peak needed to find the integral scale, l_s.

$Run\#$	$C_D = \frac{D_{u_q}}{D_{u_u}}$	$C_{R_l} = \frac{R_{l,u_q}}{R_{l,u_u}}$	$C_{R_\lambda} = \frac{R_{\lambda,u_q}}{R_{\lambda,u_u}}$
1	1.11	0.966	0.934
2	1.10	0.969	0.938
3	1.11	0.965	0.965
4	1.18	0.947	0.947

Table 2.2: Ratios of D, R_l and R_λ when $u_q \left(= (q/3)^{1/2}\right)$ and $u_u \left(= \overline{u^2}^{1/2}\right)$ are used as the as the characteristic velocity scale.

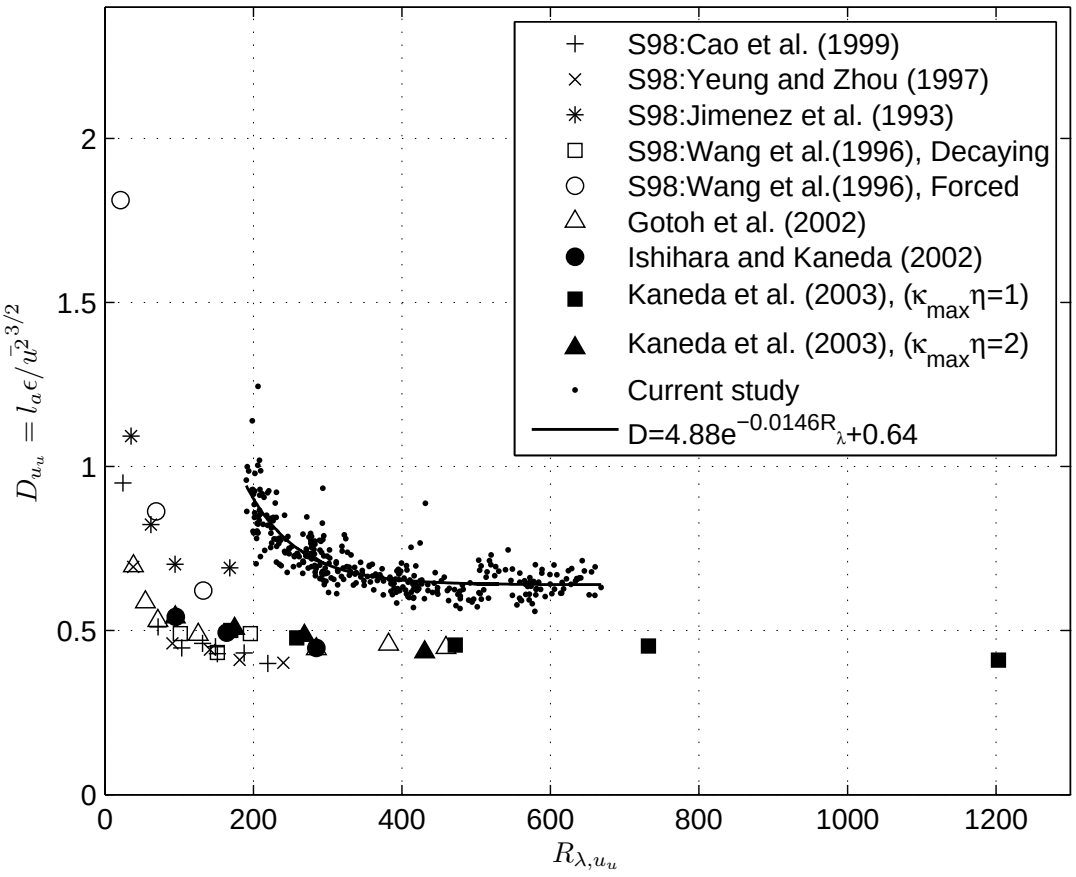

Figure 2.7: Comparison of D_{u_u} vs R_{λ,u_u} for the current study to several DNS studies. The DNS data used in S97 ((Sreenivasan, 1998)) include Cao *et al.* (1999), Yeung & Zhou (1997), Jiménez *et al.* (1993) and Wang *et al.* (1996).

(1998) and Kaneda *et al.* (2003) who show plateaus being reached at $R_{\lambda,u_u} = 100 \sim 300$ (note that since DNS can produce perfectly isotropic flows, $u_u = u_q$). Furthermore, the $D_{u_u,\infty}$ value found here is higher than the $D_{u_u,\infty}$ values of $0.4 \sim 0.5$ reported by Kaneda *et al.* (2003) and the lower $D_{u_u,\infty}$ value of about 0.4 reported by Sreenivasan (1998), which includes data from Cao *et al.* (1999), Wang *et al.* (1996) and Yeung & Zhou (1997).

One reason for the difference between the values of $D_{u_u,\infty}$ reported by Kaneda *et al.* (2003) and that of the present study may be due to the different expressions used to evaluate the integral length scale. More specifically, the integral length scale definition used by Kaneda

et al. (2003) is $l_B = (\pi/2\overline{u^2}) \int \kappa^{-1} E(\kappa) d\kappa$ where $E(\kappa)$ is the 3-dimensional velocity power spectrum. The relation between l_a and l_B remains to be determined.

Figure 2.8 shows the same data as shown in figure 2.7 but with u_q as the characteristic velocity scale. Starting at low values of R_{λ,u_q}, D_{u_q} decreases with increasing R_{λ,u_q} eventually reaching a nearly constant value of $D_{u_q,\infty} = 0.73$ at $R_{\lambda,u_q} \approx 365$. The value of R_{λ,u_q} where $D_{u_q,\infty}$ is reached is closer to those reported by Sreenivasan (1998) and Kaneda *et al.* (2003) and the value of $D_{u_q,\infty}$ reported here is in agreement with the larger $D_{u_q,\infty}$ value reported by Sreenivasan (1998), which includes DNS data from Jiménez *et al.* (1993) and Wang *et al.* (1996). The value of $D_{u_q,\infty}$ reported here is also in agreement with the value ($D_{u_q,\infty} = 0.73$) reported by Sreenivasan (1998) from the grid turbulence experiment.

In both figures 2.7 and 2.8, it can be noted that a few values for D_{u_u} and D_{u_q} are notably higher than the bulk of the data. The approach summarized by equation 2.15 is used to determine the integral length scale for these results. However, the value of the first minimum of their autocorrelation is greater than δ which increases the time to the first zero crossing causing an increase in the value of the integral length scale.

An alternative approach that has been used to determine D_∞ is based on the analysis presented by Tennekes & Lumley (1972) as summarized by equation 2.2. This approach is used by MW96 to find $D_{u_u,\infty}$ as it minimizes the scatter in the data. Figure 2.9 shows a plot of R_{l_a,u_u} as a function of R^2_{λ,u_u} where a linear least squares fit for $R_{\lambda,u_u} > 450$ leads to $D_{u_u,\infty} = 0.65$, which is consistent with the value of $D_{u_u,\infty}$ found from Figure 2.7.

In contrast, MW96 report $D_{u_u,\infty} = 0.9$ for their active grid flow. One possible reason for the difference between the $D_{u_u,\infty}$ value reported by MW96 and that obtained in the currents study is that the data used by MW96 include an R_{λ,u_u} range of 50 to 473. If an R_{λ,u_u} range is used where the value of D_{u_u} has not yet reached a constant, the resulting $D_{u_u,\infty}$ value could be higher than the true value of $D_{u_u,\infty}$. For example, limiting the R_{λ,u_u} range to $R_{\lambda,u_u} < 300$

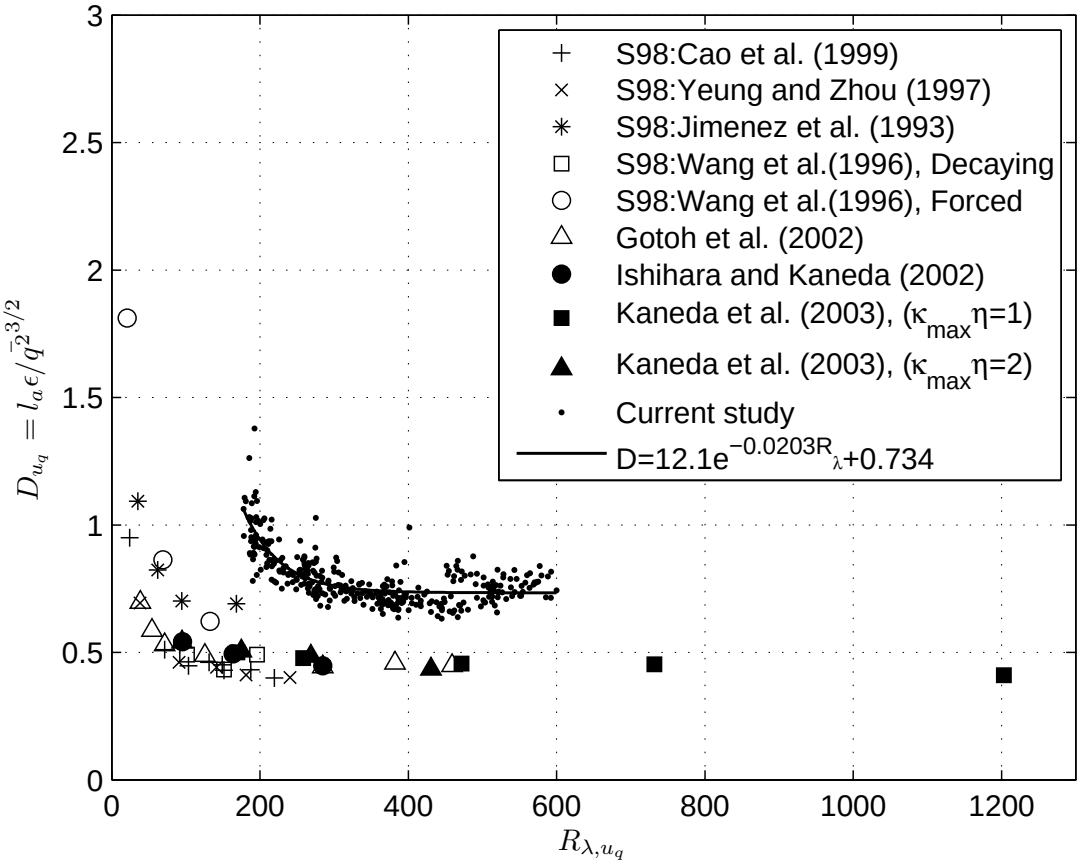

Figure 2.8: Comparison of D_{u_q} vs R_{λ,u_q} for the current study to several DNS studies. The DNS data used in S97 ((Sreenivasan, 1998)) include Cao *et al.* (1999), Yeung & Zhou (1997), Jiménez *et al.* (1993) and Wang *et al.* (1996).

leads to $D_{u_u,\infty} = 0.74$ even though the extrapolated linear least squares curve fit shown in figure 2.9 appears to follow the data for the entire range of R_{λ,u_u}.

Another possible reason for the difference in value for $D_{u_u,\infty}$ measured by MW96 and the one measured in the present study is that MW96 use l_s as the integral length scale while the present study uses l_a. A comparison of R_{l_a,u_u} *vs* R^2_{λ,u_u} and R_{l_s,u_u} *vs* R^2_{λ,u_u} is shown in figure 2.9 for MW96 and the present study. One of the main challenges in determining the integral scale, l_s, from the peak of the energy spectrum for the present study is that most of the spectra do not show a clearly defined peak due to the relative peak present at 4 Hz, as can be seen in figure 2.6. For most test conditions in the current study, the integral scale found

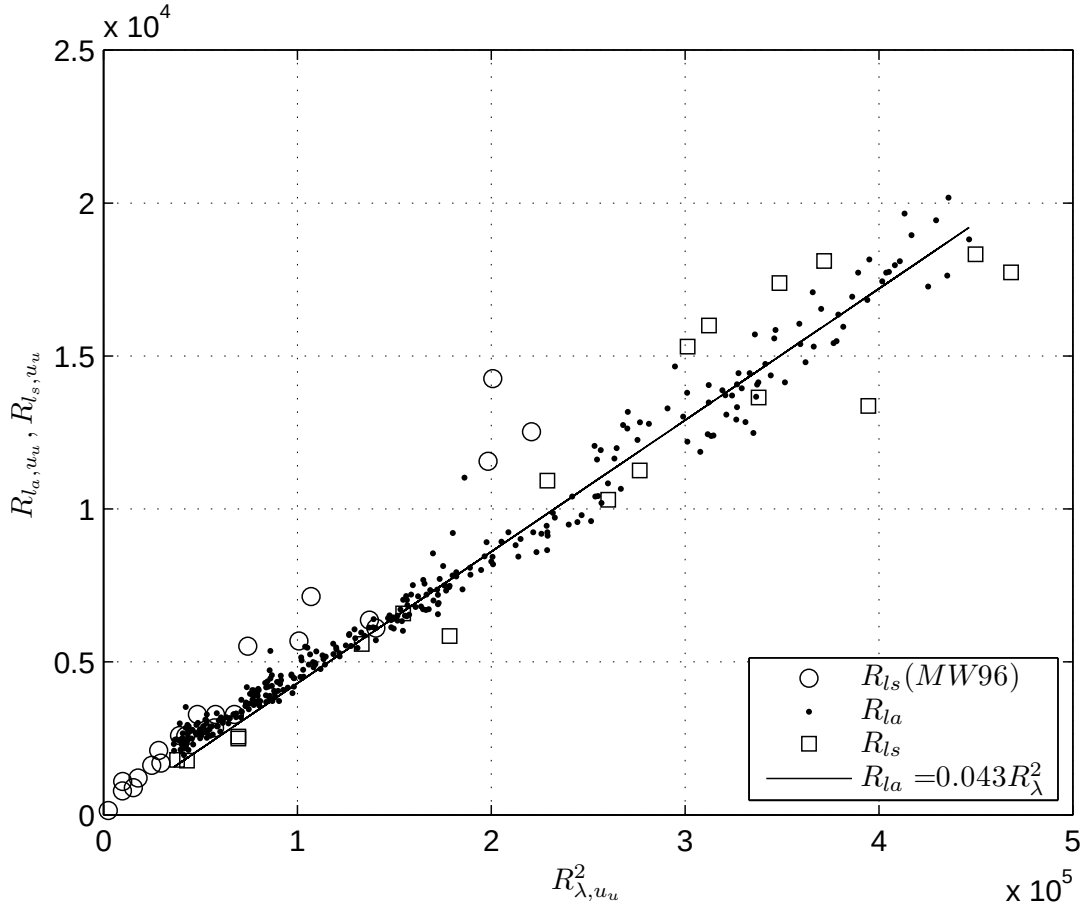

Figure 2.9: R_{l_a,u_u} vs R^2_{λ,u_u} and R_{l_s,u_u} vs R^2_{λ,u_u} for the current study and MW96. The line represents a linear least squares fit of R_{l_a,u_u} for data in the range $R_{\lambda,u_u} > 450$, which coincides with the range where D_{u_u} is nearly a constant, and is extrapolated to lower values of R^2_{λ,u_u}.

using the autocorrelations is not significantly affected by the relative peak at 4 Hz produced by the grid and, therefore, more data is available using this method. As a result, the integral length scale, l_a, determined from the autocorrelation is used. Although there is notably more scatter in the measure of R_{l_s,u_u}, it is clear that R_{l_a,u_u} and R_{l_s,u_u} are in good agreement for the current study. In fact, a linear least curve fit of the R_{l_s,u_u} data in figure 2.9 leads to $D_{u_u,\infty} = 0.64$, which is consistent with the$D_{u_u,\infty}$ value found from the autocorrelation data. Figure 2.9 also clearly shows that for $R^2_{\lambda,u_u} < 2.25 \times 10^5$, the data from MW96 is in generally good agreement with the current study, however for $R^2_{\lambda,u_u} > 2.25 \times 10^5$ the values of R_{l_s,u_u} from MW96 are generally higher than the R_{l_s,u_u} and R_{l_a,u_u} values obtained in the current

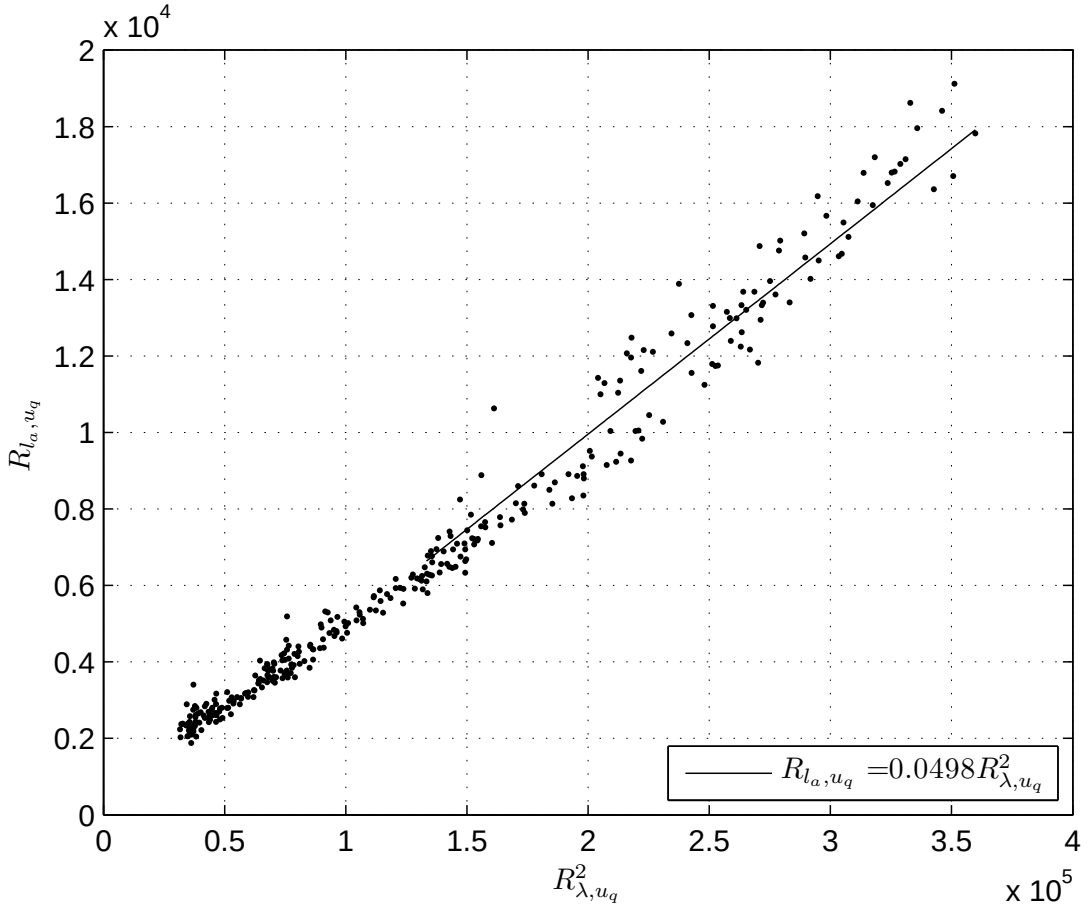

Figure 2.10: R_{l_a,u_q} vs R^2_{λ,u_q} for the current study and MW96. The line represents a linear least squares fit of R_{l_a,u_q} for data in the range $R_{\lambda,u_q} > 365$, which coincides with the range where D_{u_q} is nearly a constant, and is extrapolated to lower values of R^2_{λ,u_u}.

study. These higher R_{l_s,u_u} measurements lead to a steeper slope when a linear least curve fit is obtained, which leads to a higher $D_{u_u,\infty}$ value.

Figure 2.10 shows a plot of R_{l_a,u_q} as a function of R^2_{λ,u_q}. A linear least squares fit of R_{l_a,u_q} for data in the plateau region shown in figure 2.8 (i.e. $R_{\lambda,u_q} > 365$) leads to $D_{u_q,\infty} = 0.75$, which is also consistent with the results shown in figure 2.8.

2.6 Conclusion

Wind tunnel experiments are conducted in high intensity turbulence generated by means of an active turbulence grid modeled after the design proposed by Makita & Sassa (1991) as implemented by MW96. Time-resolved velocity measurements are obtained using a hot-wire anemometer for $191 \leq R_{\lambda,u_u} \leq 660$.

It is found that for $R_{\lambda,u_u} < 450$, the normalized dissipation rate $\left(D_{u_u} = l\epsilon/\overline{u^2}^{3/2} \right)$ decreases with increasing R_{λ,u_u} and, for $R_{\lambda,u_u} > 450$, values of D_{u_u} are found to reach a nearly constant value, defined as $D_{u_u,\infty}$, of 0.65. The flow studied herein is anisotropic, therefore the use of $u_q = (q/3)^{1/2}$ as the characteristic velocity scale is investigated. If the velocity scale is chosen to be $u_q = (q/3)^{1/2}$, $D_{u_q,\infty} = 0.73$, which is in closer agreement with the values of $D_{u_q,\infty} = 0.7$ from the DNS studies and $D_\infty = 0.73$ from the decaying turbulence experiment presented by Sreenivasan (1984, 1998).

It is suggested by Tennekes & Lumley (1972) and MW96 that $R_l = (D_\infty/15)R_\lambda^2$ can be used to find D_∞, however it is found here that great care should be taken as this method will incur an error if points used coincide with ranges where D is R_λ dependent. Close inspection of a plot showing R_l *vs* R_λ^2, such as the one shown in figure 2.10, may not be enough to select an appropriate R_λ range since the difference between the linear fit and the data points may be subtle.

Finally, integral length scale (l_a) measurements obtained from the velocity correlation are in close agreement with integral length scale (l_s) measurements obtained from the peak of the energy spectrum, $\kappa E_{11}(\kappa)$, where κ is the wavenumber and $E_{11}(\kappa)$ is the one-dimensional power spectrum of the downstream velocity as shown by Webb (1955).

Chapter 3

Variation in the velocity power spectrum as a function of Taylor Reynolds number

3.1 Abstract

The velocity power spectrum provides insight into how the turbulence kinetic energy is transferred from large to small scales. Velocity power spectra presented herein are obtained from time-resolved velocity measurements using hot-wire anemometry in a nearly homogeneous and isotropic flow for a range of Taylor Reynolds numbers, R_λ, from 194 to 997. It is shown that the slope, n, of the inertial subrange varies with R_λ as $n = 1.69 - 5.86 R_\lambda^{-0.645}$ and is consistent with experiments obtained in other grid and boundary layer flows. The effectiveness of velocity power spectrum normalizations proposed by Kolmogorov (1941), vonKarman & Howarth (1938) and George (1992) are compared qualitatively and quantitatively. The normalization proposed by Kolmogorov (1941) collapses the velocity power spectra better overall

in both the inertial subrange and the dissipation range, but less so in the low wavenumber energy-containing range. The normalization proposed by vonKarman & Howarth (1938) leads to good collapse of the spectra in the energy-containing and inertial ranges, but not in the dissipation range. In contrast, the normalization proposed by George (1992) collapses the energy-containing range better than the Kolmogorov normalization, but not as well as the Von Karman and Howarth normalization. Similarly, the George normalization collapses the dissipation range better than the Von Karman and Howarth normalization, but not as well as the Kolmogorov normalization. None of the normalizations analyzed in the current study are in accord with the changing slope in the inertial subrange.

3.2 Background

Velocity power spectra provide insight into the transfer of turbulence kinetic energy from large to small scales and for that reason alone have been the subject of many studies. Various spectrum normalizations have been proposed and these too can provide insight into the energy transfer process. Kolmogorov (1941) provides a model based on energy transfer at intermediate wavenumbers, identified as the inertial subrange, where the slope of the power spectra is predicted to follow a power law and have a slope of -5/3. Immediately following this region, at higher wavenumbers, is where dissipation takes place.

3.2.1 Power Spectrum Normalization/Scaling

Kolmogorov (1941) suggests that power spectra obtained in turbulent flow are self-similar if the flows are at a sufficiently high Taylor Reynolds number, R_λ, where $R_\lambda \equiv \overline{u^2}^{1/2}\lambda/\nu$ and

where

$$\lambda \equiv u^2/\overline{(\partial u/\partial x)^2} \tag{3.1}$$

or equivalently for isotropic flows,

$$\lambda = \left(\frac{15\nu\overline{u^2}}{\epsilon}\right)^{1/2} \tag{3.2}$$

where ϵ is the dissipation rate and ν is the kinematic viscosity. For flows that are locally isotropic and where Taylor's hypothesis is valid

$$\epsilon = 15\nu\overline{\left(\frac{\partial u}{\partial x}\right)^2} = \frac{15\nu}{\overline{U}^2}\overline{\left(\frac{\partial u}{\partial t}\right)^2}. \tag{3.3}$$

In this study, the time derivative of the fluctuating velocity is measured and equation 3.3 is used to determine the dissipation rate.

Kolmogorov suggest that the power spectrum, particularly the inertial subrange and the dissipation range, can be normalized using ν, ϵ and the Kolmogorov length scale, η, where

$$\eta \equiv \left(\nu^3/\epsilon\right)^{1/4} \tag{3.4}$$

which leads to a universal form expressed as

$$\Phi_\eta(\kappa\eta) = \frac{E(\kappa)}{(\nu^5\epsilon)^{1/4}} \tag{3.5}$$

where $E(\kappa)$ is the 3-dimensional power spectrum.

George (1992) proposes a new theory of self-preservation for decaying isotropic turbulence. His theory proposes that the Taylor Microscale, λ, is the appropriate intermediate length scale that should collapse the spectra over the range of wavenumbers from the energy-containing to the dissipation range. In this normalization, the 3-dimensional spectra is found to have a universal form, $\Phi_\lambda(\kappa\lambda)$, where

$$\Phi_\eta(\kappa\lambda) = \frac{E(\kappa)}{\overline{u^2}\lambda} \tag{3.6}$$

vonKarman & Howarth (1938) (hereafter referred to as VKH) propose a third normalization where the length scale used in the normalization is the integral length scale, l. The use of the integral length scale leads to a universal form, $\Phi_l(\kappa l)$, expressed as

$$\Phi_\eta(\kappa l) = \frac{E(\kappa)}{\overline{u^2}l}. \tag{3.7}$$

3.2.2 The inertial subrange

At sufficiently high Reynolds number when the separation between the peaks in the energy spectrum and the dissipation spectrum is sufficiently large, Kolmogorov hypothesizes that an inertial subrange would be observed where energy is neither created nor dissipated but only transferred. Kolmogorov proposes that at sufficiently high values of Taylor Reynolds number, the inertial subrange would be described as

$$E(\kappa) = C\epsilon^{2/3}\kappa^{-5/3} \tag{3.8}$$

where $C = 1.5$ is a universal constant. It can be shown (cf. Pope (2000)) that if the inertial subrange of the 3-dimensional spectrum is described by equation 3.8, it follows that the 1-dimensional spectrum of the downstream velocity, $E_{11}(\kappa)$, is described by

$$E_{11}(\kappa) = C_1 \epsilon^{2/3} \kappa^{-5/3} \tag{3.9}$$

where $C_1 \approx 0.5$ (Sreenivasan, 1995). In this paper, the term "inertial subrange" will refer to the range of wavenumbers where

$$E_{11}(\kappa) \sim \kappa^{-n} \tag{3.10}$$

but where n is not necessarily 5/3.

Kolmogorov (1962) proposed one modification to the exponent expressed in equation 3.9 based on the observation that at high Taylor Reynolds numbers the energy dissipation would be intermittent. This led to the modified hypothesis for the slope of the spectra in the inertial subrange where

$$E_{11}(\kappa) = C_1 \epsilon^{2/3} \kappa^{-5/3-\mu/9} \tag{3.11}$$

where μ is the intermittency exponent (cf. Pope (2000)). The determination of μ is not part of the present study, however, early studies, as reported in Monin and Yaglom (1975), suggest that μ varies from 0.1 to 0.8. The more recent study of Sreenivasan and Kailasnath (1993) concludes that $\mu = 0.25 \pm 0.05$ for flows with R_λ in the range of 1500 to 2000.

The prediction that the inertial subrange should be described by equations 3.9 or 3.11 is well documented for high Taylor Reynolds number flows. For example, Praskovsky & Oncley

(1994), hereafter referred to as PO94, present spectra obtained in the atmospheric boundary layer with corresponding R_λ values between 2.8×10^3 and 12.7×10^3 and find values for the slope in the inertial range close to $-5/3$.

In contrast for $50 \leq R_\lambda \leq 473$, Mydlarski & Warhaft (1996), hereafter referred to as MW96, find that while an inertial subrange of the general form described by equation 3.10 exists, n varies with R_λ as

$$n = 5/3 - 5.25 R_\lambda^{-2/3} \tag{3.12}$$

Even though an inertial subrange is observed at R_λ as low as 200, $n = 1.5$ which is significantly less than $5/3$.

The goals of the study reported herein are as follows:

1. To determine how n varies with R_λ for the range $194 \leq R_\lambda \leq 997$.

2. To compare the results for n obtained in the current study to corresponding results in similar and different flows.

3. To assess the applicability of the spectral normalization models proposed by Kolmogorov (1941), vonKarman & Howarth (1938) and George (1992).

3.3 Experimental Setup

3.3.1 Flow Facilities and Active Grid

This experiment is conducted in the large, closed-return wind tunnel at the University of California, Irvine. The tunnel has a rectangular test section that is 0.91 m tall, 0.61 m wide, 6.71 m long and is preceded by a contraction section with an area reduction ratio of 9.36. An active grid similar to the one proposed by Makita & Sassa (1991) is used to produce high intensity, nearly homogeneous and isotropic flow. The rod rotation of the active grid is controlled by two microcontrollers that are programmed to rotate the rods in a random direction at a random rate of 2 ± 0.5 rev/sec. The microcontrollers randomly change the rotation rate and direction every 250 ± 125 $msec$. Details on the design and operation of the active grid can be seen in the experimental section in Chapter 2.

Although grid parameters are randomized, a relative peak appears at twice the average rotation rate of the rods, in this case 4 Hz. Figure 3.1 shows velocity power spectra with mean velocities of 4 and 12 m/s at $x/M = 36$ where x is the coordinate position in the downstream direction with origin at the grid and M is the mesh length or spacing between rods. The relative peak grows larger as the mean velocity increases and, at most, has a magnitude of a fraction of a decade. The relative peak increases the velocity variance less than 1% and, as a result, the velocity variance is not corrected. In order to reduce noise, spectra are computed from the average of 120 1-second time records.

3.3.2 Sensors and signal conditioning

The time-resolved velocity is measured using a standard, one-component hot-wire sensor whose sensing element is a 5.08 μm diameter Wollaston platinum wire that is operated

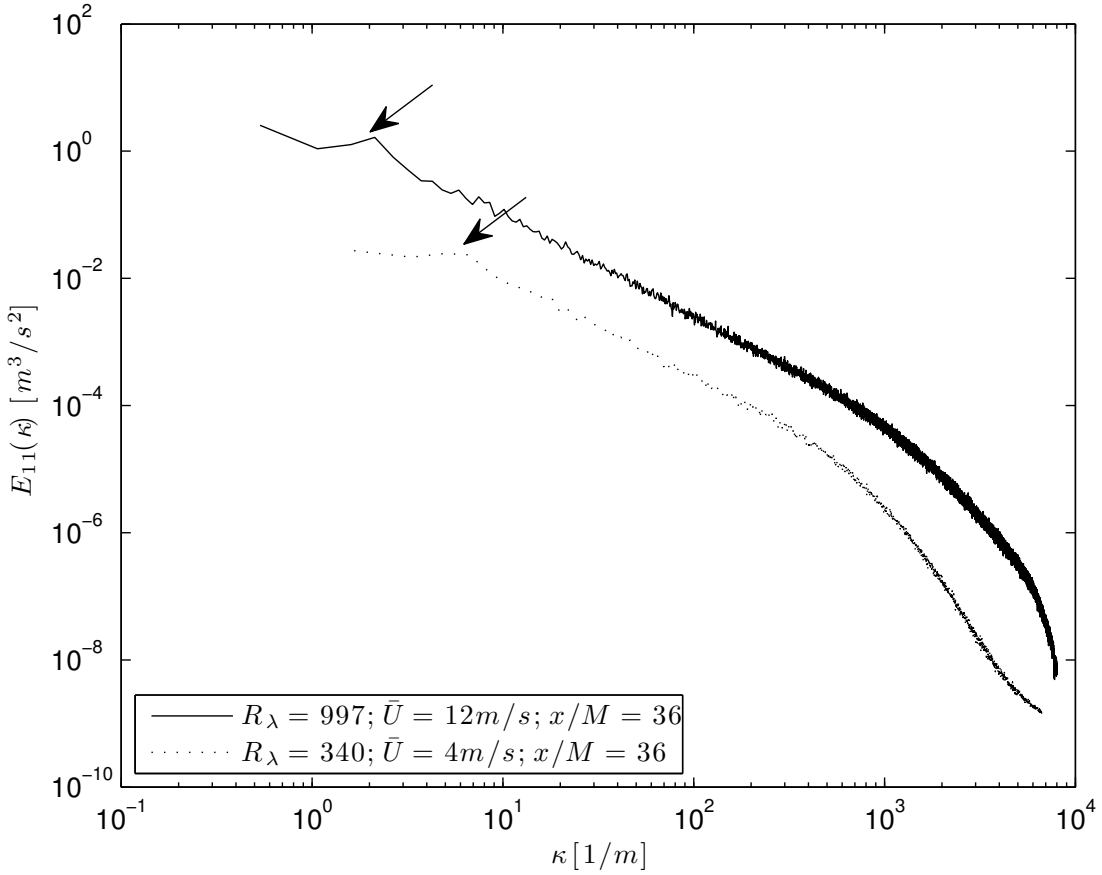

Figure 3.1: Velocity power spectra obtained at $x/M = 36$. Arrows denote the relative peaks corresponding to a frequency equal to twice the rotation rate of the active grid rods, which increase the velocity variance by less than 1%.

in constant temperature mode. The length of the platinum wire is nominally 1 mm, which yields a length to diameter ratio of about 200. This is the optimal ratio Azad (1993) suggests so as to minimize prong effects and maximize spatial resolution. The spatial averaging due to the finite length of the sensing wire decreases the velocity variance by less than 1% and, therefore, no correction is made to the velocity power spectra (cf. Wyngaard (1968)). The sensor is calibrated before and after each data collection period to ensure the sensor is stable. Data are discarded if the statistics of interest vary by more than 1% when analyzed using both calibrations.

The signal from the hot-wire is filtered using an analog, low pass, 4-pole Butterworth filter

which incorporates a Frequency Devices (744PB-4) module. The signal is amplified using a 3-stage amplifier that has a frequency response of approximately 70 Hz. The time derivative is obtained by passing the signal through a low noise, analog differentiator with a bandwidth of approximately 18 kHz. All signals are digitized using a 16-bit Measurement Computing Corp. 1608-HS analog to digital converter with 8 differential analog inputs. Data reduction and preliminary analysis is done using $LabView2013$.

3.3.3 Hot-wires in high intensity turbulent flows

A hot-wire can exhibit large measurement errors if placed in high intensity turbulence, defined as $\overline{u^2}^{1/2}/\overline{U}$. For example, hot-wires cannot measure near zero or reverse flows, which are conditions that could occur if the turbulence intensity is high enough. Bradbury (1976) compares measurements from a traditional single hot-wire to a pulsed-wire hot-wire, which is able to accurately measure velocity in flows with turbulence intensities of up to 50%. He finds that the turbulence intensity has an error of about 2 and 4% using the standard hot-wire at turbulence intensities at 20 and 30%, respectively. For results presented in this study, the maximum turbulence intensity is 20% where the error due to high turbulence intensity would, based on the study of Bradbury (1976), be expected to be about 2%. Therefore, no correction to account for high intensities or velocity variance is applied.

It has been shown (Wyngaard & Clifford, 1977; Sreenivasan, 1965) that high turbulence intensity could also cause errors in the use of Taylor's hypothesis when approximating the variance of the spatial derivative of downstream velocity, $\overline{(\partial u/\partial x)^2}$, with the variance of the temporal derivative of the downstream velocity, $\overline{(\partial u/\partial t)^2}$ as is done when measuring the Taylor Microscale, λ, and the Kolmogorov length scale, η, described in equations 3.2 and 3.4, respectively. Heskestad (1965) shows that a "generalized Taylor's hypothesis" can be used to accurately transform $\overline{(\partial u/\partial t)^2}$ to $\overline{(\partial u/\partial x)^2}$. Applying the generalized Taylor's hypothesis to

data corresponding to the highest turbulence intensity in the current study leads to a 4.8% and 2.4% error in the measured value of λ and η, respectively. These corrections are small relative to the magnitude of the trends seen in the data, therefore, no correction is deemed necessary.

3.3.4 Determination of the integral length scale

The integral length scale is determined from the integral time scale, which is defined as

$$T = \int_0^{\tau=\infty} \rho(u(x,t)u(x,t+\tau))d\tau \tag{3.13}$$

where

$$\rho(u(x,t)u(x,t+\tau)) = \frac{\overline{u(x,t)u(x,t+\tau)}}{u(x,t)^2} \tag{3.14}$$

is the time autocorrelation of the velocity. The integral length scale is then determined from

$$l = \overline{U}T \tag{3.15}$$

where $\overline{U}$ is the mean speed. This approach can be used to accurately determine the integral length scale for flows with turbulence intensity of up to 25% (Nobach & Tropea, 2012). The approach used to measure integral length scale is described in detail in Chapter 2.

$\overline{U},\ m/s$	x/M	R_λ
4	$35 - 143.5$	$194 - 340$
8	$35 - 143.5$	$365 - 699$
12	$35 - 143.5$	$510 - 997$

Table 3.1: Experimental parameters

R_λ	218	340	365	523	525	699	997
x/M	88	36	143.5	62	136	36	38
$\overline{U},\ m/s$	3.81	3.78	8.01	8.01	11.6	7.84	11.8
$\overline{u^2},\ m^2/s^2$	0.099	0.382	0.312	1.09	0.920	2.280	5.764
$\epsilon,\ m^2/s^3$	0.194	1.210	0.698	4.13	2.927	10.16	31.92
$l,\ m$	0.133	0.123	0.160	0.160	0.214	0.176	0.259
$\lambda,\ mm$	1.09	0.86	1.02	0.79	0.86	0.73	0.65
$\eta,\ mm$	0.38	0.24	0.27	0.17	0.19	0.14	0.10

Table 3.2: Flow parameters for the cases shown in the spectrum normalization section.

3.3.5 Experimental parameters

An R_λ range of 184 to 997 is achieved by varying mean speed, $\overline{U}$, and downstream location from the active grid, x/M. The mean velocities, downstream position ranges and corresponding Taylor Reynolds number ranges are shown in table 3.1. The evolution of spectra and their normalization is studied using a subset of the data set. The flow parameters for data chosen for the spectral comparisons are shown in table 3.2. The two spectra taken at $R_\lambda = 523$ and 525 can help illuminate how spectra with similar Taylor Reynolds number, but different flow parameters, i.e. $\overline{u^2}$, ϵ, etc., vary and respond to the different normalizations.

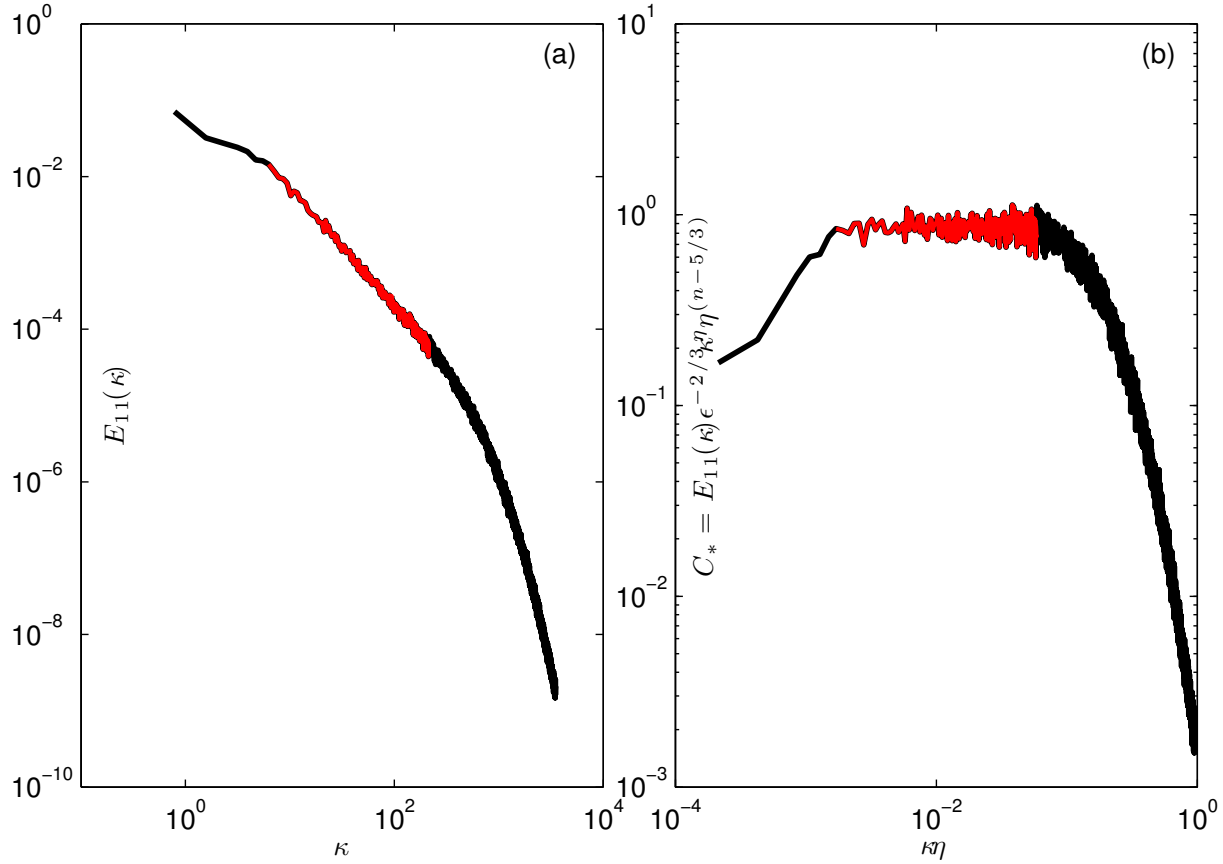

Figure 3.2: Velocity power spectrum (a) and compensated velocity power spectrum (b) obtained at $R_\lambda = 365$. The slope of the inertial subrange, n, is chosen such that the inertial subrange is has zero slope.

3.3.6 Analysis procedure

One of the goals of this study is to determine the slope and the wavenumber corresponding to the beginning and end of the inertial subrange as a function of Taylor Reynolds number, R_λ. The process used to determine the aforementioned parameters is presented next.

A velocity spectrum for $R_\lambda = 365$ is shown on figure 3.2(a). The inertial subrange can be observed as the region in red of constant slope. It is important to note that the electronic noise is reached at a wavenumbers well above the end of the inertial subrange and contributes less than 2% to the measured value of $\overline{u^2}$ for all spectra presented herein.

The determination of the slope of the inertial subrange is based on the approach used by MW96 where the following modified form is used:

$$E_{11}(\kappa) = C_1^* \epsilon^{2/3} \kappa^{-5/3} (\kappa\eta)^{5/3-n} \tag{3.16}$$

where n is the slope of the inertial subrange and C_1^* is a modified Kolmorov constant. The slope is found by adjusting n until a value is reached where the slope of the compensated spectrum in the inertial subrange is zero as shown on figure 3.2(b), which in this case leads to a value of $n = 1.55$.

To ensure repeatability and consistency, a $MATLAB$ program (see Appendix A) is used to determine the slope and extent of the inertial subrange. An initial estimate of the beginning and end points of the inertial subrange is supplied to the program and the slope of the inertial subrange is determined using the method of least squares. The amount that the slope of the least squares fit line deviates from zero (β^*) is a measure of how much the slope of the original velocity power spectrum deviates from $-5/3$. The exponent on κ is then corrected by β^* and the slope of the new compensated velocity power spectrum ($E_{11}(\kappa) \times \kappa^{5/3-\beta^*}$) is found. This iterative process is repeated until the slope correction, β^*, falls below a certain threshold, in this case, 0.00005.

The next step is to find values for the wavenumbers at the beginning and end of the inertial subrange. Due to the variability in the value of the power spectra, the spectra are smoothed using a 20-point running average. The wavenumber corresponding to the beginning of the inertial subrange is identified as the wavenumber location where the power spectral value of the averaged spectra first crosses the fitted horizontal line. The wavenumber corresponding to the end of the inertial subrange is identified as the wavenumber location where the power spectral value of the averaged spectra last crosses the fitted horizontal line.

3.4 Results

3.4.1 Evolution of the inertial subrange

While the slope of the velocity power spectrum is a constant with respect to wavenumber in the inertial subrange, the slope is not a constant and varies as a function of R_λ. Figure 3.3 shows the slope of the inertial subrange, n, as a function of R_λ for the current study. The solid line represents a least squares curve fit of the data for $185 \leq R_\lambda \leq 997$ with the corresponding prediction that $n = 1.66 - 20R_\lambda^{-0.889}$, which suggests that n asymptotically approaches 1.66 ± 0.066 with increasing R_λ. Note that there appears to be a significant decrease in the scatter of the slope of the inertial subrange with increasing R_λ. This occurs because the width (in wavenumber) of the inertial subrange increases with increasing R_λ leading to a more accurate measure of the slope. Although the uncertainty of the asymptotic value that n approaches is only $\pm 4\%$, the uncertainty with respect to the intermittency exponent, μ, is too large (± 0.55) to make any reliable estimate of its value.

As noted, spectra obtained close to the grid show a relative peak at 4 Hz (twice the rotation rate of the grid rods). In order to assess whether the relative peak has an effect on the slope of the inertial subrange, the grid is programmed to run in synchronous mode. This mode causes all the rods to rotate at the same speed and direction, which transforms the small relative peak to a relatively high amplitude peak. Figure 3.3 shows data taken with the active grid programed to rotate the rods synchronously and it is clear that the larger, more pronounced peak has not significantly affected the value of the slope. Thus, it would appear that the presence of the relative peak at 4 Hz does not have a significant effect on the energy transfer in the inertial subrange. Figure 3.3 also shows data from MW96 obtained in the flow downstream of an active grid and Saddoughi & Veeravalli (1994), hereafter referred to as SV94, which are measurements taken in a turbulent boundary layer. Similar to the current study, their data show n increasing with increasing R_λ signifying that the changing

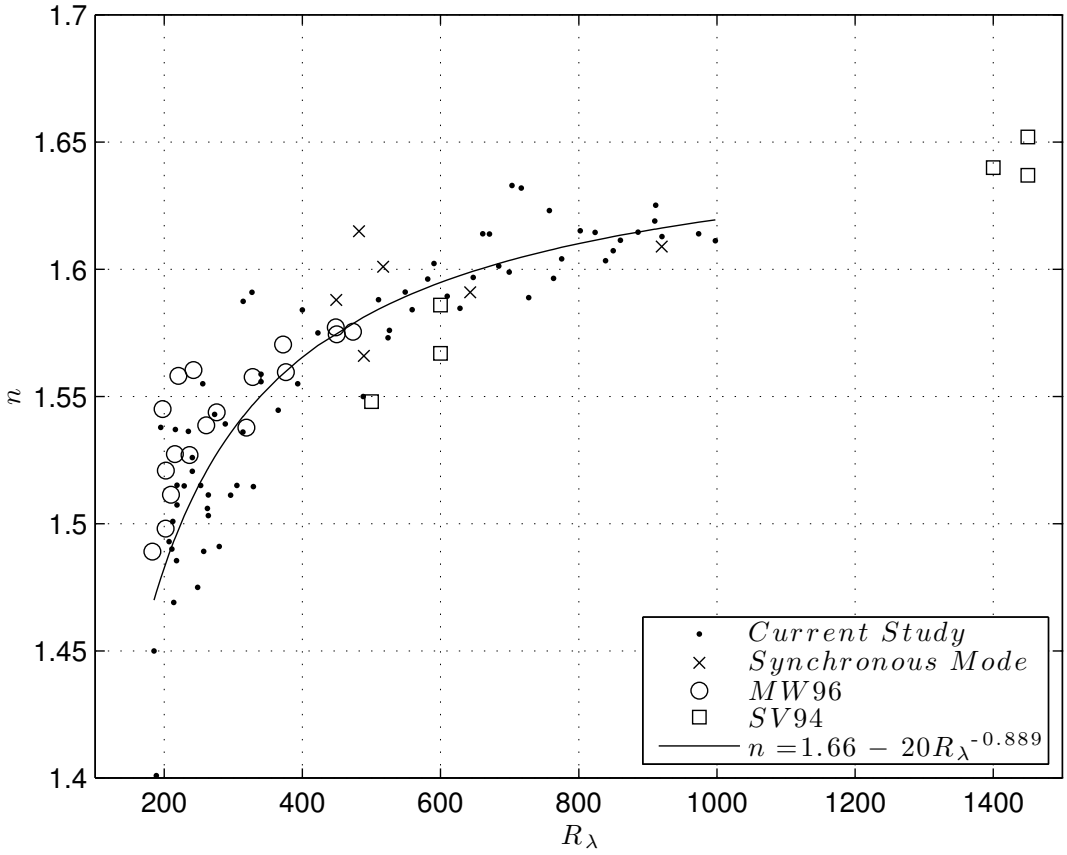

Figure 3.3: The slope of the inertial subrange as a function of Taylor Reynolds number for the current study along with data from MW96 and SV94. The solid line represents a least squares curve fit of the data from the present study.

slope of the inertial subrange is not dependent on the type of flow.

Figure 3.4 shows n as a function of R_λ with data at higher values of R_λ obtained from PO94, which include measurements taken in a mixing layer and an atmospheric surface layer. The solid line corresponds to a least squares curve fit for values of n from the present study only which has been extrapolated to $R_\lambda = 13000$. The dashed line corresponds to a least squares curve fit for all the data included in figure 3.4 where

$$n = 1.69 - 5.86R_\lambda^{-0.645} \tag{3.17}$$

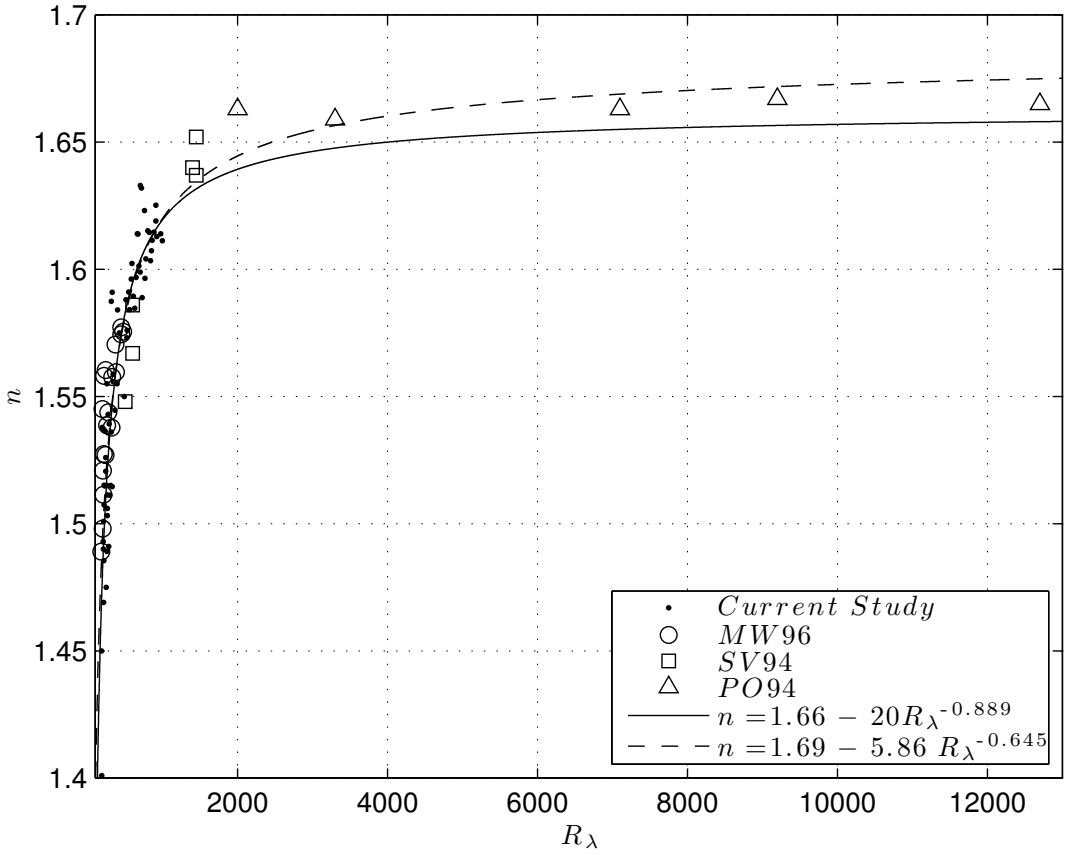

Figure 3.4: The slope of the inertial subrange versus Taylor Reynolds number for the current study, MW96, SV94 and PO94. The dashed line corresponds to a least squares curve fit for all the data.

leading to an asymptotic value for n of 1.69 ± 0.036. With the added data, the uncertainty of the asymptotic value of n decreases from $\pm 4\%$ to $\pm 2.1\%$. However, the uncertainty of μ (± 0.3) is still too large to make any conclusive statement regarding its value.

Since the accuracy of the measurement of n is a function of the length of the inertial subrange, the width of the inertial subrange as a function of R_λ is of interest. An inertial subrange is difficult to observe at low values of R_λ as evidenced by velocity power spectra obtained downstream of passive biplane grids (Alkudsi, 2012). It is likely that a minimum R_λ value may be required to obtain an observable inertial subrange. Figure 3.5 shows the width of the inertial subrange, w, as a function of R_λ. The solid line corresponds to a least squares

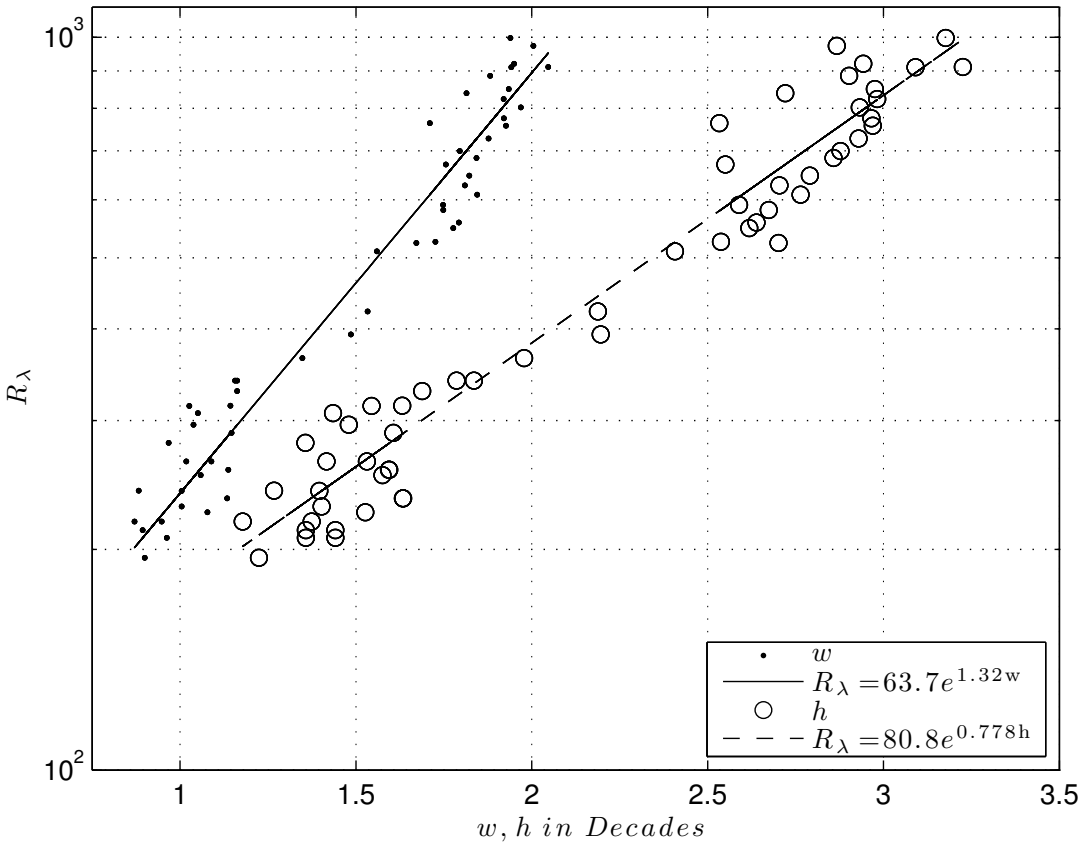

Figure 3.5: Taylor Reynolds number versus width and height of the inertial subrange in decades of wavenumber and energy, respectively. The solid and dashed lines corresponds to a least squares curve fit of the width and height, respectively.

curve fit, which shows that

$$R_\lambda = 63.7e^{1.32w} \tag{3.18}$$

Equation 3.18 suggests that an R_λ value of about 64 is needed for $w > 0$. However, qualitatively it is difficult to identify an inertial subrange accurately for $R_\lambda \leq 190$.

Figure 3.5 also shows the height of the inertial subrange, h, in decades as a function of R_λ.

The dashed line corresponds to a least squares curve fit where

$$R_\lambda = 80.8e^{0.78h} \tag{3.19}$$

Equation 3.19 suggests that an R_λ value of about 81 is needed for $h > 0$, which is reasonably close to the limiting R_λ value found for w.

It is well understood (cf. Tennekes & Lumley (1972), Libby 1996, Pope (2000)) that an inertial subrange will only be observed for large separation of the peaks of the energy and dissipation spectra. The separation of the peaks as a function of $\kappa\eta$ is shown in figure 3.6 and the separation is well described by a linear function of R_λ. The solid line on figure 3.6 corresponds to a linear least square fit where

$$\kappa\eta = 0.000415R_\lambda + 0.00238 \tag{3.20}$$

Equation 3.17 shows that $R_\lambda > 3000$ is needed for the slope of the inertial subrange to be within 2% of its plateau value. Equation 3.20 suggests that for this to occur, the separation between the peaks of the energy and dissipation spectra needs to be $\kappa\eta > 3.61$.

3.4.2 Spectrum normalization

Spectra analyzed herein correspond to values of R_λ that vary from 194 to 997. A subset of the spectra obtained in the present study is shown in figure 3.7 and flow parameters corresponding to these spectra are shown in table 3.2. Except at the high frequency portion of the spectra, values of $F_{11}(f)$ for any fixed frequency can be seen to increase with increasing R_λ. Note that in the inertial subrange the values for F_{11} are nearly the same when R_λ values

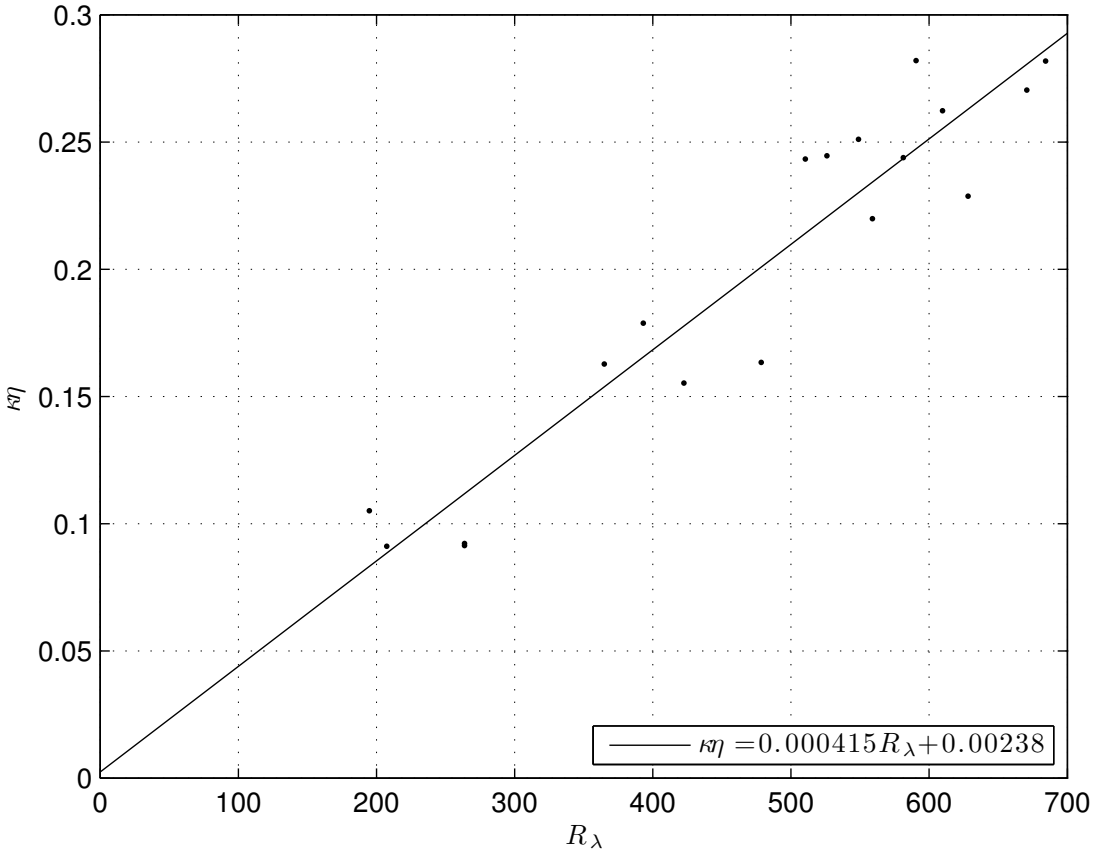

Figure 3.6: Distance between the peak of the energy spectrum and the dissipation spectrum as a function of Taylor Reynolds number.

are the same even when the mean velocity and the velocity variance differ significantly. For example the two power spectra corresponding to $R_\lambda = 525$ and 523 with corresponding mean velocities of 12 and 8 m/s and values of $\overline{u^2}$ of 0.920 and $1.089 m^2/s^2$, respectively, have nearly identical values of F_{11} in the inertial subrange, but differ in the dissipation range. Leading to the observation that the values of $F_{11}(f)$ of the power spectra in the inertial subrange appear to be functions of R_λ.

The seemingly organized manner in which the velocity power spectra, when plotted as a function of frequency, vary with R_λ is not so obvious when plotted as function of wavenumber, $\kappa = 2\pi f/\overline{U}$, where $E_{11}(\kappa) = (\overline{U}/2\pi)F_{11}(f)$ as be seen in figure 3.8. Focusing on the same

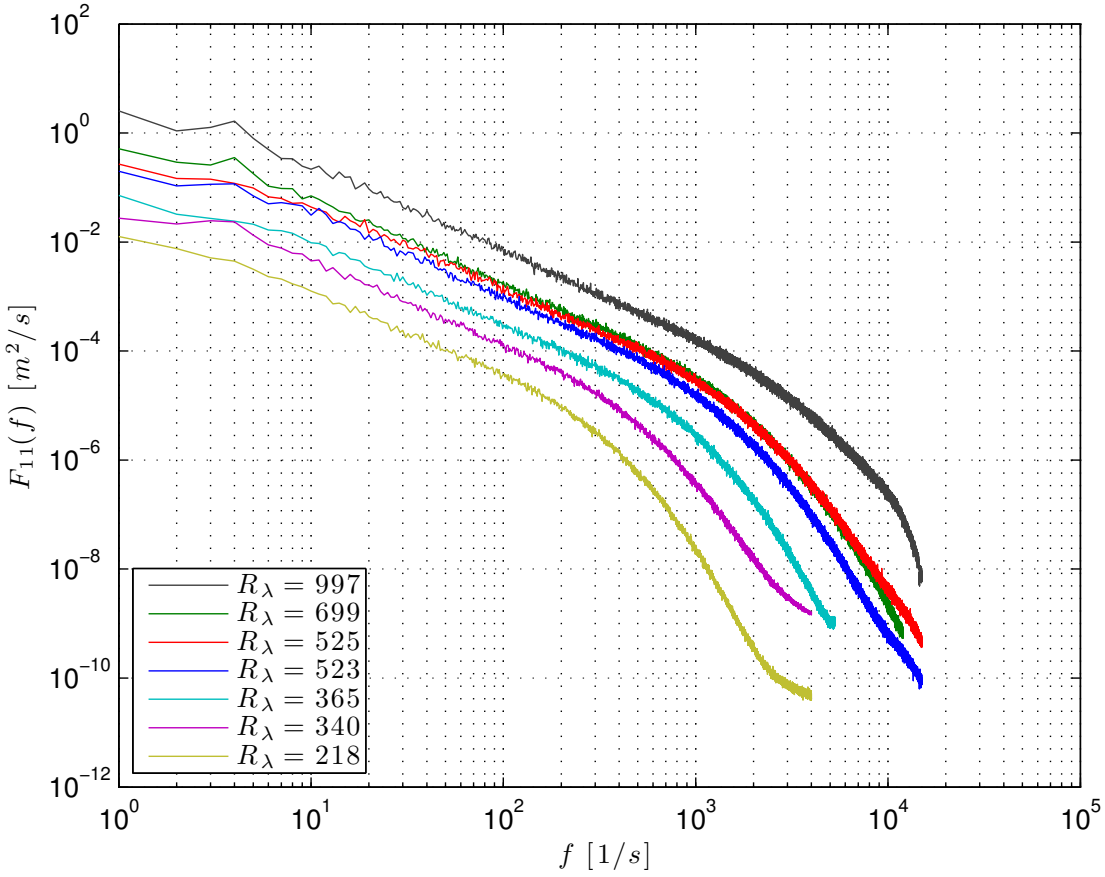

Figure 3.7: $F_{11}(f)$ versus f for various Taylor Reynolds numbers and mean speeds

two power spectra as before with similar values of R_λ, it is clear that the inertial subrange region no longer matches.

3.4.3 Spectrum normalization/comparison

The effect of applying each normalizations to the power spectra are first considered qualitatively and then quantitatively. As discussed in the background section, the three normalizations are the ones proposed by Kolmogorov (1941), vonKarman & Howarth (1938) and George (1992). It should be noted that while it has been shown in the data presented herein that the slope of the inertial subrange increases with increasing R_λ, none of the

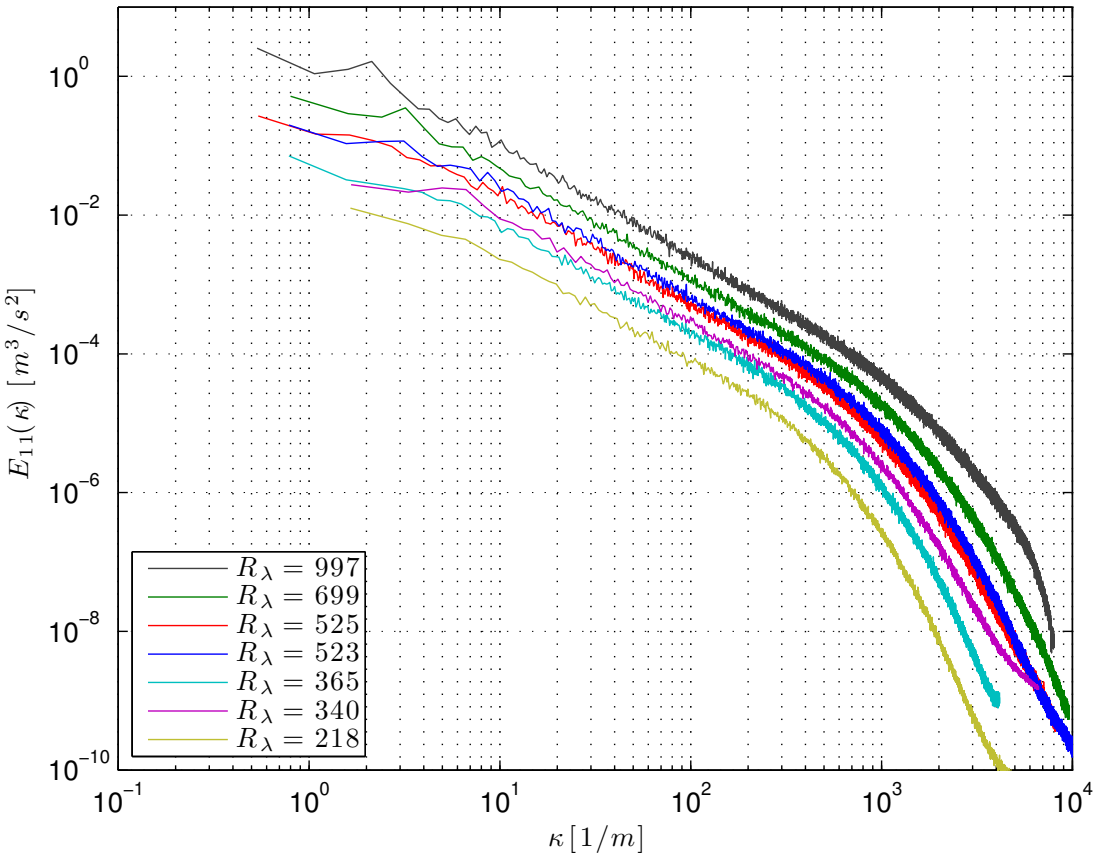

Figure 3.8: $E_{11}(\kappa)$ versus κ for various Taylor Reynolds numbers and mean speeds

normalizations account for the variation of the slope of the inertial subrange. However, notwithstanding this observation, comparisons of the effect of the three normalizations will provide a means to assess their applicability.

The velocity power spectra scaled by the normalization proposed by VKH are shown in figure 3.9. Equation 3.7 shows that this normalization is based on the integral scale of the flow, therefore it is not surprising that the energy-containing region of the spectrum collapses rather well. Furthermore, it can be observed that the normalized spectra are in good agreement up to about $\kappa l \approx 50$ where the normalized spectra begin to deviate. Clearly and as expected, this normalization does not lead to a good match of the normalized spectra in the high wavenumber dissipation range.

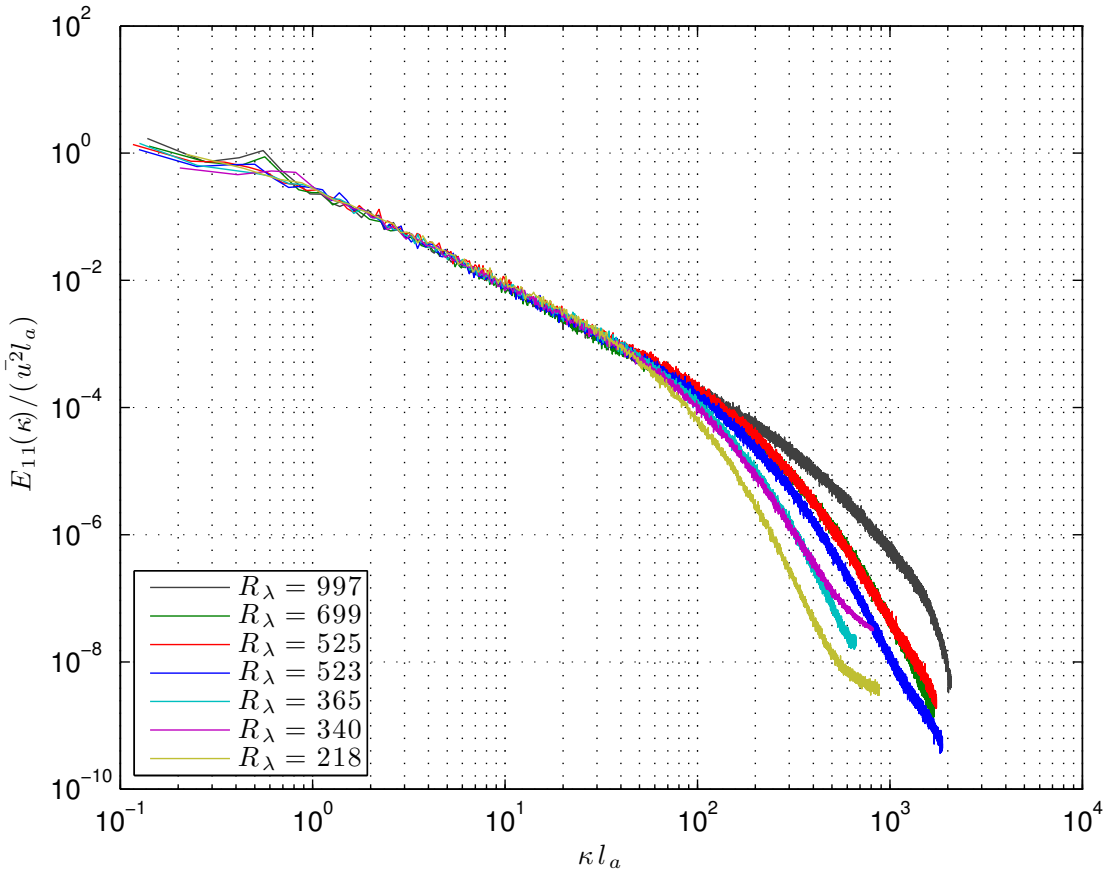

Figure 3.9: Velocity power spectra for various Taylor Reynolds normalized by the VKH normalization.

Figure 3.10 shows the velocity power spectra normalized using the scaling proposed by George (1992), which utilizes the Taylor Microscale as the normalizing length scale. This normalization leads to a reasonably good collapse for all normalized wavenumbers showing significant improvement in the dissipation range when comparing to the normalization proposed by VKH. The collapses in the energy containing range and the inertial subrange is not as good as the collapse obtained using the VKH's normalization, however.

Figure 3.11 shows the effect of the normalization proposed by Kolmogorov (1941) where the normalization is based on the Kolmogorov length scale, η, the dissipation rate, ϵ, and the kinematic viscosity, ν. Although the normalizing length scale is small compared to the scales

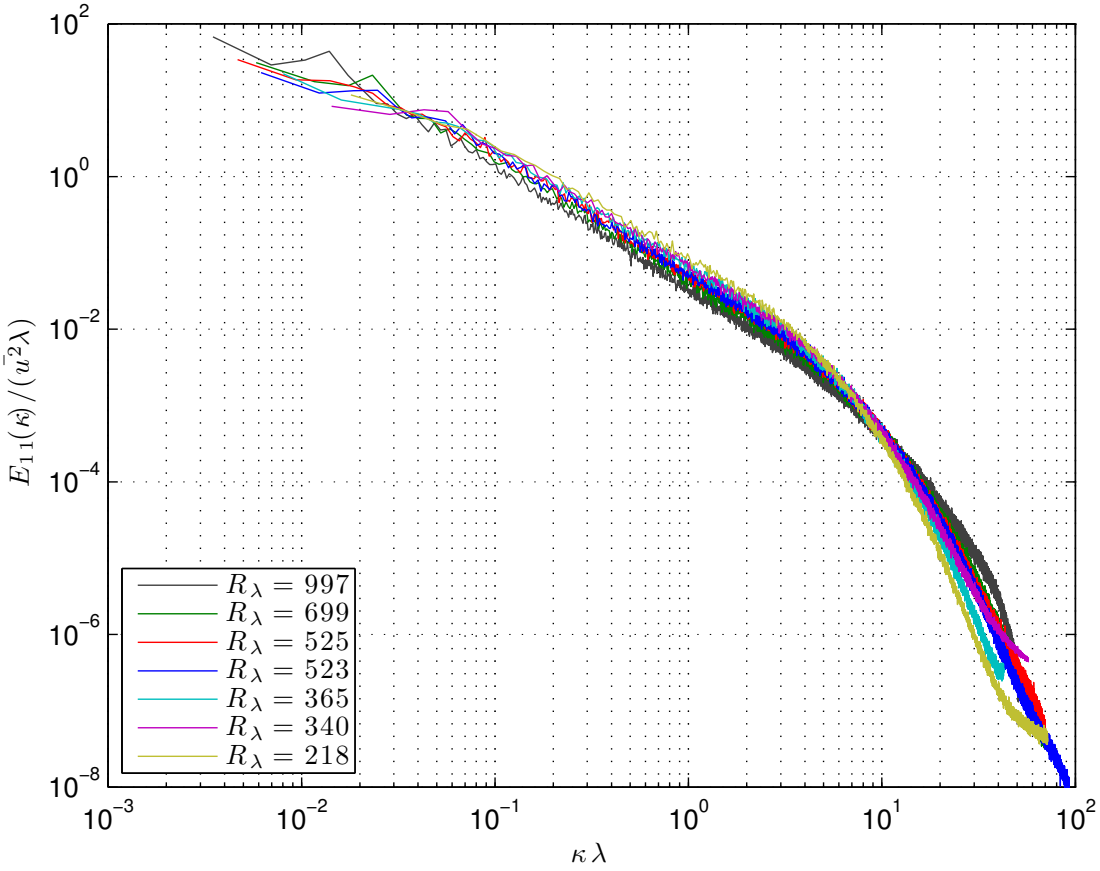

Figure 3.10: Velocity power spectra for various Taylor Reynolds normalized by the George (1992) normalization.

of other normalizations, Kolmogorov's normalization shows an excellent collapse in both the inertial subrange and dissipation range. The spectra do not collapse as well in the energy containing range as they do when employing the George or VKH normalizations.

The qualitative assessment of the three normalizations suggests the normalization proposed by George and VKH collapse the energy containing range better than the Kolmogorov normalization. However the normalizations proposed by VKH and Kolmogorov lead to a relatively better collapse of the spectra in the inertial subrange with Kolmogorov's normalization leading to the best collapse in the dissipation range.

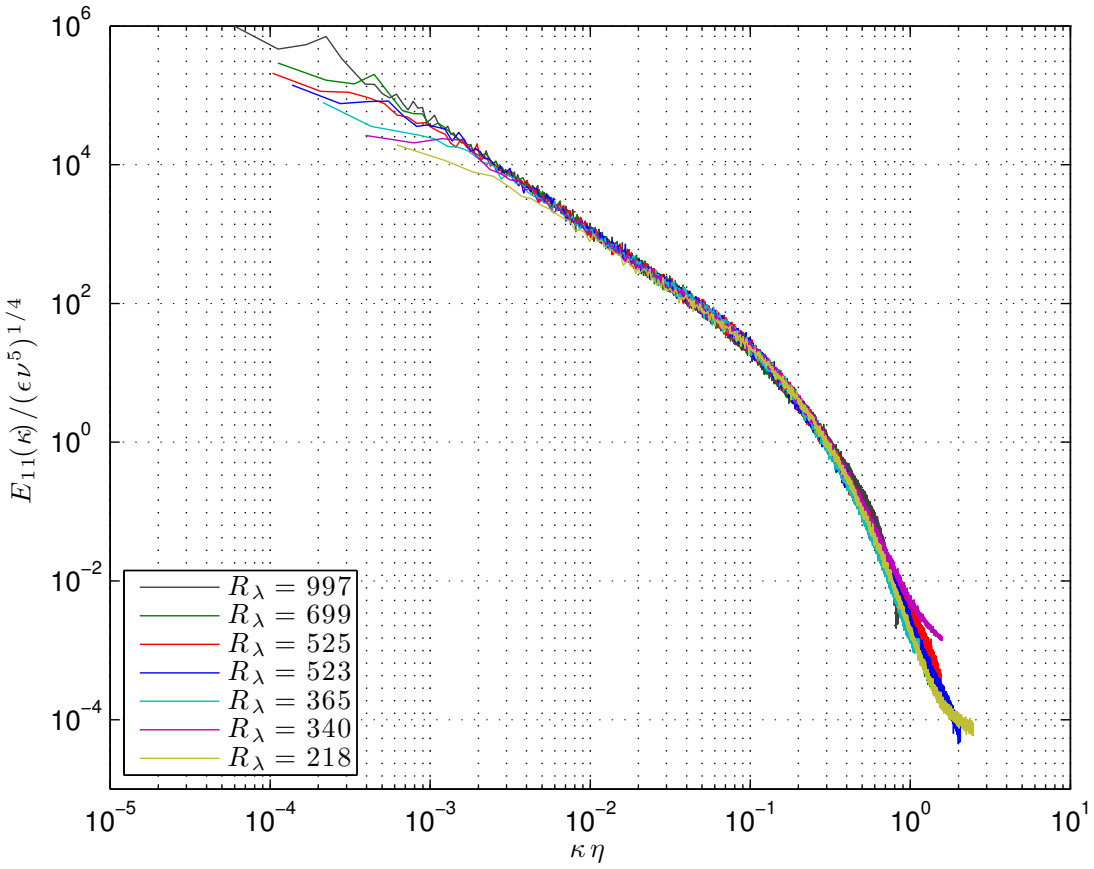

Figure 3.11: Velocity power spectra for various Taylor Reynolds normalized by the Kolmogorov (1941) normalization.

3.4.4 Quantitative analysis on the effectiveness of the normalizations

Next is considered a more quantitative based assessment of the effectiveness of the three normalizations. As noted in section 3.2.1, since each of the normalizations use different scales to normalize the spectra, it is expected that the different normalizations collapse the spectra better in different wavenumber ranges. For that reason, the normalized spectra are divided up into ranges that include the inertial subrange ($I.S.$) and 3 subranges in the dissipation range ($D1$, $D2$ and $D3$) as shown in table 3.3. Due to the inability of VKH's normalization to collapse the dissipation range of the spectrum, it is not included in the

–	$I.\ S.$	$D1$	$D2$	$D3$
$\kappa\eta$	$0.0097 - 0.035$	$0.062 - 0.067$	$0.140 - 0.146$	$0.224 - 0.230$
$\kappa\lambda$	$0.29 - 1.06$	$3.83 - 4.18$	$8.70 - 9.05$	$13.9 - 14.3$
κl	$4.29 - 12.86$	$--$	$--$	$--$

Table 3.3: Normalized wavenumber ranges used to compare the normalizations proposed by Kolmogorov ($\kappa\eta$), George ($\kappa\lambda$) and VKH (κl).

quantitative comparison the dissipation range. Unfortunately, the relative peak at 4 Hz, which can be noticed in some of the power spectra, obscures the quantitative comparison of the collapse in the energy-containing region of the spectra. For that reason, no quantitative assessment is conducted in this region.

The normalized spectral values within each normalized wavenumber range are averaged and the collapse is then assessed by comparing the difference of each average to that of a reference spectrum. In this case, the reference spectrum is the spectrum obtained for $R_\lambda = 997$ and the differences are computed as

$$C_\xi = \frac{\frac{E_{11}(\kappa)}{\xi} - \frac{E_{11,ref}(\kappa)}{\xi_{ref}}}{\frac{E_{11,ref}(\kappa)}{\xi_{ref}}} \tag{3.21}$$

where $\xi = (\epsilon\nu^5)^{1/4}$, $\xi = \overline{u^2}\lambda$ or $\xi = \overline{u^2}l$ for the normalizations proposed by Kolmogorov, George and VKH, respectively.

Figure 3.12 shows the spectral comparison in the inertial subrange for all three normalizations as a function of R_λ. By definition (cf. equation 3.21), $C_\xi = 0$ for the inertial subrange of the spectrum corresponding to $R_\lambda = 997$. If a normalization worked perfectly, C_ξ would equal zero for spectra at all R_λ values. Figure 3.12 shows an excellent collapse for $R_\lambda > 350$ for both the Kolmogorov ($\xi = (\epsilon\nu^5)^{1/4}$) and VKH's ($\xi = \overline{u^2}l$) normalizations. At $R_\lambda < 350$, the collapse for both normalizations begins to deviate from the reference spectrum, something

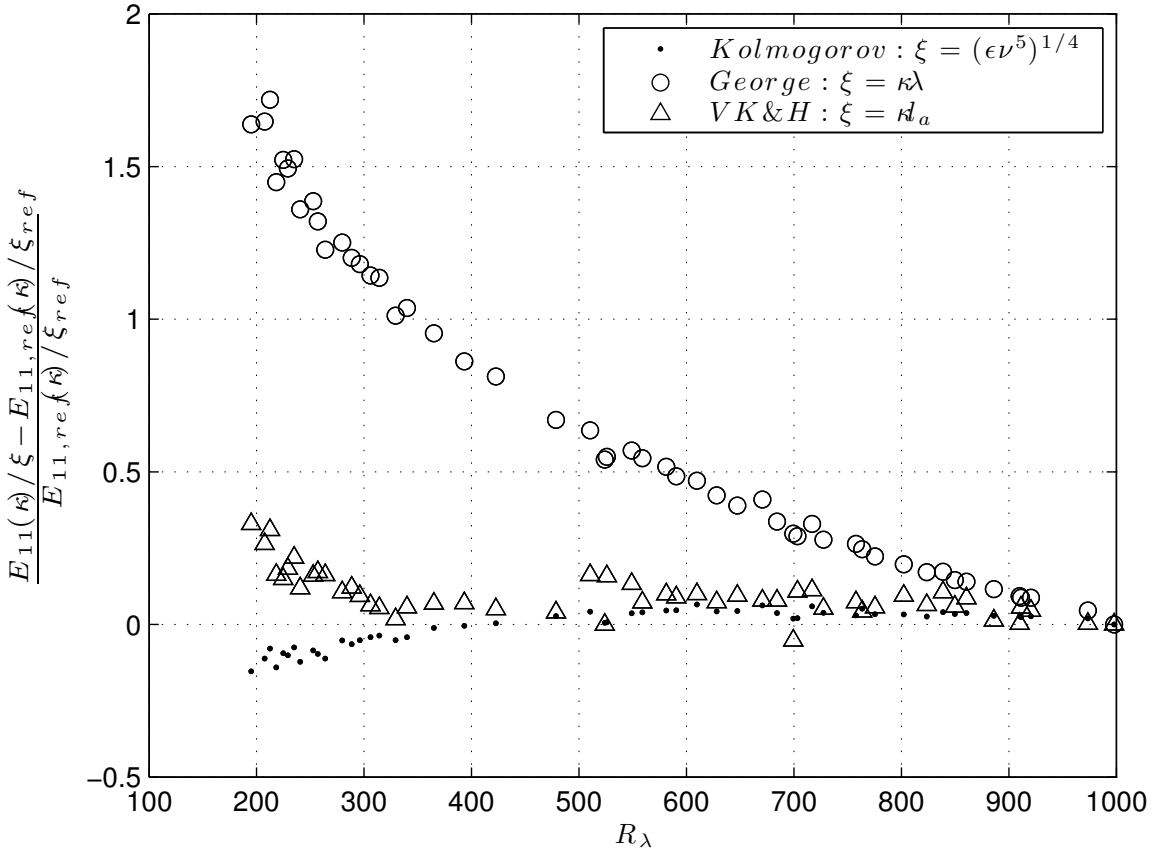

Figure 3.12: Effectiveness of normalizations in collapsing the inertial subrange ($I.S.$) when applying the normalizations proposed by VKH (1938), George (1992) and Kolmogorov (1941).

that is not obvious from the qualitative observation based on figure 3.9 and figure 3.11.

Another assessment of the normalizations is based on the observation that the high wavenumber extent of the inertial subrange should also have an identical normalized value. Figure 3.13 (a), (b) and (c) show the normalized wavenumber location that represents the high wavenumber extent of the inertial subrange as a function of R_λ for the normalizations proposed by George, Kolmogorov and VKH, respectively. For the normalization proposed by George (figure 3.13(a)), the normalized high wavenumber extent of the inertial subrange initially increases with increasing wavenumber, but appears to reach a nearly constant value starting at about $R_\lambda = 550$ with a peak to peak variation of about $\pm 20\%$. For the nor-

malization proposed by Kolmogorov (figure 3.13(b)), The location of the normalized high wavenumber extent of the inertial subrange appears to reach a constant value for $R_\lambda \geq 350$ but with a peak to peak variation of about $\pm 14\%$. For the normalization proposed by VKH (figure 3.13(c)), the normalized value of the high wavenumber extent of the inertial subrange does not appear to approach a constant value but rather to increase with increasing wavenumber.

Next, the effectiveness of the normalizations proposed by George and Kolmogorov in the dissipation subranges are determined and shown in figure 3.14(a), (b), and (c). The variation of C_ξ with R_λ is much smaller for the Kolmogorov normalization in comparison to the variation found in the George normalization. Figure 3.14(b) shows a reduction in the variation of C_ξ with R_λ for the George normalization, which coincides with the wavenumber range in figure 3.10 where the normalized spectra appear to cross over each other.

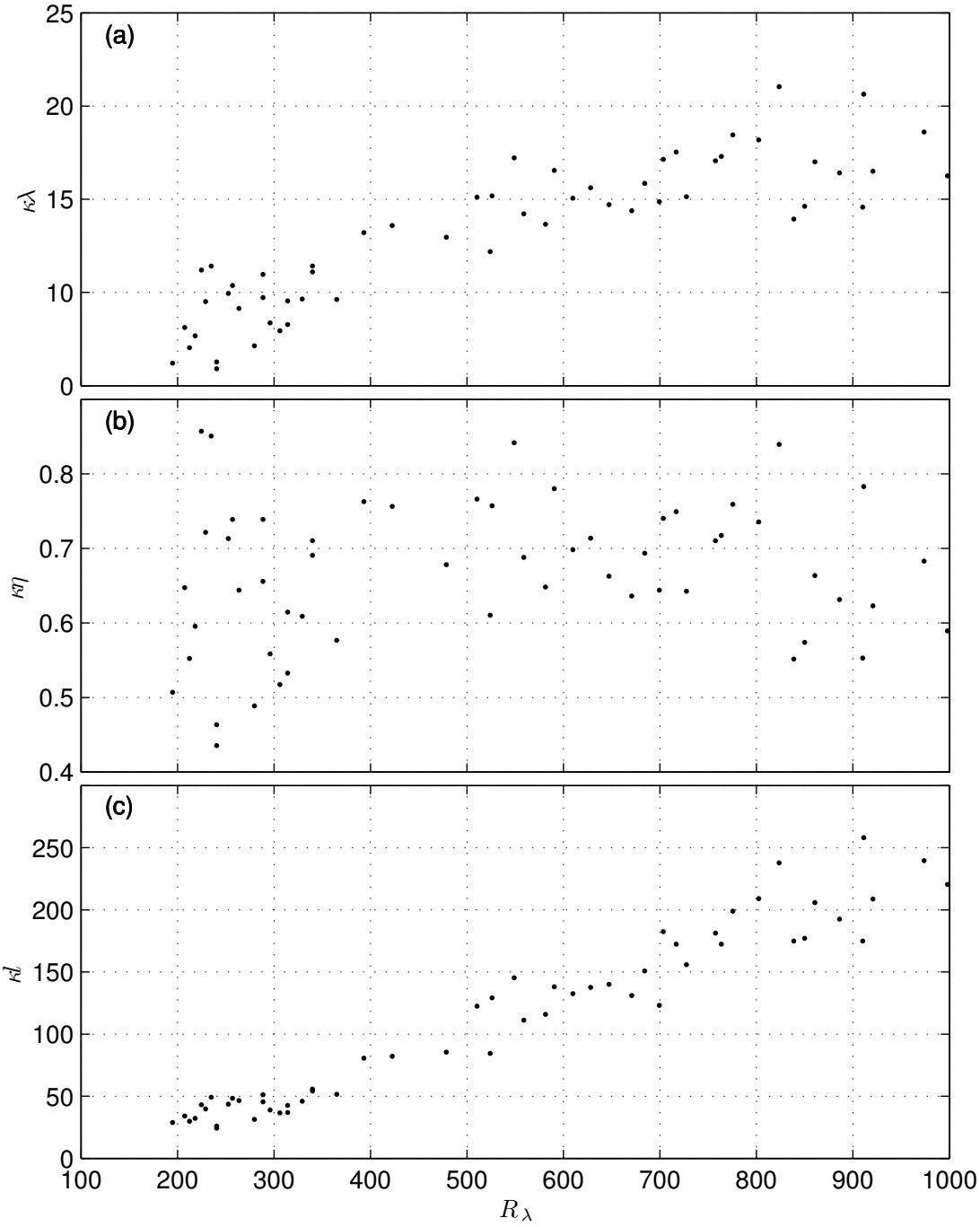

Figure 3.13: Location of the normalized high wavenumber extent of the inertial subrange as a function of R_λ using George's normalization (a), Kolmogorov's normalization (b) and VKH's normalization (c).

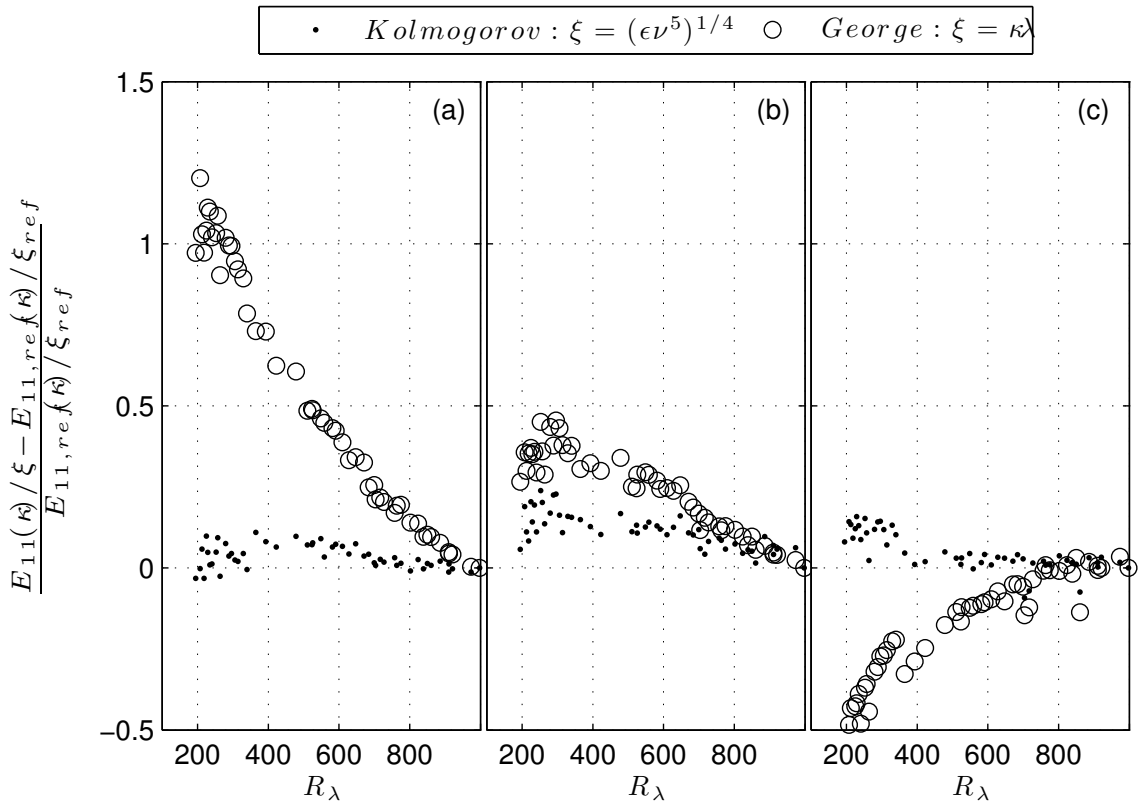

Figure 3.14: Effectiveness of normalizations in collapsing the ranges $D1$ (a), $D2$ (b) and $D3$ (c) when applying the normalizations proposed by George (1992) and Kolmogorov (1941)

3.5 Conclusion

Using the definition of the inertial subrange as the wavenumber range where $E_{11}(\kappa) \sim \kappa^n$, it is clear that the value of n varies with R_λ and the variation for the results obtained for the flow downstream of an active grid in the present study is described by

$$n = 1.66 - 20R_\lambda^{-0.889}. \tag{3.22}$$

These results are consistent with results obtained not only in previous studies in the region

downstream of an active grid, but also in a turbulent boundary layer as reported by SV94. The inclusion of n values obtained from the active grid study of MW96, the turbulent boundary layer studies of SV94 and the atmospheric boundary layer and mixing layer study of PO94 leads to a slight modification of the computed variation of n with R_λ as

$$n = 1.69 - 5.86 R_\lambda^{-0.645}. \tag{3.23}$$

The uncertainty of the asymptotic value of n predicted by equation 3.23 is ± 0.036. That uncertainty is too large to determine a reasonably accurate value for the intermittency factor, μ. In addition, the original estimate of 5/3 for the value of n made by Kolmogorov falls within this uncertainty range.

Based on equation 3.22, n is within 2% of the asymptotic value of $n = 1.66$ at $R_\lambda \geq 1440$ and based on equation 3.23, n is within 2% of the asymptotic value of $n = 1.69$ at $R_\lambda \geq 3000$. Thus, a conservative estimate for the minimum value of R_λ where the inertial subrange slope might be expected to remain a constant thereafter is $R_\lambda \approx 3000$.

A quantitative comparison of the effectiveness of the three normalizations suggests the normalization proposed by vonKarman & Howarth (1938) does as well as the Kolmogorov (1941) normalization in normalizing the inertial subrange where the George (1992) normalization does not work as well. The VKH normalization does not work in the dissipation range where the Kolmogorov normalization is best. The George normalization also does a better job in the dissipation range of the power spectrum than the VKH normalization, but not as good as the Kolmogorov normalization. Based on qualitative observations, the George normalization does a better job in the energy-containing portion of the spectra than Kolmogorov normalization, but not as good as the VKH normalization. Furthermore, it appears as though $R_\lambda \geq 350$ is sufficient to remove any dependence on R_λ in the effectiveness of collapse in the inertial subrange for the Kolmogorov and VKH normalizations.

Chapter 4

Modified spectrum model

4.1 Abstract

A model of the one-dimensional velocity power spectrum is presented herein that applies to power spectra in the range of Taylor Reynolds number, R_λ, from about 200 to 2000 where the slope of the inertial subrange is found to vary. The model is based on the model proposed by Pope (2000) which has been demonstrated to model power spectra at high value of R_λ where the slope of the inertial subrange is very close to $-5/3$. With one exception, the coefficients in the modified model are found to be a function of R_λ and approaching the coefficients proposed by Pope with increasing value of R_λ. That one exception is the coefficient that is most directly related to the shape of the spectrum in the dissipation range. Based on that observation, it would appear that even though the inertial subrange slope depends on R_λ, that dependence does not extend to the dissipation range. It is also suggested that the low wavenumber portion of the velocity power spectrum may not be well described by a universal model as that portion of the spectrum may well depend on initial conditions.

4.2 Background

The velocity power spectrum provides insight into how energy is distributed amongst the scales present in turbulent flows as well as the manner in which energy is transferred between those scales. The ability to accurately model the velocity power spectrum is useful for turbulence modeling, in particular Large Eddy Simulation (LES) where the spectrum of the sub-grid scale must be modeled in order to focus computational power to resolving the large scales. Heretofore, most spectrum models do not take into account the changing slope with respect to Taylor Reynolds number (cf. Pao (1965), Pope (2000)) that has been observed in several experiments (cf. Saddoughi & Veeravalli (1994), Mydlarski & Warhaft (1996)) including the results presented in Chapter 2. Instead, models have been developed for spectra with high R_λ values and where the slope of the inertial subrange is a contant. Gamard & George (2000) propose a composite model that merges a low wavenumber and high wavenumber model together and match the varying slope of the inertial subrange as a function of R_λ utilizing spectral data from Mydlarski & Warhaft (1996). Pope (2000) proposes a composite model, which he compares to several power spectra obtained from a variety of flows at various values of Taylor Reynolds number. This model, however, does not predict the varying slope of the inertial subrange with respect to R_λ. The goal of this paper is to extend the model proposed by Pope to account for the variation of the slope of the inertial subrange with respect to R_λ.

4.2.1 Spectrum model

Pope (2000) proposes a model for the three-dimensional spectrum, $E_p(\kappa)$, which is described as

$$E_p(\kappa) = C\epsilon^{2/3}\kappa^{-5/3} f_l(\kappa l) f_\eta(\kappa\eta) \tag{4.1}$$

where $C = 1.5$ is the universal Kolmogorov constant, ϵ is the dissipation rate, κ is the wavenumber, η is the Kolmogorov length scale and l is the integral length scale, which is taken to be related to the velocity scale $\mathbf{u} = \overline{u^2}^{1/2}$ and the dissipation rate as

$$l = D\overline{u^2}^{3/2}/\epsilon \tag{4.2}$$

where D is a constant of proportionality. In Pope's analysis, D is assumed to be a constant, however, for low values of R_λ, it has been found to vary with respect to R_λ. For example, for the study presented herein, it is found to only become a constant for $R_\lambda \gtrsim 450$. f_l and f_η are are non-dimensional functions that determine the shape of the energy-containing and dissipation range, respectively. f_l is described by

$$f_l(\kappa l) = \left(\frac{\kappa l}{[(\kappa l)^2 + c_l]^{1/2}} \right)^{5/3+p_o} \tag{4.3}$$

where c_l is a positive constant and $p_o = 2$ such that $f_l \to 1$ for large κl and $E(\kappa)$ varies as $\kappa^{p_o} = \kappa^2$. It is has been shown (Kang *et al.*, 2003) that the anisotropy in the flow downstream of an active grid at high R_λ is isolated to the large scales and can be dependent on the turbulence generator and initial conditions, which directly affects the value for c_l. f_η

is described by

$$f_\eta(\kappa\eta) = exp\left\{-\beta\left\{\left[(\kappa\eta)^4 + c_\eta^4\right]^{1/4} - c_\eta\right\}\right\} \tag{4.4}$$

Where β and c_η are positive constants such that $f_\eta \to 1$ for small values of $\kappa\eta$. Using the turbulent boundary layer spectra of Saddoughi & Veeravalli (1994), hereafter referred to as SV94, Pope (2000) finds that $\beta = 5.2$ and that at very high Taylor Reynolds numbers, $c_l = 6.78$ and $c_\eta = 0.4$ are determined by the requirement that $E(\kappa)$ and $2\nu\kappa^2 E(\kappa)$ integrate to κ and ϵ respectively.

Non-dimensionalizing equation 4.1 by the normalization proposed by Kolmogorov (1941), yields the expression

$$\frac{E_p(\kappa)}{(\epsilon\nu^5)^{1/4}} = C(\kappa\eta)^{-5/3} f_l(\kappa l) f_\eta(\kappa\eta) \tag{4.5}$$

In the inertial subrange, f_l and f_η are unity and, therefore, equation 4.1 suggests that the slope of the spectrum in the inertial subrange is $-5/3$ as proposed by Kolmogorov (1941). It has been shown in Chapter 3 that the slope of the inertial subrange follows

$$n = -\frac{5}{3} - \frac{\mu}{9} + C_1 R_\lambda^{C_2} \tag{4.6}$$

where $C_1 = 5.86$, $C_2 = -0.645$ and μ is the intermittency exponent. Thus, the model proposed by Pope (2000) must be modified.

4.2.2 Modified spectrum model

The following modified model equation is proposed herein for $E(\kappa)$:

$$E(\kappa) = C_\phi \epsilon^{2/3+\phi} \kappa^{-\frac{5}{3}-\frac{\mu}{9}+C_1 R_\lambda^{C_2}} f_l(\kappa l) f_\eta(\kappa\eta) \tag{4.7}$$

where C_ϕ and ϕ are dimensional parameters that are required so that the right hand side of equation 4.7 has the same unit as $E(\kappa)$, i.e., $[m^3/s^2]$, where square brackets denote units. To determine ϕ, it is useful to show equation 4.7 in the form

$$E(\kappa) = \left(C_\phi \epsilon^\phi \kappa^{-\frac{\mu}{9}+C_1 R_\lambda^{C_2}} \right) \epsilon^{2/3} \kappa^{-5/3} f_l(\kappa l) f_\eta(\kappa\eta) \tag{4.8}$$

where the product of the variables inside the parenthesis must be dimensionless in order to for the right hand side of the equation to have the same units as $E(\kappa)$. The only way to eliminate the dimensions of $\kappa^{-\frac{\mu}{9}+C_1 R_\lambda^{C_2}}$, where $\kappa = [1/m]$, is to choose ϕ such that $\epsilon^\phi \kappa^{-\frac{\mu}{9}+C_1 R_\lambda^{C_2}}$ is not a function of $[m]$, or alternatively that

$$[m^2/s^3]^\phi [1/m]^{-\frac{\mu}{9}+C_1 R_\lambda^{C_2}} = [m]^0. \tag{4.9}$$

This leads to

$$2\phi + \frac{\mu}{9} - C_1 R_\lambda^{C_2} = 0 \tag{4.10}$$

or

$$\phi = \frac{1}{2}\left(C_1 R_\lambda^{-C_2} - \frac{\mu}{9}\right). \tag{4.11}$$

This choice of ϕ leads to a second issue with respect to units, specifically,

$$\epsilon^{\frac{1}{2}\left(C_1 R_\lambda^{-C_2} - \frac{\mu}{9}\right)} \kappa^{-\frac{\mu}{9} + C_1 R_\lambda^{C_2}} = \left[\frac{1}{s^3}\right]^{\frac{1}{2}\left(C_1 R_\lambda^{-C_2} - \frac{\mu}{9}\right)}. \tag{4.12}$$

In order for the units of the right hand side of equation 4.8 to have the same units as $E(\kappa)$, C_ϕ must have units of $[s]^{\frac{3}{2}\left(C_1 R_\lambda^{-C_2} - \frac{\mu}{9}\right)}$. It will be shown later that

$$C_\phi = C\left(\frac{l}{\overline{u^2}^{1/2}}\right)^{\frac{3}{2}\left(C_1 R_\lambda^{-C_2} - \frac{\mu}{9}\right)} \tag{4.13}$$

gives the most consistent results when comparing to Pope's original model.

Equation 4.3 must also be modified to take into account the changing slope of the inertial subrange leading to

$$f_l(\kappa l) = \left(\frac{\kappa l}{[(\kappa l)^2 + c_l]^{1/2}}\right)^{n+p_o}. \tag{4.14}$$

Since f_l is dimensionless, this change does not affect the units of the right hand side of equation 4.7. Non-dimensionalizing equation 4.7 leads to

$$\frac{E(\kappa)}{(\epsilon\nu^5)^{1/4}} = 15^{-3\phi/2} C D^{3\phi} R_\lambda^{3\phi} (\kappa\eta)^{2\phi - 5/3} f_l(\kappa l) f_\eta(\kappa\eta) \tag{4.15}$$

where ϕ is defined by equation 4.11 and $D = 0.76$ for $R_{\lambda,u_q} > 365$ (cf. Chapter 2) is the normalized dissipation rate defined as

$$D = l\epsilon/\overline{u^2}^{3/2} \tag{4.16}$$

where l is the integral length scale found from the autocorrelation as described in Chapter 2. It is important to note that if $\mu = 0$, as $R_\lambda \to \infty$, equation 4.7 will approach equation 4.1.

In this study, the dissipation rate is determined using the variance of the temporal velocity derivative, Taylor's hypothesis and the assumption of local isotropy, which yields

$$\epsilon = 15\nu\overline{\left(\frac{\partial u}{\partial x}\right)^2} = \frac{15\nu}{\overline{U}^2}\overline{\left(\frac{\partial u}{\partial t}\right)^2}. \tag{4.17}$$

The Taylor Microscale is defined as

$$\lambda = \left(\frac{15\nu\overline{u^2}}{\epsilon}\right)^{1/2} \tag{4.18}$$

and the Kolmogorov scale as

$$\eta = \left(\nu^3/\epsilon\right)^{1/2}. \tag{4.19}$$

$\overline{U},\ m/s$	x/M	R_λ
4	$35 - 143.5$	$194 - 340$
8	$35 - 143.5$	$365 - 699$
12	$35 - 143.5$	$510 - 997$

Table 4.1: Experimental parameters

R_λ	x/M	$\overline{U},\ m/s$	$\overline{u^2},\ m^2/s^2$	$\epsilon,\ m^2/s^3$	$l,\ m$	$\lambda,\ mm$	$\eta,\ mm$
195	143.5	3.78	0.070	0.123	0.157	1.20	0.42
590	106	11.7	1.32	4.77	0.197	0.81	0.17
997	38	11.8	5.76	31.9	0.259	0.65	0.10

Table 4.2: Flow parameters for the cases shown in the spectrum normalization section.

4.3 Experimental parameters

The range of R_λ shown in table 4.1 is achieved by varying the test section mean speed, $\overline{U}$, and downstream location from the active grid, x/M, where M is the grid mesh length. The modified spectrum model is compared to spectra obtained in the current study with flow parameters as shown in table 4.2. In order to reduce noise, each spectrum presented herein is the average of 120 spectra computed from 1-second time records.

4.4 Analysis Procedure

The modified spectrum model shown in equation 4.7 is the three-dimensional velocity power spectrum. However, the measured power spectra, which will be used in the determination of the model coefficients are one-dimensional velocity power spectra, $E_{11}(\kappa)$. For that reason, the first step is to determine the one-dimensional power spectrum from the three-dimensional

spectrum where (cf. Pope (2000))

$$E_{11}(\kappa) = \int_{\kappa_1}^{\infty} \frac{E(\kappa)}{\kappa} \left(1 - \frac{\kappa_1^2}{\kappa^2}\right) d\kappa. \tag{4.20}$$

The next step in the analysis is to assume an initial value for C, c_l, c_η and β and use the Generalized Reduced Gradient method to determine adjusted values for those coefficients such that the square of the difference between the measured spectra and the model spectra is minimized.

4.5 Results

A comparison of the modified model and measure spectra for three values of R_λ is shown in figure 4.1. Next, the values of the model coefficients are shown as a function of R_λ and compared to the corresponding values obtained by Pope (2000), which are found to be in good general agreement. Finally, the model spectrum developed in the current study and the high R_λ model of Pope will be compared to spectra with $R_\lambda = 997$ and 590 obtained in the present study and with spectra at $R_\lambda = 600$ obtained from the turbulent boundary layer flow of SV94.

One-dimensional spectra obtained in the current experiment for values of R_λ of 997, 590 and 207 are shown in figure 4.1. Flow parameters corresponding to these spectra are shown in table 4.2. The dashed lines represent the one-dimensional modified model spectrum based on the three-dimensional modified spectrum model obtained from equations 4.15 and 4.11 and converted using equation 4.21. It should not be surprising that the modified model spectrum follows the experimentally obtained spectra closely since they are used to obtain the coefficients for the model. However, it should be noted that the coefficients directly

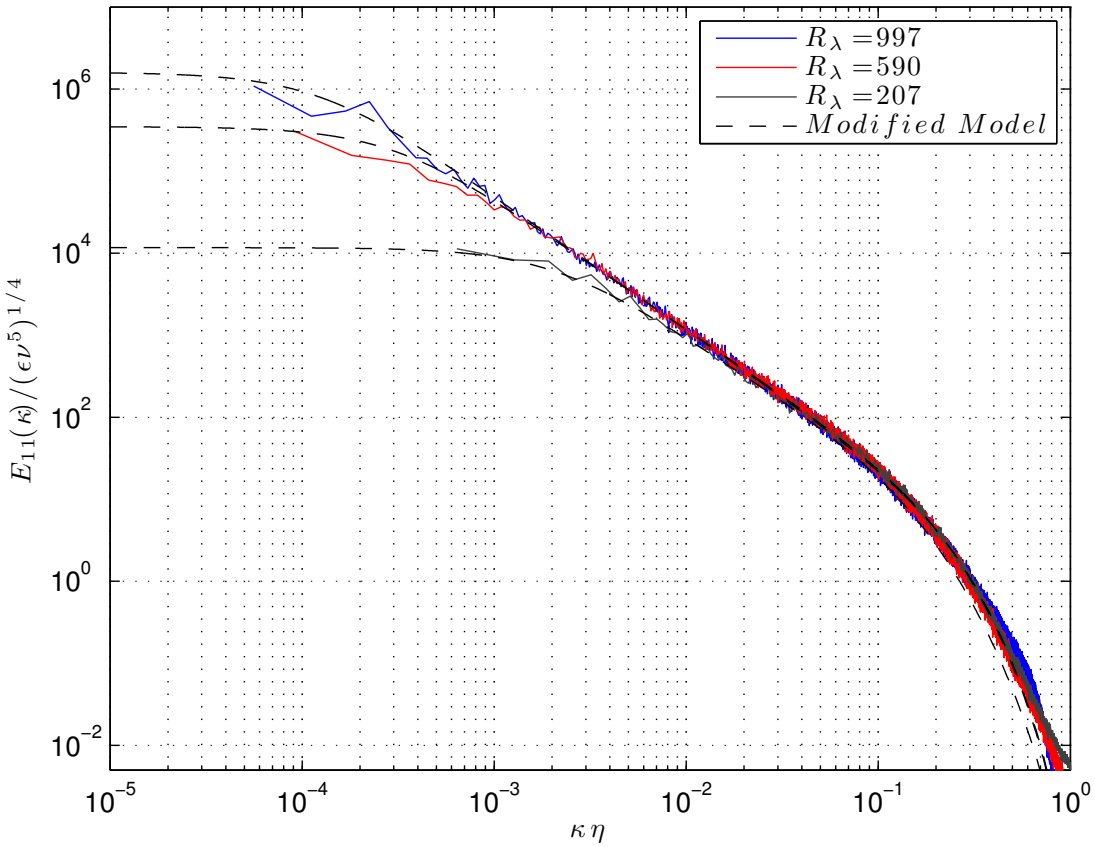

Figure 4.1: One-dimensional velocity power spectra normalized using Kolmogorov's normalization. The dashed line represents the one-dimensional modified model spectrum based on the three-dimensional modified spectrum model defined in equations 4.15 and 4.11 and converted using equation 4.21.

obtained from fitting the modified model to the experimental data are not used in generating the model spectra shown in figure 4.1 or any subsequent figure. Instead, least squares curve fits of the coefficients as a function of R_λ are used to form the modified model spectra.

The shape of the high wavenumber dissipation range of the velocity power spectrum is primarily related to f_η, which is described by equation 4.4. The coefficient that is most directly related to the curvature of the velocity power spectrum in the transitional region between the inertial subrange and the dissipation range is c_η and, to a lesser extent, β. Figure 4.2 shows c_η as a function of R_λ where the solid line represents a least squares curve

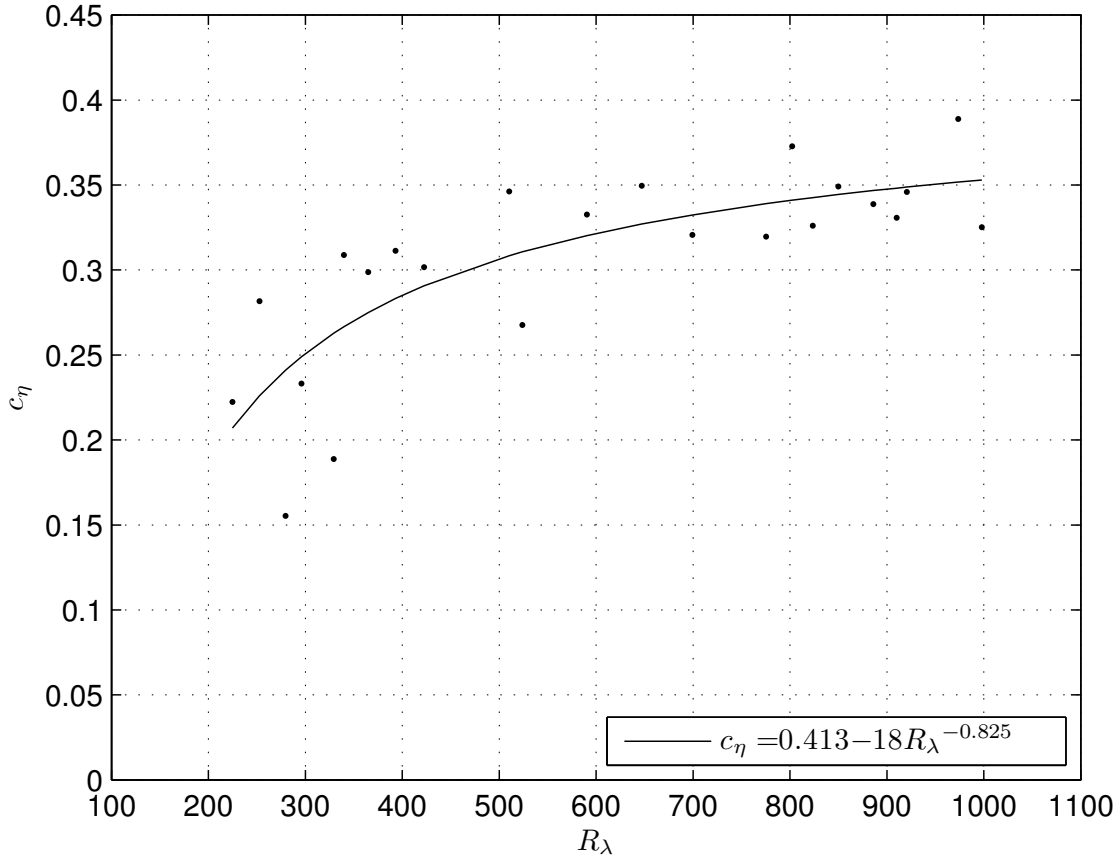

Figure 4.2: c_η as a function of R_λ. The solid line represents a least squares curve fit of the data.

fit of the data. It is clear that c_η increases with increasing R_λ and appears to be approaching a constant value. The least squares curve fit described by $c_\eta = 0.413 - 18R_\lambda^{-0.825}$ shows that c_η will asymptote to a value close to 0.4, which is in agreement with the value proposed by Pope (2000). This result should not be surprising since it is shown that in the limiting case when R_λ approaches infinity, the slope of the inertial subrange approaches a number close to $-5/3$, as is discussed in Chapter 3. Therefore, the modified model described by equation 4.15 will approach the original model proposed by Pope described by equation 4.5.

Figure 4.3 shows β as a function of R_λ. Although there is some scatter in the values of β, it appears as though β does not vary with respect to R_λ. The average value of β is 6.3 and is in

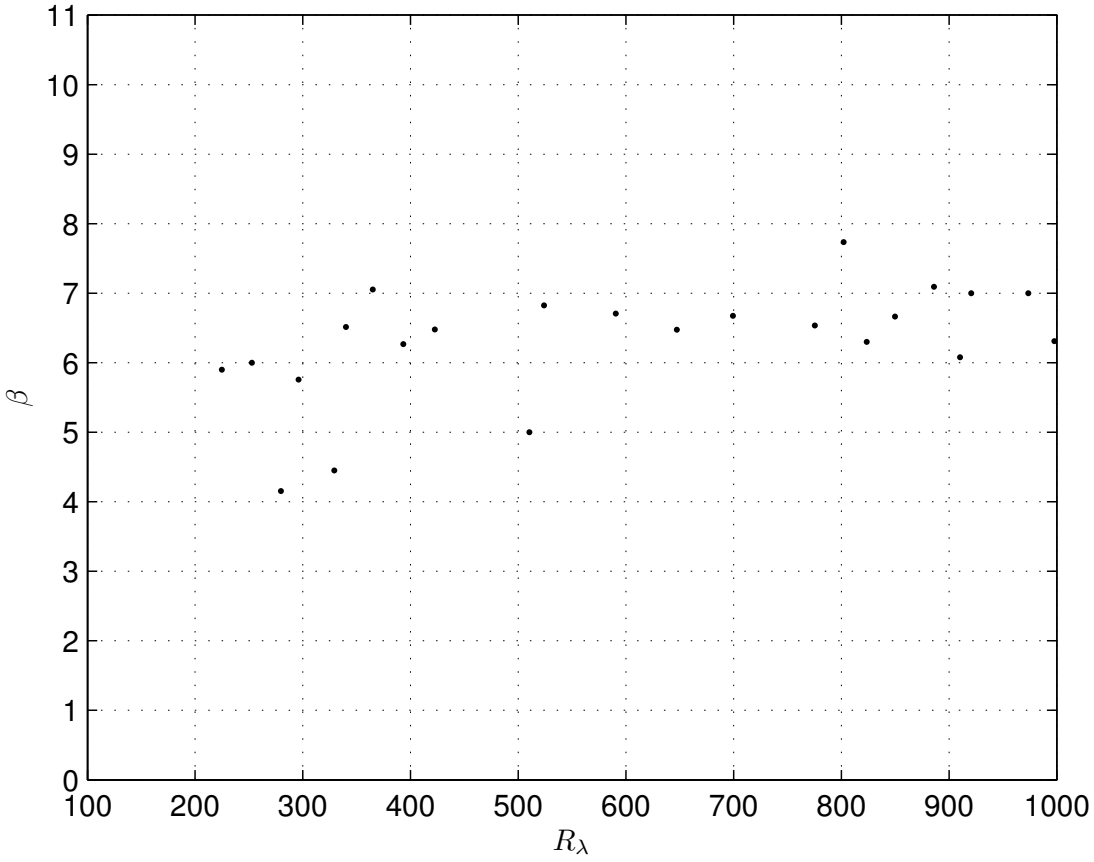

Figure 4.3: β as a function of R_λ.

reasonable agreement with the value of 5.2 proposed by Pope (2000). The lack of variation in β with respect to R_λ suggests that the high wavenumber portion of the dissipation range is independent of R_λ and, thus, independent of the variation in the slope in the inertial subrange. In contrast, c_η, is a function of R_λ. At small values of R_λ, say smaller than 400, the slope of the inertial subrange is significantly less steep than $-5/3$, which would require a value for c_η far smaller than 0.4 to properly transition the power spectrum from the R_λ dependent inertial subrange to the R_λ independent dissipation range.

The spectral values of the modified spectrum model are proportional to the constant, C, which is defined as the Kolmogorov constant, at all wavenumbers. Figure 4.4 shows the values for C as a function of R_λ where the solid line represents a least squares curve fit of the

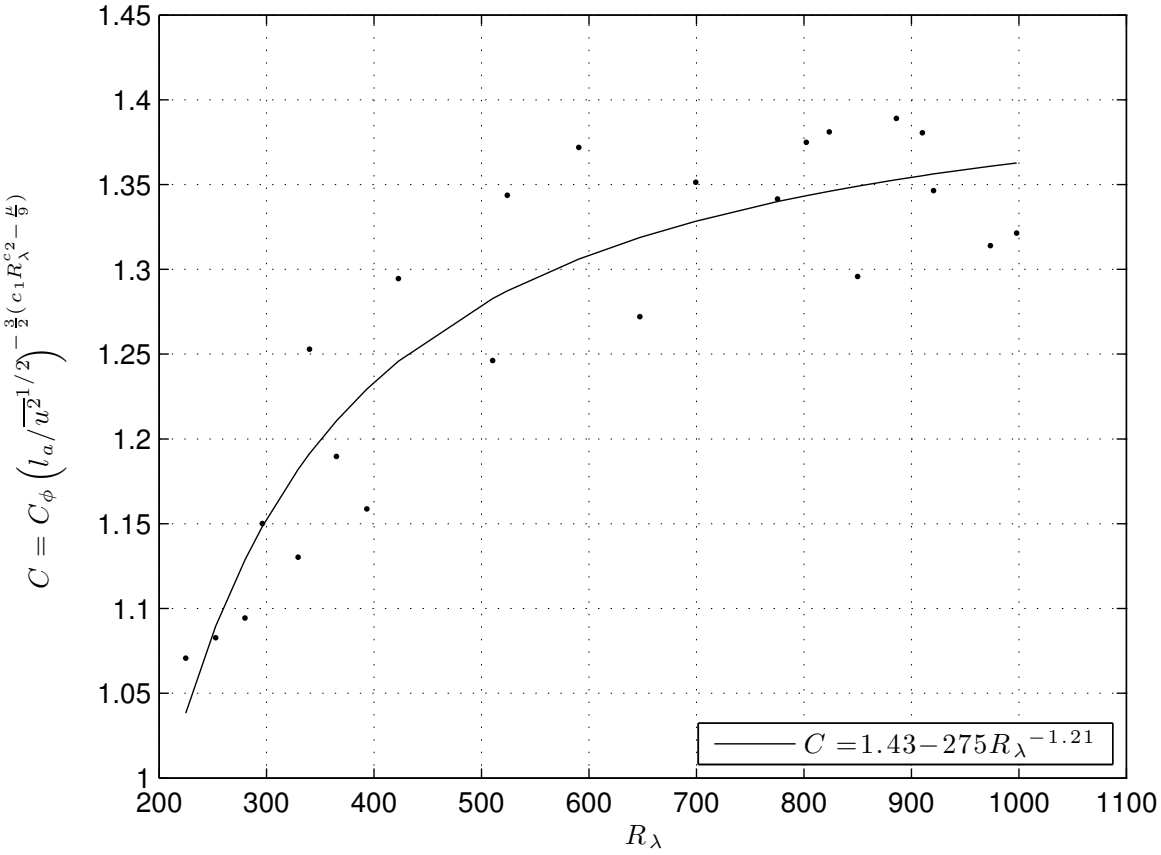

Figure 4.4: The Kolmogorov constant, C, as a function of R_λ. The solid line represents a least squares curve fit of the data.

data and is described by $C = 1.43 - 275 R_\lambda^{-1.21}$. The values for C increase with increasing R_λ and the curve fit suggests that this trend will plateau at $C \approx 1.43$. This is in close agreement with the experimentally accepted value of 1.5 found by Sreenivasan (1995) and used by Pope (2000).

The shape of the low wavenumber energy-containing portion of the velocity power spectrum is most directly related to f_l, which is presented in equation 4.3 and which is primarily dependent on the coefficient c_l. Figure 4.5 shows the values of c_l obtained in the current study as a function of R_λ where they can be seen to decrease with increasing values of R_λ for $R_\lambda < 750$. The c_l values appear to reach nearly a constant of about 0.25 for $R_\lambda > 750$.

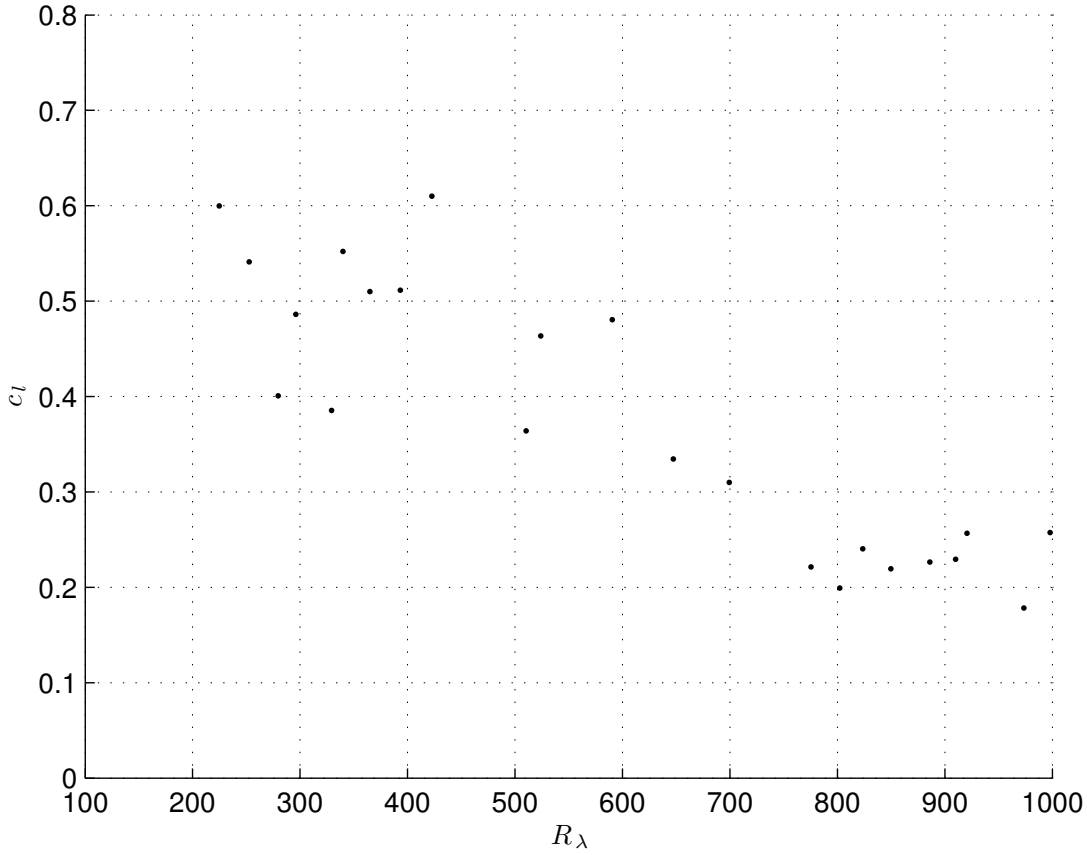

Figure 4.5: c_l as a function of R_λ.

These values for c_l are significantly less than, and are not trending towards, the value of 6.78 proposed by Pope (2000). One reason for the difference between the c_l values found in the current study and the c_l value proposed by Pope is that the shape of the low wavenumber portion of the spectra obtained in the current study is more directly related to the initial conditions, i.e., to the large scale structures produced by the turbulence generators. This is consistent with the findings of Kang *et al.* (2003) that the large scales can depend on the characteristics of the turbulence generator.

Figure 4.6 shows normalized velocity power spectra for $R_\lambda = 590$ and 997 obtained in the present study as well as normalized velocity power spectra for $R_\lambda = 600$ and 1450 obtained by SV94 in a turbulent boundary layer flow. The spectra for R_λ values of 600 and 590 obtained

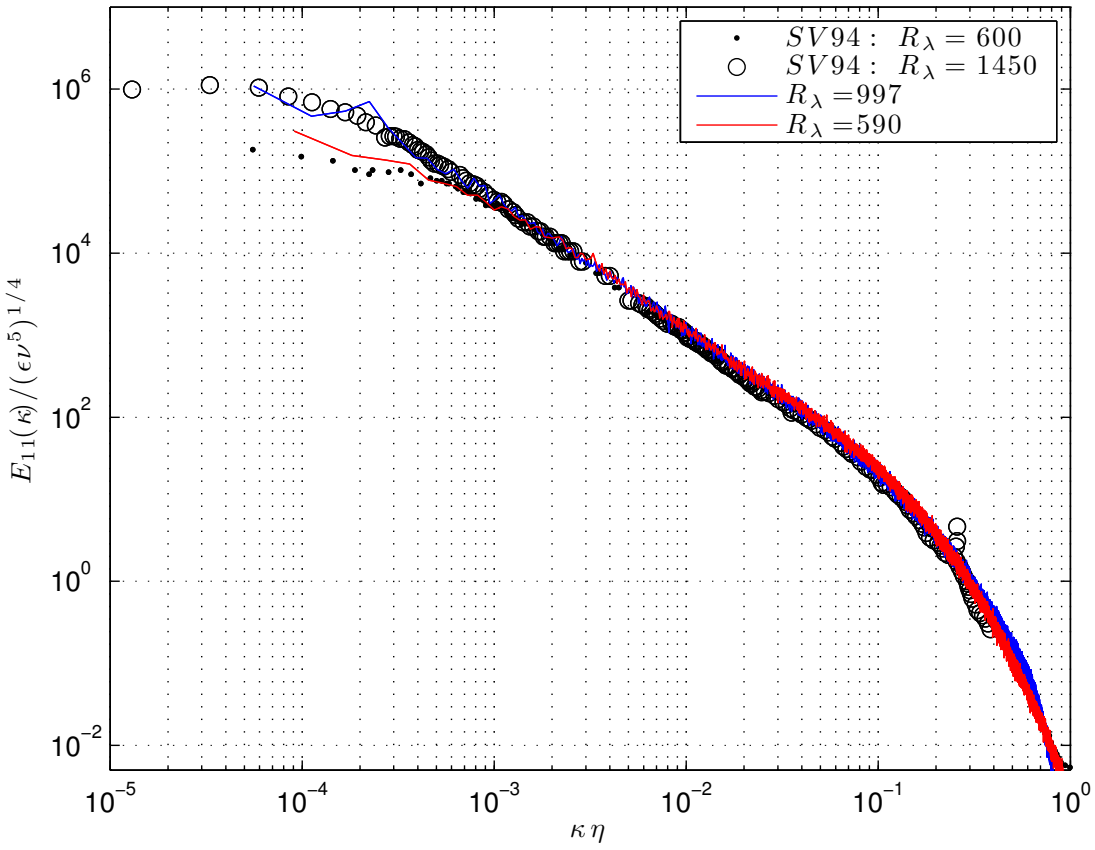

Figure 4.6: Normalized velocity power spectra for $R_\lambda = 997$ and 590 obtained in the current study. The dots and circles represent normalized velocity power spectra for $R_\lambda = 600$ and 1450 obtained in SV94, respectively.

from SV94 and the present study, respectively, show large differences in the value of the normalized power spectra for corresponding wavenumbers in the low wavenumber energy containing range even though their R_λ values nearly match. This observation is consistent with the suggestion that the low wavenumber portion of the power spectrum depends on the initial conditions. Those differences are significantly smaller in the inertial subrange and the dissipation range. Similarly, the spectra for R_λ values of 1400 and 997 obtained from SV94 and the present study, respectively, show small differences in the value of the normalized power spectra for corresponding wavenumbers in the low wavenumber energy containing range even though their R_λ values are significantly different. The model spectrum proposed

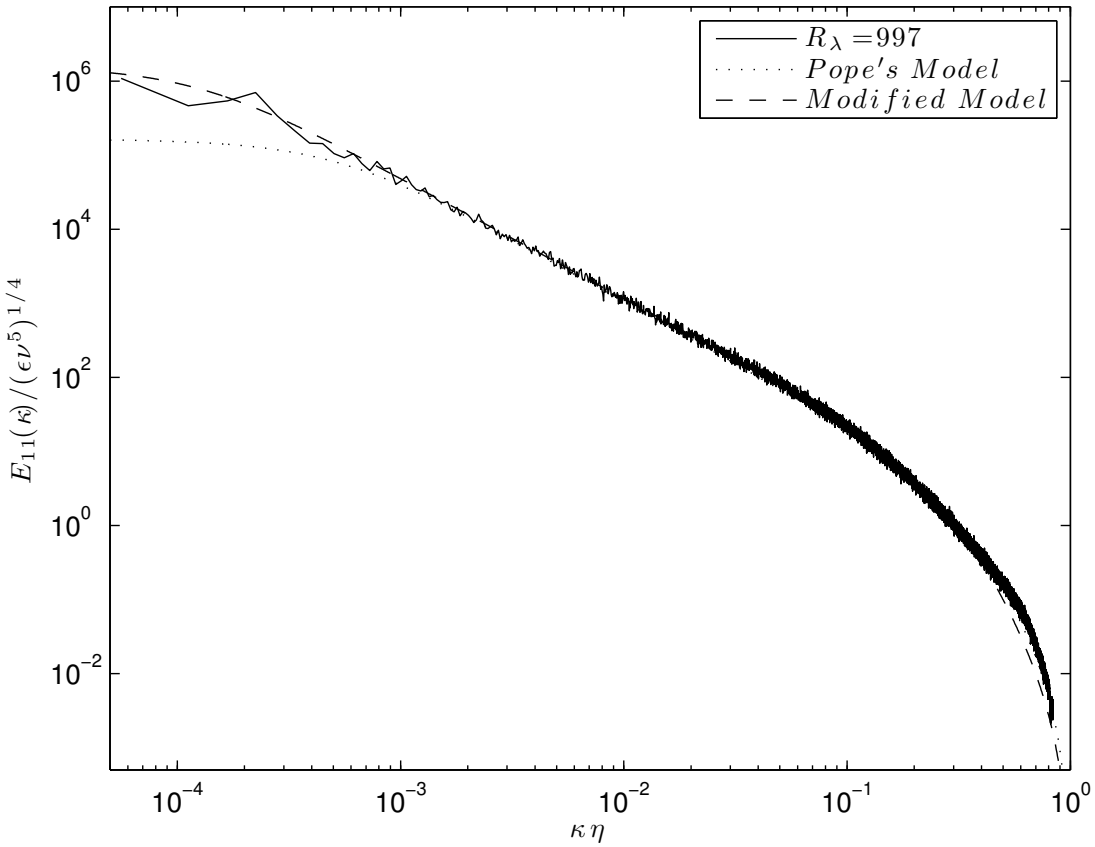

Figure 4.7: Normalized velocity power spectrum for $R_\lambda = 590$. The dotted line represents the model proposed by Pope (2000) and outlined by equation 4.5 and the dashed line represents the modified model that is outlined by equation 4.15.

by Pope (2000) and the modified model spectrum proposed in the current study is uniquely determined by the shape of the low wavenumber portion of the spectrum. This means that since the low wavenumber portion of the spectrum is dependent on the manner in which the turbulence is being generated, this model or any model that is based on experimentally determined values of the low wavenumber portion of different types of flow should not be expected to match. Since the anisotropy of high R_λ flows is isolated to the large scales, the modified model presented herein is expected to model the velocity power spectrum in the inertial subrange and the dissipation range.

Figure 4.7 show the normalized velocity power spectrum for $R_\lambda = 997$ for the present study.

The dotted line represents the model proposed by Pope (2000) and expressed by equation 4.5 and the dashed line represents the modified model that corresponds to equation 4.15. As is expected due to the large difference between the c_l values obtained for the present study and the c_l value proposed by Pope, the low wavenumber energy-containing region of the velocity power spectrum does not match the Pope model. Since this portion of the power spectrum is dependent on initial conditions, the accuracy of the model proposed herein is best assessed by comparison of the spectrum predicted by the model to the measured spectrum in the inertial subrange and dissipation range.

Although it appears that the differences between the original spectrum model and the modified one in the inertial subrange is small, it is important to point out that the modified model spectrum is consistent with the changing slope with respect to R_λ of inertial subrange while the Pope model is not. Plotting the spectra using a logarithmic scale presents more explicitly the relative high energy associated with the large scales. However, the changing slope of the inertial subrange with respect to R_λ is not obvious. Figure 4.8 shows the compensated normalized velocity power spectrum, $E_{11}(\kappa)/(\epsilon\nu^5)^{1/4} \times (\kappa\eta)^n$, where $n = 1.62$ is the measured slope of the inertial subrange for $R_\lambda = 997$. The dashed line represents the original spectrum model and the solid line represents the modified spectrum model. As expected, the inertial subrange is flat when the velocity power spectrum is compensated by $(\kappa\eta)^n$ if n is chosen to be the slope of the inertial subrange. The slope of the inertial subrange for Pope's model is $-5/3$ and does not match the measured slope of the power spectrum. At large wavenumbers both models agree with the measured spectra. The small differences correspond to the difference in the value of β found in the current study as compared to the β value proposed by Pope (2000). Since the slope of the inertial subrange decreases with decreasing R_λ, the differences between the original model and the modified model would increase with decreasing values of R_λ.

Figure 4.9 shows the compensated normalized velocity power spectrum, $E_{11}(\kappa)/(\epsilon\nu^5)^{1/4} \times$

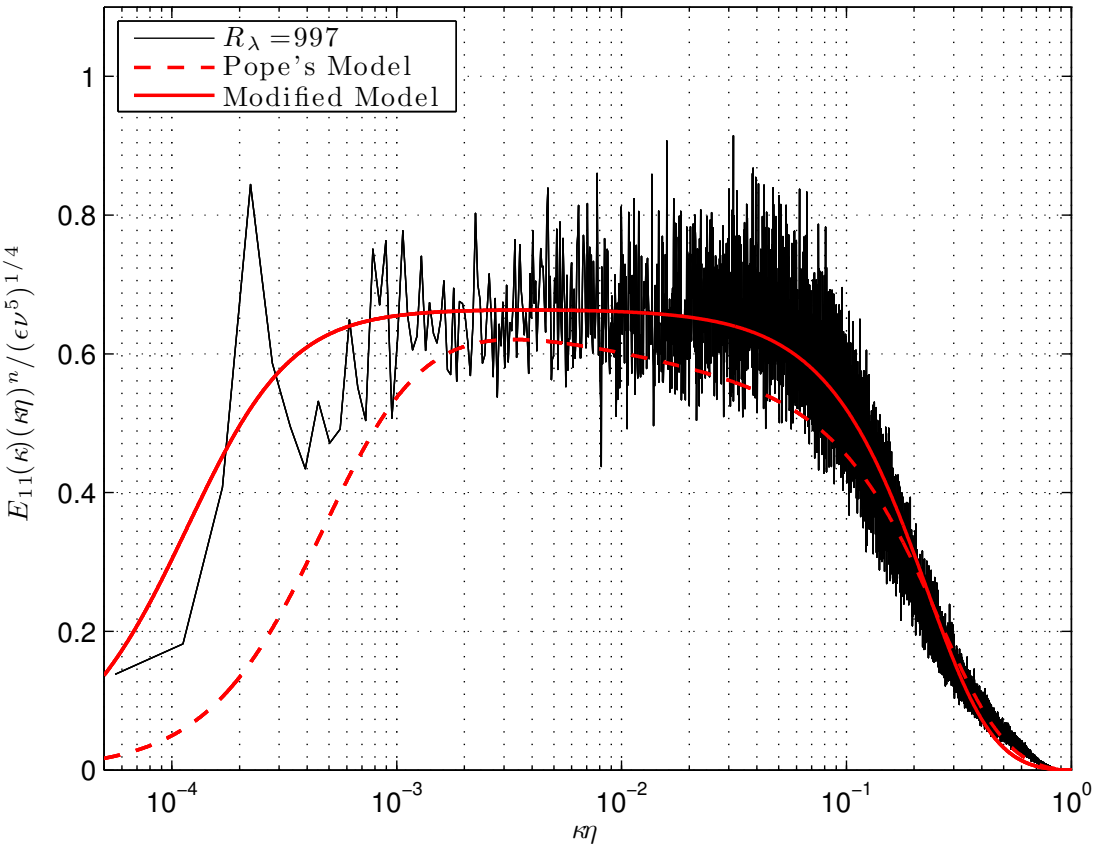

Figure 4.8: Compensated normalized velocity power spectrum, $E_{11}(\kappa)/(\epsilon\nu^5)^{1/4}\times(\kappa\eta)^n$, where n is the measured slope of the inertial subrange for $R_\lambda = 997$. The dotted line represents the model proposed by Pope (2000) and the dashed line represents the modified model proposed herein.

$(\kappa\eta)^n$, where $n = 1.59$ is the measured slope of the inertial subrange for $R_\lambda = 590$. The dashed line represents Pope's model and the solid line represents the modified spectrum model presented herein. It is clear that the two models differ in the inertial subrange and the wavenumber range separating the inertial subrange and the dissipation range, however, as is seen in figure 4.8, there is marginal difference in the high wavenumber dissipation range.

SV94 obtain velocity power spectra in a turbulent boundary layer that show a varying inertial subrange slope with respect to R_λ and which Pope (2000) uses to determine β for the Pope model. Figure 4.10 shows the compensated normalized velocity power spectrum,

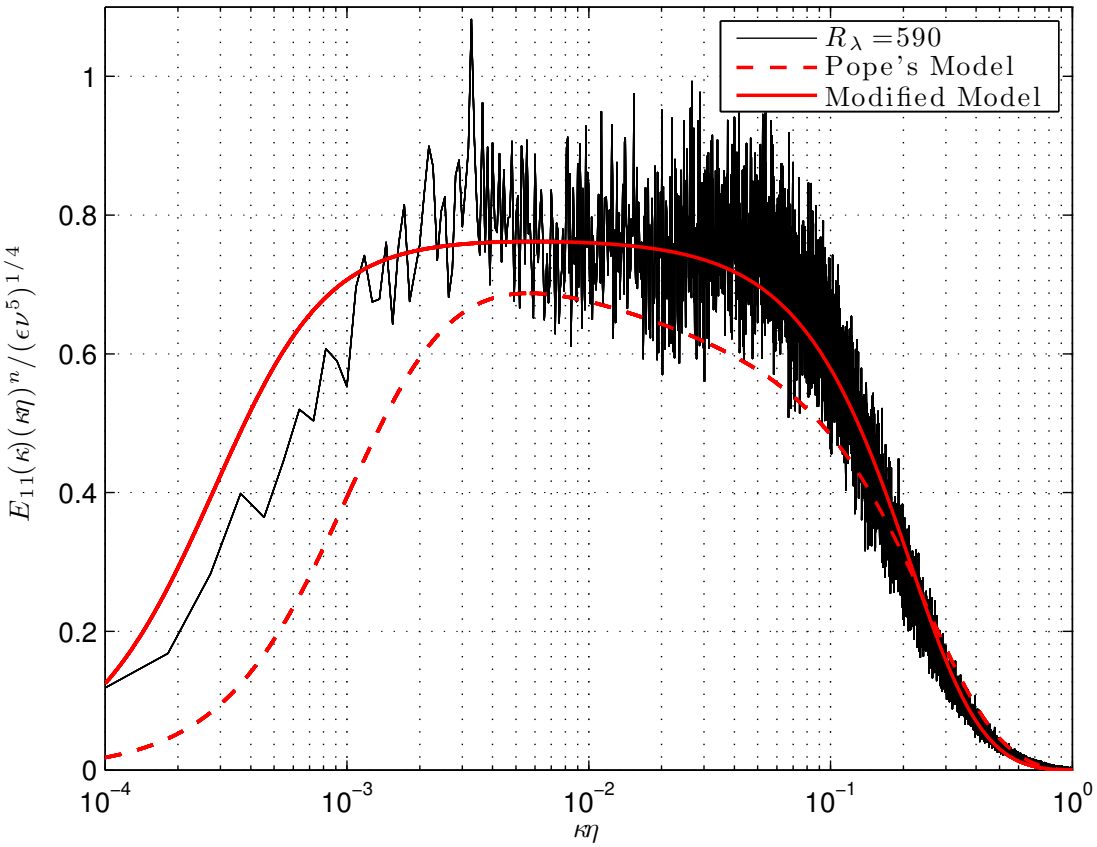

Figure 4.9: Compensated normalized velocity power spectrum, $E_{11}(\kappa)/(\epsilon\nu^5)^{1/4}\times(\kappa\eta)^n$, where n is the measured slope of the inertial subrange for $R_\lambda = 590$. The dotted line represents the model proposed by Pope (2000) and the dashed line represents the modified model proposed herein.

$E_{11}(\kappa)/(\epsilon\nu^5)^{1/4} \times (\kappa\eta)^n$, where $n = 1.59$ is the measured slope of the inertial subrange for the SV94 spectrum obtained at $R_\lambda = 600$. The dashed line corresponds to Pope's model and the solid line corresponds to the modified model presented herein. In the inertial subrange, $2 \times 10^{-3} \leq \kappa\eta \leq 5 \times 10^{-2}$, the extent and slope of the inertial subrange of the modified model are in better agreement with the measured spectrum, but in the central region of the inertial subrange, the spectral values predicted by Pope's model are closer to the values of the measured spectrum.

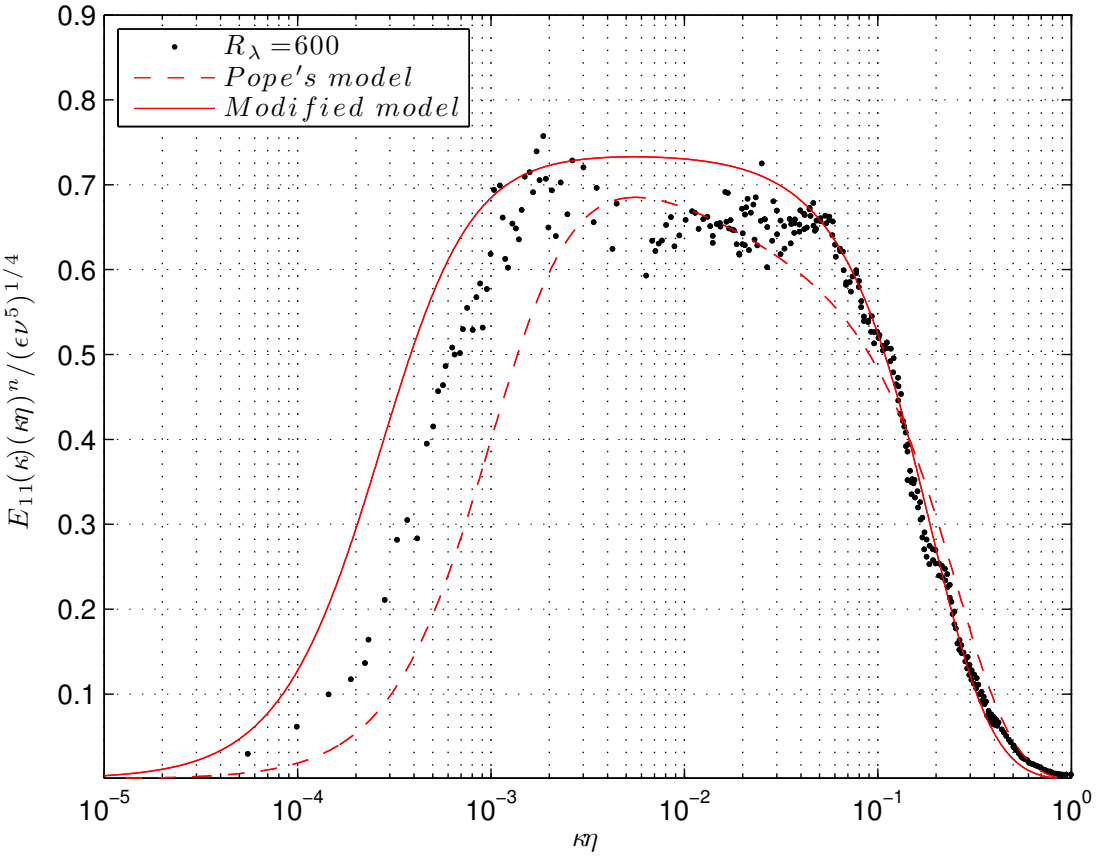

Figure 4.10: Compensated normalized velocity power spectrum, $E_{11}(\kappa)/(\epsilon\nu^5)^{1/4} \times (\kappa\eta)^n$, where n is the measured slope of the inertial subrange for $R_\lambda = 600$ for data obtained in a turbulent boundary layer (SV94). The dotted line represents the model proposed by Pope (2000) and the dashed line represents the modified model proposed herein.

The difference between the measured and modified spectral values can be estimated by

$$\sigma = \left(\frac{1}{N} \sum_{i=1}^{N} \left(F_{11,m,i} - F_{11,exp,i} \right)^2 \right)^{1/2} \Bigg/ \overline{F}_{11,exp,i} \tag{4.21}$$

where the summation takes place over the range of wavenumbers $2 \times 10^{-3} \leq \kappa\eta \leq 5 \times 10^{-2}$, $\overline{F}_{11,exp,i}$ is the average measured spectral values in that range, the subscript "m" means that spectral values correspond to the values predicted by the model and the subscript "exp" means that the spectral values correspond to the values obtained from the experimental

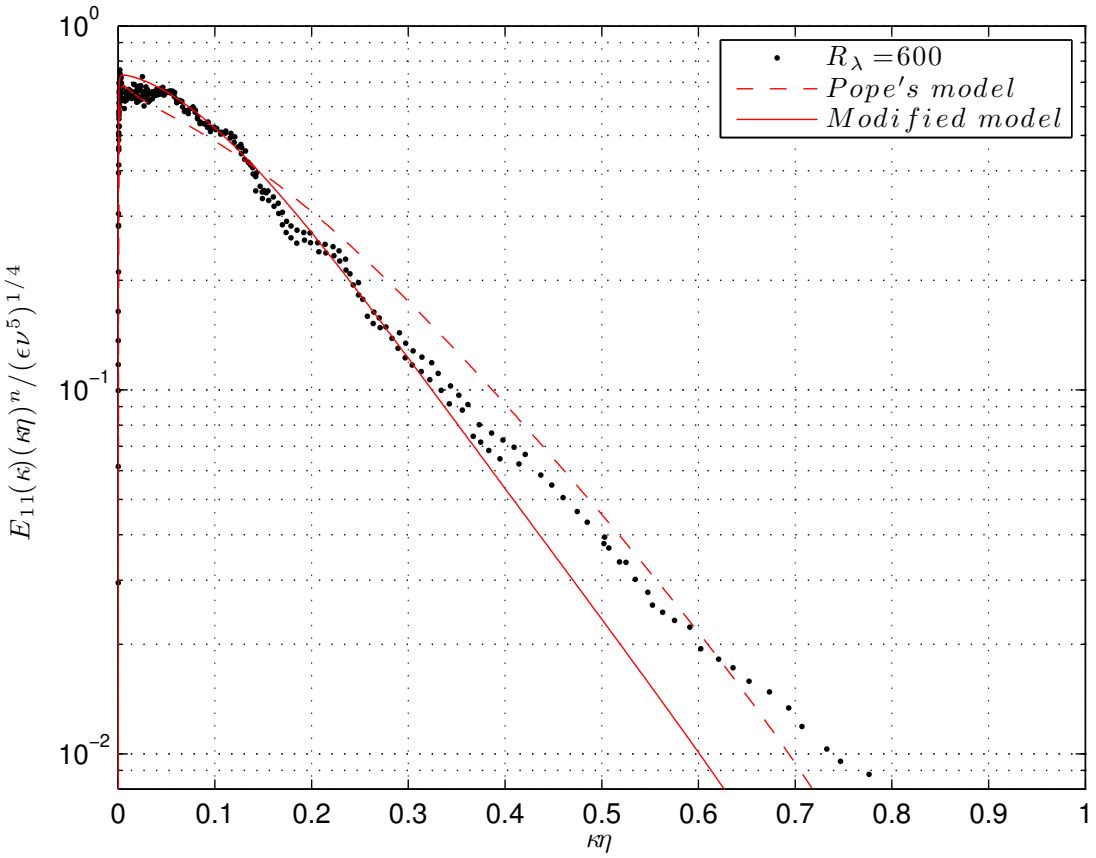

Figure 4.11: Compensated normalized velocity power spectrum, $E_{11}(\kappa)/(\epsilon\nu^5)^{1/4} \times (\kappa\eta)^n$, where n is the measured slope of the inertial subrange for $R_\lambda = 600$ for data obtained in a turbulent boundary layer (SV94). The dotted line represents the model proposed by Pope (2000) and the dashed line represents the modified model proposed herein.

spectrum. The values of σ corresponding to Pope's and the modified model are 9% and 7%, respectively, that is they are the same. For wavenumbers higher than those of the inertial subrange and extending into the dissipation range, the spectral values from Pope's model and the modified model are in closer agreement.

Figure 4.11 shows the same data as figure 4.10 except with a logarithmic scale on the y-axis and a linear scale on the x-axis. In this figure, the differences in the two models for $\kappa\eta > 0.1$ is accentuated. As expected due to the general agreement in the values of β proposed using the two models, there is less difference in this portion of the spectrum between the two

models. There appears to be a marginal improvement in the spectral values predicted by the modified model in the range $0.15 < \kappa\eta < 0.4$. However, the original model proposed by Pope shows improved spectral values for the range $\kappa\eta > 0.4$.

4.6 Conclusion

The ability to model the evolution of the velocity power spectrum as a function of R_λ could be useful for LES where the large scales are resolved and the sub-grid scales are modeled. A modification is proposed for the spectrum model proposed by Pope (2000) to take into account the variation in the slope of the inertial subrange with respect to R_λ. The modified model is shown to approach the original model proposed by Pope with increasing R_λ and is described by

$$\frac{E(\kappa)}{(\epsilon\nu^5)^{1/4}} = 15^{-3\phi/2} C D^{3\phi} R_\lambda^{3\phi} (\kappa\eta)^{2\phi-5/3} f_l(\kappa l) f_\eta(\kappa\eta) \tag{4.22}$$

where D is the normalized dissipation rate, $\phi = \frac{1}{2}\left(C_1 R_\lambda^{-C_2} - \frac{\mu}{9}\right)$ is related to the varying slope of the inertial subrange with respect to R_λ, $f_l(\kappa l) = \left(\frac{\kappa l}{[(\kappa l)^2 + c_l]^{1/2}}\right)^{n+p_o}$ is directly related to the shape of the power spectrum in the low wavenumber range and $f_\eta(\kappa\eta) = exp\left\{-\beta\left\{\left[(\kappa\eta)^4 + c_\eta^4\right]^{1/4} - c_\eta\right\}\right\}$ is more directly related to the shape of the power spectrum in the high wavenumber range. While Pope (2000) proposes that the coefficients C, c_l, c_η and β are constants with respect to R_λ, the modified model shows, with the exception of β, that they are functions of R_λ. The constants C, c_l, c_η and β are found by fitting the modified model spectrum to velocity power spectra obtained in the flow downstream of an active grid. C is the universal Kolmogorov constant, which is found to approach the experimentally accepted value of 1.5 (Sreenivasan, 1995) with increasing values of R_λ. The constant c_η is found to approach 0.413 with increasing values of R_λ, which is in close agreement with the

value of 0.4 proposed by Pope (2000). The constant β found from the modified model is in general agreement with the value proposed by Pope and is not a function of R_λ suggesting that the R_λ dependence seen in the inertial subrange does not affect the high wavenumber dissipation range of the power spectrum. The constant that is directly related to the shape of the small wavenumber energy containing range, c_l, is also found to vary with respect to R_λ, however it approaches 0.2 rather than 6.78 as proposed by Pope. The comparison of the velocity power spectra obtained by SV94 in a turbulent boundary layer to the velocity power spectra obtained in the current experiment reveals that the shape of the energy containing range may be dependent on the mechanism producing the turbulence or the initial conditions as suggested by Kang *et al.* (2003).

Bibliography

Alkudsi, A. 2012 Calibration of an x-wire with assessment of a moderately high reynolds number flow. PhD thesis, University of California, Irvine, Irvine, CA.

Azad, R. S. 1993 Effects of hot-wire length and length-diameter ratio on spectral energy of turbulence. *Meas. Sci. Technol.* **4**, 405.

Boffetta, G. & Romano, G. P. 2002 Structure functions and energy dissipation dependence on reynolds number. *Phys. Fluids* **14**.

Bradbury, L. J. S. 1976 Measurements with a pulsed-wire and a hot-wire anemometer in the highly turbulent wake of a normal flat plate. *J. Fluid Mech.* **77**, 473–497.

Bruun, H. H. 1995 *Hot-Wire Anemometry*. New York: Oxford Science.

Cao, N., Chen, S. & Doolen, G. D. 1999 Statistics and structures of pressure in isotropic turbulence. *Phys. Fluids* **11**, 2235–2250.

Champagne, F. H. 1978 The fine-scale structure of the turbulent velocity field. *J. Fluid Mech.* **86**, 67–108.

Gamard, S. & George, W. K. 2000 Reynolds number dependence of energy spectra in the overlap region of isotropic turbulence. *Flow Turbul. Combust.* **63**, 443–477.

George, W. K. 1992 The decay of homogeneous isotropic turbulence. *Phys. Fluids* **4**, 1492–1509.

Heskestad, G. 1965 A generalized taylor hypothesis with application for high reynolds number turbulent shear flows. *J. Appl. Mech.* **32**, 735–739.

Jiménez, J., Saffman, A. A. & Rogallo, R. S. 1993 The structure of intense vorticity in isotropic turbulence. *J. Fluid Mech.* **255**, 69–90.

Kaneda, Y., Ishihara, T., Yokokawa, M., Itakura, K. I. & Uno, A. 2003 Energy dissipation rate and energy spectrum in high resolution direct numerical simulations of turbulence in a periodic box. *Phys. Fluids* **15**, L21.

Kang, H. S., Chester, S. & Meneveau, C. 2003 Decaying turbulence in an active-grid-generated flow and comparisons with large-eddy simulation. *J. Fluid Mech.* **480**, 129–160.

Kolmogorov, A. N. 1941 The local structure of turbulence in incompressible viscous fluid for very large reynolds numbers. *Dokl. Akad. Nauk SSSR* **30**, 301–305.

Kolmogorov, A. N. 1962 A refinement of previous hypotheses concerning the local structure of turbulence in a viscous incompressible fluid at high reynolds number. *J. Fluid Mech.* **13**, 82–85.

Makita, H. & Sassa, K. 1991 Active turbulence generation in a laboratory wind tunnel. In *Advances in Turbulence 3*, pp. 497–505. Springer Berlin Heidelberg.

Mydlarski, L. & Warhaft, Z. 1996 On the onset of high-reynolds-number grid-generated wind tunnel turbulence. *J. Fluid Mech.* **320**, 331–368.

Nguyen, B. 2015 Effect of length scales on the mixing of passive scalars in grid turbulence. Master's thesis, University of California, Irvine, Irvine, CA.

Nobach, H. & Tropea, C. 2012 A statistical method for transforming temporal correlation functions from one-point measurements into longitudinal spatial and spatio-temporal correlation functions. *Exp. Fluids* **53**, 1815–1821.

Pao, Y.-H. 1965 Structure of turbulent velocity and scalar fields at large wavenumbers. *Phys. Fluids* **8**, 1063–1075.

Pope, S. B. 2000 *Turbulent flows*. Cambridge, UK: Cambridge Univ. Press.

Praskovsky, A. & Oncley, S. 1994 Measurements of the kolmogorov constant and intermittency exponent at very high reynolds numbers. *Phys. Fluids* **6**, 2886–2888.

Saddoughi, S. G. & Veeravalli, S. V. 1994 Local isotropy in turbulent boundary layers at high reynolds number. *J. Fluid Mech.* **268**, 333–372.

Sreenivasan, K. R. 1965 Interpretation of time spectra measured in high intensity shear flows. *Phys. Fluids* **8**, 1056–1062.

Sreenivasan, K. R. 1984 On the scaling of the turbulence energy dissipation rate. *Phys. Fluids* **27**, 1048–1051.

Sreenivasan, K. R. 1995 On the universality of the kolmogorov constant. *Phys. Fluids* **7**, 2778–2784.

Sreenivasan, K. R. 1998 An update on the energy dissipation rate in isotropic turbulence. *Phys. Fluids* **10**, 528–529.

Tennekes, H. & Lumley, J. L. 1972 *A first course in turbulence*. MIT press.

vonKarman, T. & Howarth, L. 1938 On the statistical theory of isotropic turbulence. *P. Roy. Soc. A-Math Phy.* **164**, 192–215.

Wang, L. P., Chen, S., Brasseur, J. G. & Wyngaard, J. C. 1996 Examination of hypotheses in the kolmogorov refined turbulence theory through high-resolution simulations. part 1. velocity field. *J. Fluid Mech.* **309**, 113–156.

Webb, E. K. 1955 Autocorrelations and energy spectra of atmospheric turbulencel. In *Div. of Meteorological Physics Technical Paper*. Australia: Commonwealth Scientific and Industrial Research Organization.

Wyngaard, J. C. 1968 Measurement of small-scale turbulence structure with hot wires. *J. Phys. E: Sci. Inst.* **1**, 1105.

Wyngaard, J. C. & Clifford, S. F. 1977 Taylor's hypothesis and high-frequency turbulence spectra. *J. Atmos. Sci.* **34**, 922–929.

Yeung, P. K. & Zhou, Y. 1997 Universality of the kolmogorov constant in numerical simulations of turbulence. *Phys. Rev. E: Stat.* **56**, 1746.

Appendices

A MATLAB code to find slope of inertial subrange

```
%7-10-2015

%This program will find the range of the scaling region in a
    compensated
%power spectrum (the scaling region must be as flat as possible).

clear all
close all
format shortG
s=dlmread('vel spectra 4ms-2.txt','\t',1,0);

nn=17;

[row,col]=size(s);

alimits=[1 10000 0.1 10];

```

```
17 slopeguess = 1.66;
18
19 specx    = s(:,nn);
20 specxog  = s(:,nn);
21 f        = s(:,1);
22 fog      = s(:,1);
23
24 %taking running average of specx0
25
26 avgw=1; %number of points for running average
27 avgspec=zeros(length(specx),1);
28 for i=1:(length(specx)-avgw)
29     avgspec(i)=mean(specx(i:i+avgw));
30 end
31 specx=avgspec;
32
33 %flattening plateau
34 tempspec=zeros(length(f),1);
35 for i = 1:length(f);
36     tempspec(i)=specx(i)*f(i)^(slopeguess);
37 end
38
39 tempspec2=zeros(length(f),1);
40 for i = 1:length(f);
41     tempspec2(i)=specx(i)*f(i)^(1);
42 end
43
```

```
%user input of plateau region

figure(1)
loglog(f,tempspec)
%axis([1 2000 0.2 0.8])
grid on

[fguess,y] = ginput(2);

close all

fstart = round(fguess(1));
fend   = round(fguess(2));

close all

j=1;
for i=fstart:fend;
    plat(j)=tempspec(i);
    fplat(j)=f(i);
    j=j+1;
end

%initializing plateau

F=@(z,zdata)(z(1).*zdata+z(2));
z0=[0,0.5];
```

```
71 z = lsqcurvefit(F,z0,fplat,plat); %z=[slope,y-int]
72
73 deltaslope=z(1);
74
75 while deltaslope>0.00005
76
77     for i=1:length(f);
78         tempspec(i)=specx(i)*f(i)^(slopeguess-deltaslope);
79     end
80
81     slopeguess=slopeguess-deltaslope;
82
83     j=1;
84     for i=fstart:fend;
85         plat(j)=tempspec(i);
86         fplat(j)=f(i);
87         j=j+1;
88     end
89
90     F=@(z,zdata)(z(1).*zdata+z(2));
91     z0=[0,0.5];
92     z = lsqcurvefit(F,z0,fplat,plat); %z=[slope,y-int]
93
94     deltaslope=z(1);
95 end
96
97 j=1;
```

```
98  for i = 17:980;
99      sr(j)=specxog(i);
100     fsr(j)=fog(i);
101     j=j+1;
102 end
103
104 F1=@(x,xdata)(x(1).*xdata.^(-x(2)));
105 x0=[5,slopeguess];
106 x = lsqcurvefit(F1,x0,fsr,sr); %z=[slope,y-int]
107
108 % for i=1:length(f);
109 %     platfit(i)=z(1)*f(i)^-z(2);
110 % end
111
112 for i = 1:length(f);
113     tempspec(i)=specxog(i)*f(i)^(slopeguess);
114 end
115
116 figure(1)
117 loglog(f(1:3000),tempspec(1:3000))
118 %axis([1 2000 0.2 0.8])
119 grid on
120
121 % Program below takes the compesated output from above
122
123 specx0=tempspec;
124 specx0og=specxog;
```

```
125
126 alimits=[1 10000 0.1 10];
127
128 %taking running average of specx0
129
130 avgw=5; %number of points for running average
131 avgspec=zeros(length(specx0),1);
132
133 for i=1:(length(specx0)-avgw)
134     avgspec(i)=mean(specx0(i:i+avgw));
135 end
136
137 specx0=avgspec;
138
139 %user input of plateau region
140
141 j=1;
142 for i=fstart:fend;
143     plat(j)=specx0(i);
144     fplat(j)=f(i);
145     j=j+1;
146 end
147
148 %initializing plateau
149
150 F=@(z,zdata)(z(1).*zdata + z(2));
151 z0=[0,0.5];
```

```
z = lsqcurvefit(F,z0,fplat,plat); %z=[slope,y-int]


midplat=round((fend+fstart)/2);

for i=1:length(f);
    platfit(i)=f(midplat)*z(1)+z(2);
end

figure(2)
loglog(f,specx0)
axis(alimits)
grid on
hold on
loglog(f,platfit,'r')

j=1;
k=1;
for i=1:length(specx0og);

    if ( (specx0(i)-platfit(j))>0 );
        tempplat(j)=specx0og(i);
        tempf(j)=fog(i);
        j=j+1;

    end
end
```

```
179
180 fstart=round(tempf(1));
181 if fstart==0;
182     fstart=1;
183 end
184 fend=round(tempf(length(tempf)));
185
186 figure(3)
187 loglog(f(1:3000),tempspec(1:3000))
188 hold on
189 loglog(f(fstart:fend),tempspec(fstart:fend),'r')
190 loglog(f,platfit,'k')
191 %axis([1 2000 0.2 0.8])
192 grid on
193
194 clear plat fplat
195
196 plat=tempplat;
197 fplat=tempf;
198
199 figure(4)
200 loglog(fog,specx0og)
201 hold on
202 grid on
203 loglog(fog(fstart:fend),specx0og(fstart:fend),'r')
204 loglog(f,platfit,'k','LineWidth',1)
205 %axis(alimits)
```